Quad module prototypes and design improvement studies of planar n^+-in-n silicon pixel sensors for the ATLAS Inner Tracker upgrade

Dissertation
zur Erlangung des akademischen Grades
Doktor der Naturwissenschaften

vorgelegt von

Andreas Gisen

Lehrstuhl für Experimentelle Physik IV
Fakultät Physik
Technische Universität Dortmund
Juni 2018

Erstgutachter:	Prof. Dr. K. Kröninger
Zweitgutachter:	Prof. Dr. T. Weis / Prof. Dr. Dr. W. Rhode
Prüfungsvorsitz:	Prof. Dr. M. Betz
Prüfungsbeisitz:	Dr. B. Siegmann

Datum des Einreichens der Arbeit:	28. Juni 2018
Datum der Promotionsprüfung:	2. Oktober 2018

Fassung vom 22. Oktober 2018.

Abstract

In order to meet the requirements of the High Luminosity-LHC (HL-LHC), it will be necessary to replace the current tracker of the ATLAS experiment. Therefore, a new all-silicon tracking detector is being developed, the so-called Inner Tracker (ITk). The use of quad chip modules is intended in its pixel region. These quad modules consist of four read-out chips, bump-bonded to one large silicon pixel sensor.

In this thesis, first prototypes of quad modules are investigated, which were assembled using a planar n^+-in-n silicon pixel sensor and four FE-I4 read-out chips. The focus of the investigations is the measurement of charge collected in the laboratory and the tracking efficiency for particle passages at testbeams.

In addition, the development of new pixel designs is presented.

Zusammenfassung

Um die Anforderungen des High Luminosity-LHC (HL-LHC) zu erfüllen, wird es notwendig sein, den aktuellen Tracking-Detektor des ATLAS-Experiments zu ersetzen. Deshalb wird ein neuer Silizium-Tracking-Detektor entwickelt, der sogenannte Inner Tracker (ITk). In dessen Pixelbereich ist der Einsatz von Quad-Chip-Modulen vorgesehen. Diese Quad-Module bestehen aus vier Auslese-Chips, die über Bump Bonds mit einem großen Silizium-Pixelsensor verbunden sind.

In dieser Arbeit werden erste Prototypen solcher Quad-Module untersucht, die unter Verwendung eines planaren n^+-in-n-Silizium-Pixelsensors und vier FE-I4-Auslesechips gefertigt wurden. Der Fokus der Untersuchungen liegt auf Messung der Ladungssammlung im Labor und der Nachweiseffizienz von Teilchendurchgängen im Testbeam.

Darüber hinaus wird die Entwicklung neuer Pixel-Designs vorgestellt.

Contents

Chapter 1

Introduction

The Standard Model of particle physics is a very good description of the fundamental particles and their interactions in the entire Universe and everything it contains. The Standard Model was confirmed and completed with the discovery of the Higgs boson [1, 2] at the **L**arge **H**adron **C**ollider (LHC).

After 15 years of operation, the LHC will approach its limits in the 2020s. Continued data taking after 2020 would require running times of more than ten years to halve the statistical error of a given measurement [3]. In order to fully exploit the physics potential of the LHC and to continue its successful operation, the LHC will be upgraded during **l**ong **s**hutdown **3** (LS3), starting 2024, to the **H**igh **L**uminosity-**LHC** (HL-LHC). The scheduled timeline is shown in Figure 1.1.

As a result of the upgrade, the HL-LHC is expected to reach an instantaneous luminosity of $5 \times 10^{34}\,\mathrm{cm}^{-2}\,\mathrm{s}^{-1}$ and collect an integrated luminosity of $3000\,\mathrm{fb}^{-1}$ until 2040. Latest research indicate that it should even be possible to achieve an instantaneous luminosity of $7 \times 10^{34}\,\mathrm{cm}^{-2}\,\mathrm{s}^{-1}$ and collect an integrated luminosity of $4000\,\mathrm{fb}^{-1}$ [3]. The studies to be carried out with these data include measurements of Higgs boson properties, vector boson scattering and gauge couplings and searches for physics beyond the Standard Model, including searches for exotic particles and interactions and flavour-changing neutral currents in top-quark decays [5, 6]. Some of these studies can only be carried out at the HL-LHC, as they investigate processes involving very rare decays.

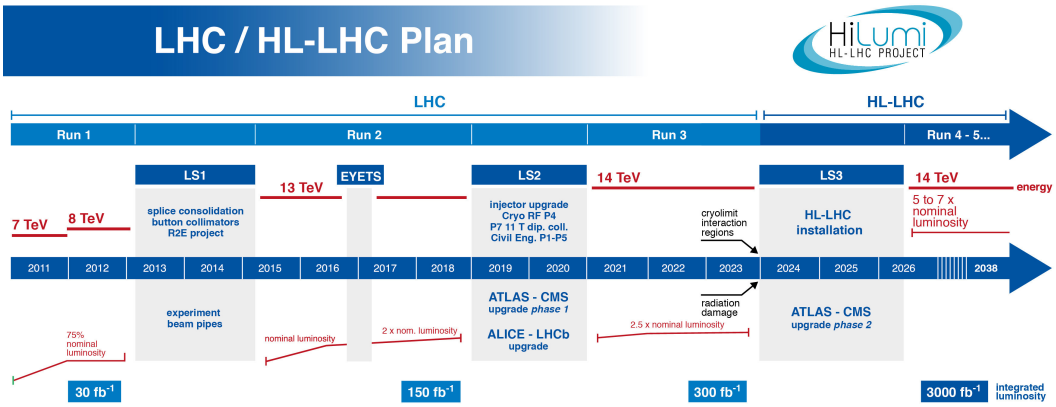

Figure 1.1: The road to HL-LHC, as of July 2017. [4]

The HL-LHC represents a great opportunity for experimental particle physics, but also presents great challenges. The largely increased number of roughly 200 inelastic collisions per beam crossing results in an increased secondary particle flux which increases the radiation damage accordingly. This is valid not only for the detector components of the experiments, but also for the machine parts such as magnets and electronics. Due to the beam-induced heat load, the cooling of components close to the interaction regions will also reach its limits. Therefore, before particles can collide in the HL-LHC, extensive hardware improvements must be made in which many components are either replaced or upgraded.

In order to meet the increased requirements of the HL-LHC and to maintain the same tracking performance, one of the upgrades for the ATLAS experiment is the replacement of the current **I**nner **D**etector (ID) with a new all-silicon **I**nner **T**rac**k**er (ITk). The **T**echnical **D**esign **R**eports (TDRs) for the ITk Strip Detector subsystem [7] and the ITk Pixel Detector subsystem [8] were recently published, marking the final step in the transition from R&D stage into production stage of this project.

This thesis describes the current state of the ATLAS pixel detector and gives an outlook on the development of the new pixel detector system, which is part of the new all-silicon tracker for the ATLAS experiment. Main focus is the investigation of first large area pixel modules, so-called quad chip modules, in the laboratory and at testbeams. These quad modules consist of four read-out chips, bump-bonded to one large pixel sensor. In addition, the development of new pixel designs will be presented.

In chapter 2, a brief introduction on physics of semiconductor sensors and their interaction with matter is given, focusing on silicon as the most important material in detector physics. In chapter 3, a short overview of the accelerator complex at CERN is provided, including details of the important accelerators as well as the main experiments at the LHC. The focus will be on the ATLAS experiment and its upgrades, especially the ITk Pixel Detector. In chapter 4, the sensor technologies and the read-out chips used in the current and in the ITk pixel detector are presented. The structure and composition of the pixel modules is explained on the basis of the investigated quad modules. In chapter 5, the methods for data acquisition and analyses used for the investigations in this thesis are introduced. In addition, facilities frequently used to irradiate modules are briefly presented. In chapter 6, the main results of the investigation of the quad modules in the laboratory and at testbeams are presented, including results before and after irradiation. In chapter 7, studies to improve the pixel design are motivated. A newly created wafer layout and first measurements of its sensors are presented. In chapter 8, the results from the previous chapters are summarized and an outlook is given.

Chapter 2

Silicon semiconductor sensors

Nowadays semiconductor devices are an indispensable part of science and technology. Their development also enriched particle physics, starting with the use of semiconductor sensors to measure particle energies with excellent resolution in spectroscopy, later leading to the development of position-sensitive detectors, which could operate at high rates and allowed high precision measurements of particle tracks.

In this chapter, a brief introduction on the physics of semiconductor sensors is given, focusing on silicon as the most important material. A more detailed view on semiconductor sensors and their applications can be found in literature, e.g. in [9–12].

2.1 Conduction in semiconductors

Silicon crystallizes in a diamond lattice configuration where each atom shares its four valence electrons with the neighbouring atoms in the lattice, forming covalent bonds. The energy levels for the electrons of the single atoms can not be treated separately in such a lattice system. They cannot be the same due to the Pauli exclusion principle. Because of the mutual interactions they split into energy states which differ only in smallest amounts of energy. Groups of such energy states, the energy bands, are separated by forbidden regions called band gaps.

At a temperature of absolute zero only the lower energy bands are filled with electrons. The highest occupied band at this state is filled with valence electrons and therefore called valence band. Their covalent bonds can be broken by thermal excitation or with the application of an external electrical field. This is shown in Figure 2.1a. The electron is thereby lifted into a higher band, where it can move freely and participates in electric conduction. Therefore this next higher energy band is called conduction band. The lifted electrons leave deficiencies, called holes, in the valence band. These defects can be cured if an electron from a neighbouring bond moves to this position, resulting in an effective movement of the hole. This is shown in Figure 2.1b. The holes also contribute to electric conduction but opposite to the electrons as positive charged particle.

The highest energy level of the valence band is named E_V, while the lowest energy level of the conduction band is named E_C. The energy difference between E_C and E_V is called band gap energy E_g. This amount of energy is at least necessary to break a covalent bond and to excite an electron from the valence band into the conduction band. In silicon, the band gap energy at room temperature is 1.12 eV [9], while the mean

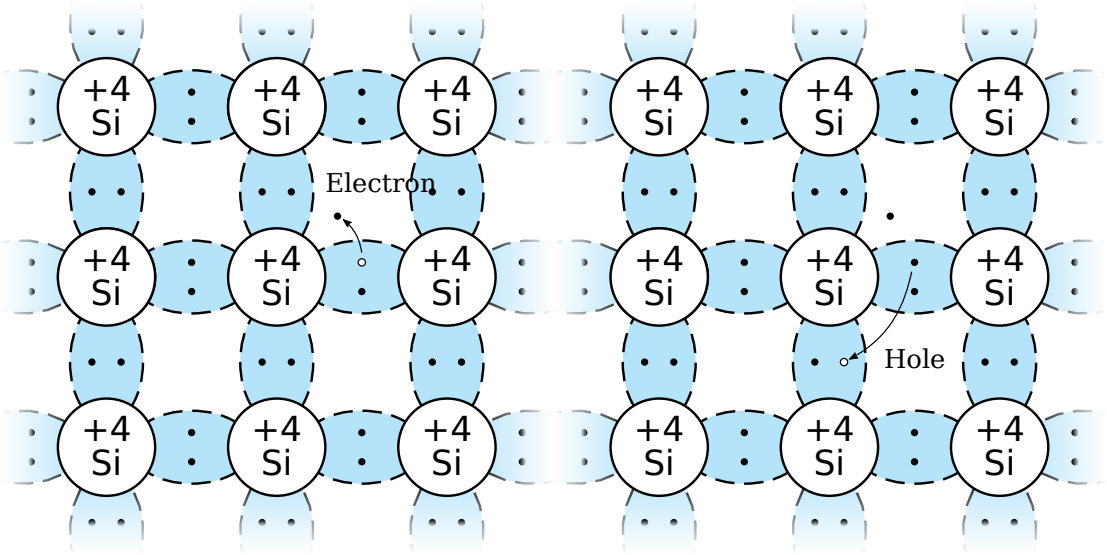

(a) A bond broken by thermal excitation, resulting in a conduction electron and a hole.

(b) The deficiency cured by a neighbouring electron, resulting in a moving hole.

Figure 2.1: The basic representation of conduction in intrinsic silicon, using a schematic two-dimensional representation of the real tetrahedron bond. After [9], Fig. 1.8.

energy necessary to create an electron-hole pair is $(3.62 \pm 0.02)\,\mathrm{eV}$ to $(3.68 \pm 0.02)\,\mathrm{eV}$, depending on the type of the ionizing particle [10]. The difference between these values can be explained by the necessary momentum transfer to the lattice, as in silicon the maximum of the valence band and the minimum of the conduction band do not occur at the same crystal momentum.

The band structure model explains the influences of temperature, pressure, illumination and electric fields on conduction in semiconductors. Each parameter affects either the band gap width or the amount of excited charge carriers. It also explains the good conductivity of metals, where the conduction band at ground state is already partially filled or overlaps with the valence band. In insulators, the band gap is too large to be crossed through thermal excitation.

2.2 Doping and p-n junction

The insertion of impurities in the semiconductor material, called doping, can be used to introduce additional charge carriers. The replacement of a silicon atom with a donor atom is shown in Figure 2.2a. A donor like phosphorus has an additional valence electron, which does not participate in covalent bonding but in conduction. To introduce additional holes, a similar approach can be used, as shown in Figure 2.2b. A silicon atom is replaced with an boron atom, which has three valence electrons. This deficiency is

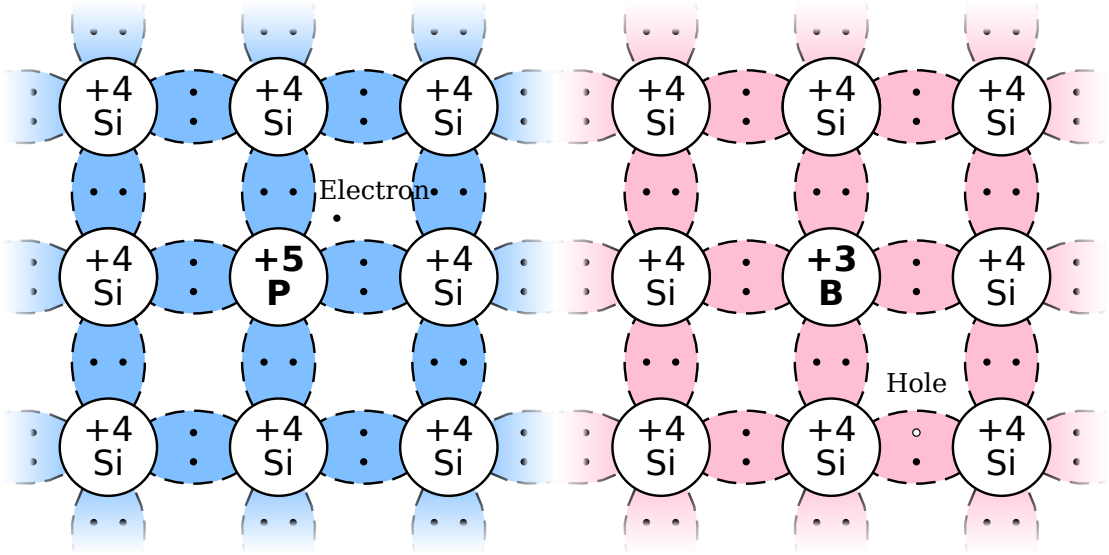

(a) N-type silicon, doped with phosphorus. **(b)** P-type silicon, doped with boron.

Figure 2.2: Schematic bond pictures for (a) n-type silicon with donor and (b) p-type silicon with acceptor. After [9], Fig. 1.19.

cured by a neighbouring electron, leaving a hole. These impurities introduce additional energy levels. For donors they are close to E_C, so the electrons can be ionized easily and are lifted in the conduction band whereas for acceptors their energy levels are slightly above E_V, so they are filled easily with electrons from the valence band, leaving holes. Examples for energies of these levels in silicon are $E_C - 0.045\,\text{eV}$ for phosphorus and $E_V + 0.045\,\text{eV}$ for boron [9].

An excess of either negative or positive charge carriers leads to a reduction of the other type of charge carriers due to recombination. Silicon with donors has additional negative charge carriers and is therefore called n-doped or n-type. If it has acceptors and thus additional positive charge carriers, it is called p-doped or p-type. The doping process does not change the total charge of the semiconductor, as there remains an immovable ion with opposite charge for each mobile charge carrier.

If a semiconductor contains an n-type and a p-type region or if an n-type and a p-type semiconductor are brought together, a p-n junction is formed. The electrons diffuse into the p-type region, while the holes diffuse into the n-type region. This creates an area lacking of mobile charge carriers, which is why it is called depletion zone. The movement is driven by the concentration gradient of electrons and holes in the corresponding areas. They leave behind immobile charged ions, building up space charges. Their potential difference, the so-called built-in voltage V_0, causes an electrical field which forces a current opposite to the diffusion current and finally stops the movement. Comparable considerations can be made for the transition of a highly doped region to a normal doped region of the same type, forming a n^+-n or a p^+-p junction.

2.3 Biasing the p-n junction

The width of the depletion zone in a sensor depends on the biasing condition. In equilibrium condition, the width depends only on the build-in voltage V_0 which results from the initial doping concentration. This is shown in Figure 2.3a. In forward-bias condition, a positive (negative) bias voltage is applied to the p-side (n-side), the built-in voltage is reduced and the depletion zone is shrunk or even vanishes. In reverse-bias condition, a negative (positive) bias voltage is applied to the p-side (n-side), the built-in voltage is increased and the depletion zone is enlarged. The two different biasing conditions are shown in Figure 2.3b and Figure 2.3c. The dependency of the depletion zone width w on the bias voltage V_{bias} can be derived [9, 10] to

$$w = \sqrt{\frac{2\varepsilon\varepsilon_0}{e}\left(\frac{N_A + N_D}{N_A N_D}\right)(V_0 - V_{\text{bias}})} \quad , \tag{2.1}$$

using the elementary charge e, the permittivity of silicon $\varepsilon\varepsilon_0$, the acceptor concentration N_A and the donor concentration N_D. Usually the bias voltage required to fully deplete a sensor of given thickness d, the depletion voltage V_{depl}, is of greater relevance. Setting $w = d$ in Equation 2.1 and rearranging yields

$$-V_{\text{depl}} = \frac{e}{2\varepsilon\varepsilon_0}\left(\frac{N_A N_D}{N_A + N_D}\right) d^2 - V_0 \quad . \tag{2.2}$$

A semiconductor detector device is always operated reverse-biased to enlarge the depletion zone, which gives V_{bias} and V_{depl} a negative sign. Assuming usual simplifications [10], Equation 2.2 shortens to

$$-V_{\text{depl}} \simeq \frac{w^2}{2\varepsilon\mu\rho} \quad . \tag{2.3}$$

The depletion voltage mainly depends on the majority charge carrier mobility μ and of the resistivity ρ of the bulk silicon. Usually high resistive silicon with $1\,\text{k}\Omega\,\text{cm}$ to $15\,\text{k}\Omega\,\text{cm}$ is used for sensors to maintain a low depletion voltage.

While biasing the p-n junction a leakage current can be measured. It is a combination of surface generated current and bulk generated current. The surface current usually

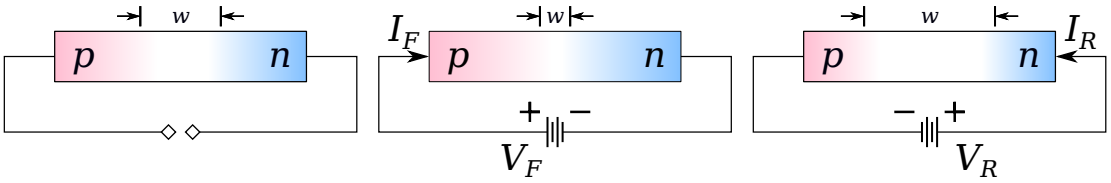

(a) Thermal-equilibrium condition.

(b) Forward-bias condition.

(c) Reverse-bias condition.

Figure 2.3: Schematic representation of depletion zone width of a p-n junction under various biasing conditions. After [9], Fig. 3.8.

makes a small contribution only as it depends rather on the geometry of the surface than on the applied bias voltage. This can change if the surface is heavily contaminated or damaged by scratches.

The main source of the bulk current are electron-hole pairs generated by thermal excitation within the depleted or active volume of the sensor. Since the surface usually does not change, active volume mainly depends on the width of the depletion zone which itself, according to Equation 2.1, depends on the square root of the bias voltage:

$$I \propto \sqrt{-V_{\text{bias}}} \quad . \tag{2.4}$$

The bulk leakage current strongly depends on the temperature. The relation is described by

$$I(T) \propto T^2 \exp\left(\frac{-E_{\text{g}}(T)}{2k_B T}\right) \quad , \tag{2.5}$$

using the band gap energy E_{g}, the Boltzmann constant k_B and the temperature T. It is therefore necessary to normalize measured leakage currents to a standard temperature, especially in the case different measuring setups. The relationship between two currents at different temperatures can easily be derived from Equation 2.5: For a current $I_m(T_m)$ measured at a temperature T_m the current $I(T)$ at the normalization temperature T is determined by

$$I = I_m \cdot \left(\frac{T}{T_m}\right)^2 \exp\left[\frac{-E_{\text{g}}}{2k_B} \cdot \left(\frac{1}{T} - \frac{1}{T_m}\right)\right] \quad . \tag{2.6}$$

2.4 Particle detection with silicon sensors

In order to detect the transit of a particle through a silicon sensor, its generated charge has to be registered by the read-out electronics. For charged particles with lower energies, this charge is mainly deposited by collision effects such as excitation and ionization of atoms, while for charged particles with higher energies it is mainly caused by radiation effects such as bremsstrahlung. The energy E_{crit} is defined as the energy where the contributions of collision and radiation effects to the total energy loss are equal. These energy losses lead to the creation of electron-hole pairs within the detector volume. In the depleted detector region, the free charge carriers do not recombine but drift in the direction of the electrodes due to the applied electric field. In order to achieve the largest charge signal possible, the detector should therefore be operated fully depleted.

Photons in silicon are absorbed through the photoelectric effect or pair production, which releases detectable electrons or positrons in the sensor, or they are deflected through Compton scattering, transferring energy to electrons, which are then detected. Transitions of other non-charged particles are not detected directly by silicon sensors. Absorbing materials in front of the sensors can be used for neutral particles such as neutrons to convert their energy into radiation that is detectable in silicon.

The mean energy loss of charged particles much heavier than electrons can be described in good approximation by the Bethe equation

$$\left\langle -\frac{\mathrm{d}E}{\mathrm{d}x} \right\rangle = \frac{1}{2} K z^2 \frac{Z}{A} \frac{1}{\beta^2} \left[\ln \frac{2 m_e c^2 \beta^2 \gamma^2 W_{\max}}{I^2} - \frac{\beta^2}{2} - \delta(\beta\gamma) \right] \quad , \tag{2.7}$$

where $W_{\max}$ is the maximum possible energy transfer in a single collision, I is the mean excitation energy and $\delta(\beta\gamma)$ is the density-effect correction term. Information on the prefactor, often abbreviated with ξ, and details on the individual terms and derivations can be found in [11–13]. The Bethe formula (2.7) is valid for a ratio $\beta\gamma$ of momentum p and rest mass m_0 between 0.1 and 1000 [13]. At $\beta\gamma \approx 3$, it has a distinctive minimum where the energy loss is lowest. A particle at this energy-loss minimum is therefore called **m**inimum-**i**onizing **p**article (MIP). From this minimum on, the energy loss does not increase significantly until the radiation effects are noticeable. These MIP-like particles generate the smallest possible signal in the detector and are therefore often used as benchmark for sensor tests. The energy loss of electrons and positrons can be described by a formula similar to Equation 2.7. Their energy loss is generally higher than that of heavy charged particles, but for relativistic electrons it is still similar to that of MIPs, e.g. the difference between the energy losses at the ionization minimum is 6.6 % in silicon [11]. However, the critical energy E_{crit} is significantly lower than $\beta\gamma m_0 \approx 1000\,\mathrm{m_0}$, e.g. 37.60 MeV in silicon [11].

An approximation for the energy loss distribution is provided by the convolution of a Landau distribution, parametrised in [11] as

$$\phi(\lambda) = \frac{1}{\pi} \int_0^\infty e^{(-\pi u/2)} \cos\left[u(\ln(u) + \lambda)\right] \, \mathrm{d}u \quad , \tag{2.8}$$

and a Gauss distribution, which can be parametrised as

$$\varphi(x) = \frac{1}{\sqrt{2\pi\sigma^2}} e^{-\frac{(x-\mu)^2}{2\sigma^2}} \quad . \tag{2.9}$$

The highly-skewed convolution distribution is characterised by its maximum value, the most probable energy loss or **m**ost **p**robable **v**alue (MPV) and by an asymmetric long tail in the high energy region, which is mainly caused by rare high-energy δ-rays. The value Δ_p of the most probable energy loss can be calculated according to

$$\Delta_p = x\xi \left[\ln \frac{2mc^2\beta^2\gamma^2}{I} + \ln \frac{x\xi}{I} + j - \beta^2 - \delta(\beta\gamma) \right] \tag{2.10}$$

where x is the detector thickness in $\mathrm{g\,cm^{-2}}$ and j is an empirical factor, for which a value of 0.200 is given [13, 14]. The remaining quantities correspond to those in Equation 2.7. The most probable energy loss has a logarithmic dependence on the traversed detector thickness. In order to determine the expected charge signal in a detector, its thickness must therefore be taken into account.

The mean value and the MPV are theoretically very well predicted by Equation 2.7 and Equation 2.10, but in experimental distributions the mean is affected by outliers like very rare high-energy transfer collisions or escaping δ-rays. These shift the mean value while the MPV remains unaffected, as it is derived from the frequency of the charge signals. The MPV is thus the more stable characteristic and is therefore preferred in examinations.

2.5 Radiation damage in silicon

In addition to the energy loss caused by ionization, described in section 2.4, particles can also transfer their energy directly to the lattice atoms of a silicon sensor. These so-called **n**on-**i**onizing **e**nergy **l**oss (NIEL) interactions can dislocate the **p**rimary **k**nock-on **a**tom (PKA) from its lattice position to an interstitial (I) position. A vacancy (V) in the lattice is left behind. This formation of an interstitial close to a vacancy is called Frenkel pair (V-I). These basic defects are shown in Figure 2.4. If a sufficient amount of energy is transferred, the PKA can displace further atoms, causing large defect clusters.

The primary point defects, interstitials and vacancies, are mobile at room temperature [15] and are therefore unstable. On the one hand, they can anneal when an interstitial fills a vacancy. On the other hand, they can form new defect complexes with other existing defects, which are then stable at room temperature. Examples for such complex defects are the combination of two vacancies to a divacancy (V_2), the combination of a vacancy with a donor or an acceptor atom to an E-center (V-P/V-B) or the combination of a vacancy with oxygen to an A-center (V-O).

The defects have a strong effect on the properties of a sensor. Recombination-generation centers increase the leakage current by the alternating emission of electrons and holes. Trapping centers capture charge carriers and release them with varying time

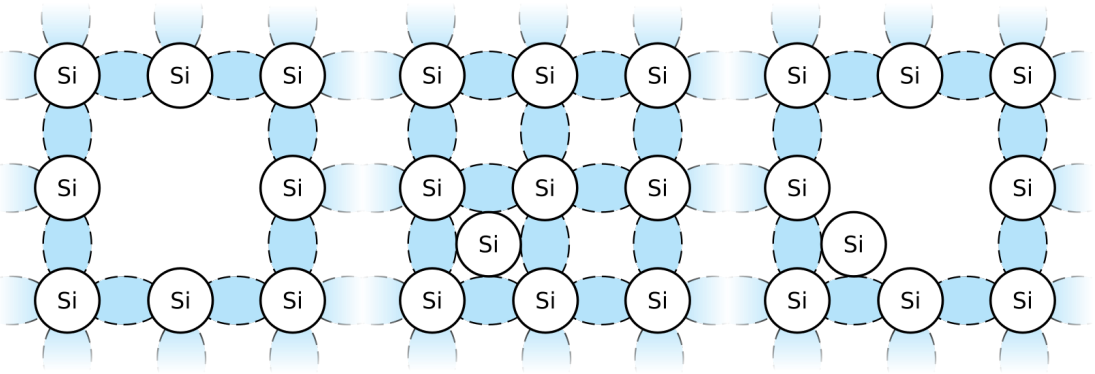

(a) A vacancy in the lattice. **(b)** An atom in interstitial position in the lattice. **(c)** A vacancy and an interstitial forming a Frenkel pair in the lattice.

Figure 2.4: Schematic representation of primary lattice defects in silicon.

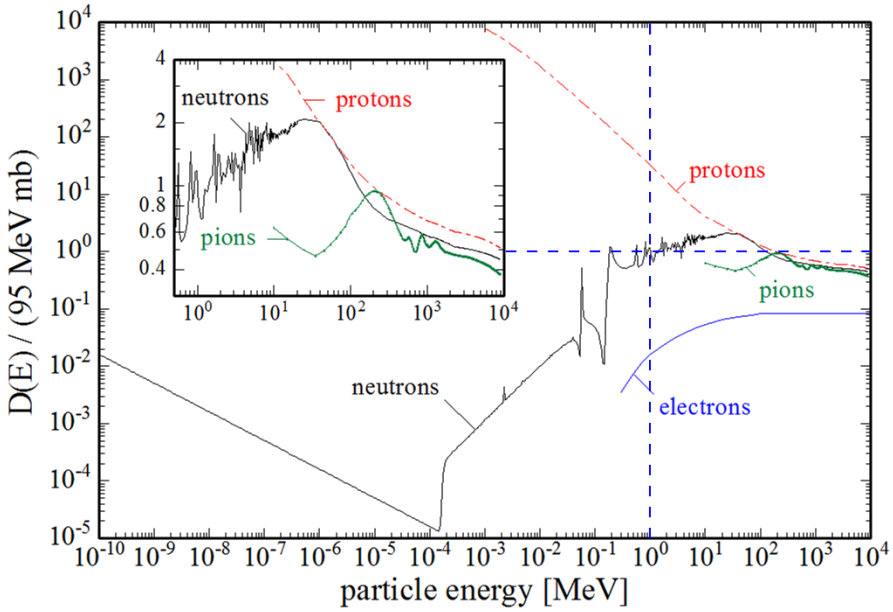

Figure 2.5: Non-ionizing energy loss (NIEL) in silicon for different particle types, normalized to 1 MeV neutrons [17]. The dashed lines illustrate the normalizing value.

constants. Due to this delay they may be lost for detection. Donors and acceptors can be removed, and therefore change the effective doping concentration and thus the depletion voltage. More details about defects and their impacts can be found in literature, e.g. in [11, 12, 15–17].

The damage caused by radiation depends strongly on the particle energy and the particle type. It is described by the energy-dependent displacement damage cross-section or damage function $D(E)$. This function is plotted against the particle energy for protons, neutrons, pions and electrons in Figure 2.5. The NIEL scaling hypothesis states that radiation damage depends only on the number and the energy of PKAs. Therefore, the damage function is used to normalize fluences Φ_x from different irradiations to a 1 MeV neutron equivalent fluence Φ_{eq} with help of the hardness factor κ:

$$\Phi_{\text{eq}} = \kappa \cdot \Phi_x \quad . \tag{2.11}$$

The hardness factor can be calculated [16] as

$$\kappa = \frac{\int D_x(E)\phi_x(E)\mathrm{d}E}{D_n(1\,\text{MeV}) \int \phi_x(E)\mathrm{d}E} \quad , \tag{2.12}$$

using the damage function $D(E)$ and the spectral fluence $\phi_x(E)$.

NIEL scaling works reliably for leakage currents. However, for other effects such as change of effective doping concentration, violations of the NIEL scaling hypothesis were observed [17].

Chapter 3

The accelerator complex at CERN

In 1957 the **S**ynchro-**C**yclotron (SC), the first accelerator at CERN, the European Organization for Nuclear Research, started delivering particles to experiments, followed shortly by the **P**roton **S**ynchrotron (PS). This marked the beginning of over 60 years of particle and accelerator physics. While the SC has nowadays become a very impressive light show to improve public relations, the PS is still an important part of the accelerator chain as a result of continuous upgrades and improvements. The complete accelerator complex at CERN and all the experimental facilities it servers are shown in Figure 3.1.

In this chapter, an overview of the accelerator complex at CERN is provided. Details of the important accelerators as well as the main experiments at LHC are presented.

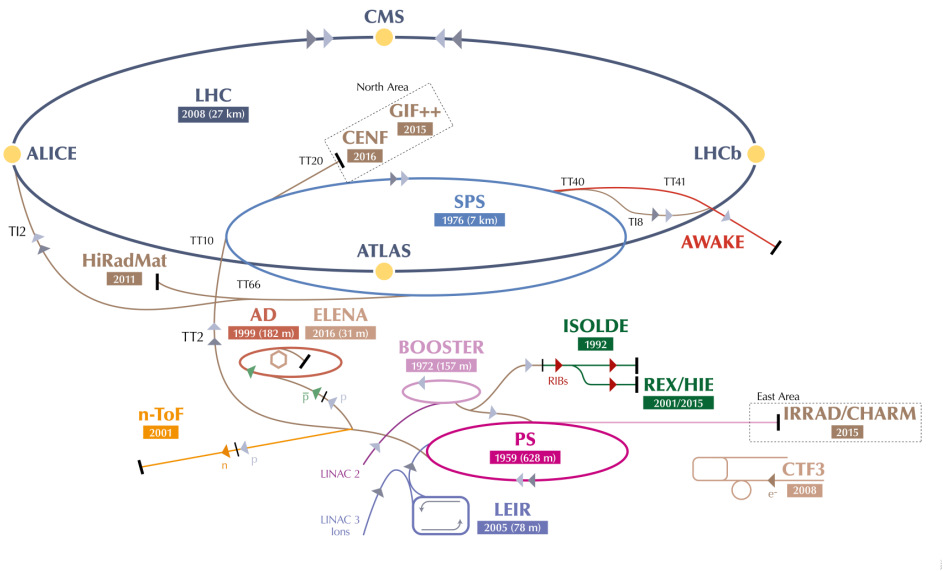

Figure 3.1: The CERN accelerator complex. [18], modified.

3.1 Important accelerators and experimental areas

3.1.1 PS – The Proton Synchrotron

The PS is a synchrotron with a circumference of 628 m. It is one of the first alternating-gradient synchrotrons, using the strong focusing principle. By the end of 1959 protons reached an energy of 24 GeV for the first time [19].

Nowadays, pre-boosted protons are injected in the PS. After acceleration the protons are transferred to the **S**uper **P**roton **S**ynchrotron (SPS) or delivered to the experiments or the irradiation facility in the East Area.

3.1.2 East Area

The East Area is part of the PS complex. It is an experimental area located in CERN building 157. After the conclusion of the experimental program and the decommissioning of the DIRAC experiment [20] in 2012, the area was refurbished and the existing proton irradiation facility IRRAD1 [21], operating since 1992, was upgraded [22, 23].

Nowadays, the area comprises four beam lines. Three of these are dedicated to test beams, while one is dedicated to the irradiation facilities IRRAD[1] and CHARM[2]. Like the old facility, the new one uses 24 GeV protons delivered from the CERN-PS. In addition to the usual irradiation at room temperature, the facility offers the possibility of irradiation under operational conditions, where the devices are powered and/or cooled. The standard beam size is $12 \times 12\,\mathrm{mm}^2$ **f**ull **w**idth at **h**alf **m**aximum (FWHM) but it can be spread out to $20 \times 20\,\mathrm{mm}^2$ FWHM. The protons are delivered in spills of roughly 4×10^{11} p, which is about four times the intensity of the previous IRRAD1 facility. Present requirements for the irradiation of ATLAS pixel modules are fluences in the range of $0.5 \times 10^{16}\,\mathrm{n_{eq}\,cm^{-2}}$ to $1.5 \times 10^{16}\,\mathrm{n_{eq}\,cm^{-2}}$ and a spread beam in order to irradiate this large-area devices as homogeneously as possible. In 2017 an average of 50 days, including stops and beam efficiency, was needed to reach $1 \times 10^{16}\,\mathrm{p\,cm^{-2}}$ with a $20 \times 20\,\mathrm{mm}^2$ beam [24].

3.1.3 SPS – The Super Proton Synchrotron

The SPS is a synchrotron with a circumference of 6.9 km. Like the PS, it uses conventional electromagnets, operated at room temperature. Being commissioned in 1976 it is nowadays a further link in the accelerator chain [25].

The acceleration of protons is continued up to an energy of 450 GeV. Then the protons are delivered either to the LHC and its experiments or to the beamlines leading to the experiments and test beam facilities in the North Area.

[1] `www.cern.ch/ps-irrad`
[2] `www.cern.ch/charm`

3.1.4 North Area

The North Area is a secondary beam line complex located at CERN's Prévessin site in France. The proton beam from the SPS is divided into three parts and directed at three targets. These are used to convert the primary proton beam into secondary particle beams, mainly of pions, electrons or muons. This secondary beams are shared between seven beam lines, leading to the three experimental halls EHN1, EHN2 and ECN3. The beam energy can be selected with the help of magnets [26].

In addition to various experiments such as COMPASS and SHINE, mainly test beam campaigns for detector development for the LHC experiments are carried out in the several experimental areas per beam line in the North Area. For testbeam investigations of ATLAS pixel modules, the beamline H6 is mainly used, which features a pion beam of typically 120 GeV. Beam telescopes are permanently installed in its H6A and H6B areas to ensure high spatial resolution during examinations.

3.1.5 LHC – The Large Hadron Collider

The LHC is a two-ring superconducting hadron accelerator and collider with a circumference of 26.7 km [27]. Two opposing proton beams are brought into collision at four intersection points. First collisions occurred in 2009 with beams with a particle energy of 3.5 TeV each. Since then, all beam parameters were improved. In 2017 collisions occurred at a center-of-mass energy of 13 TeV with a peak luminosity of more than $2 \times 10^{34}\,\mathrm{cm}^{-2}\,\mathrm{s}^{-1}$, which allowed an accumulation of more than $100\,\mathrm{fb}^{-1}$ since initial commissioning [28].

3.2 Detector systems at the LHC

3.2.1 ATLAS

The ATLAS (**A** **T**orridial **L**HC **A**pparatu**S**) experiment [29] is one of two multi-purpose detectors at the LHC. It is 44 m long, has a height of 25 m and a total weight of approximately 7000 t. All important components are shown in Figure 3.2. Characteristic for the ATLAS detector are the coils of the toroid magnet and the muon wheels. The layout is similar to other hermetic detectors: The interaction point is surrounded by the tracking system, giving vertex and momentum information due to the applied magnetic field. The next detector elements are the electromagnetic and the hadronic calorimeters for energy measurement and finally the muon system, so that these particles can be identified before they leave the detector. All systems have a cylindrical barrel area which is enclosed on both sides by so-called end caps.

Inner Detector (ID)

The ID is cylindrical around the beam pipe with a length of 7.0 m and a radius of 1.1 m. Its three subsystems are embedded in a 2 T magnetic field, which is generated by the

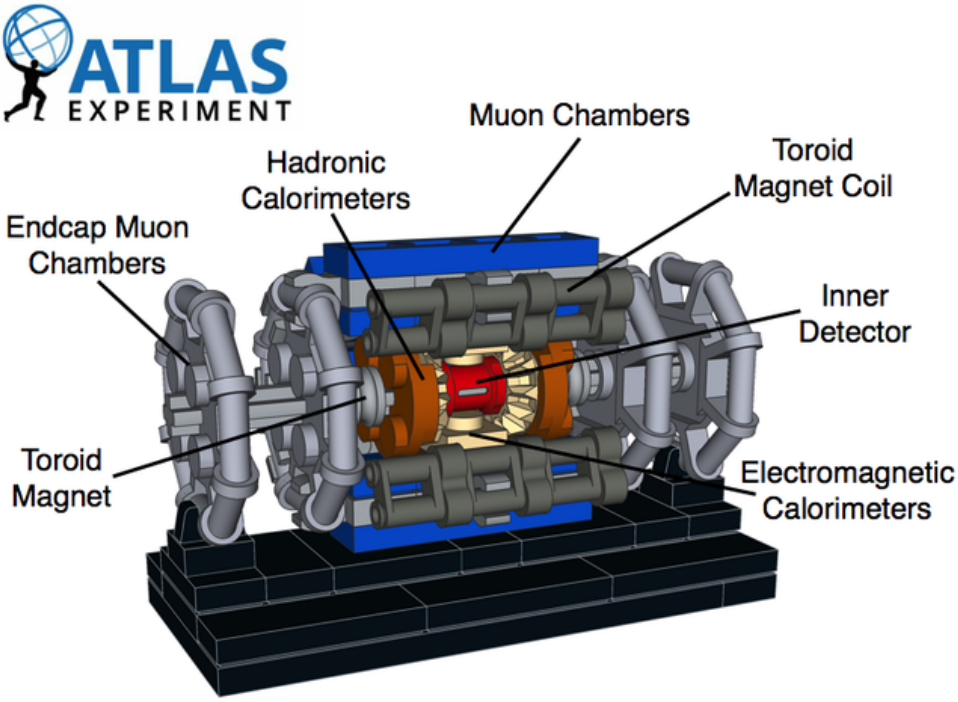

Figure 3.2: The ATLAS experiment. Simplified schematic view. [30]

central solenoid, to deflect charged particles. Their impulse can then be deduced from the bent track. A cross section of the ID components in the barrel region is shown in Figure 3.3. The innermost pixel layer, the **I**nsertable **B**-**L**ayer (IBL), is installed close to the beam pipe since the phase-0 upgrade in 2014. Still close to the interaction point are the three original layers of the pixel detector. Next are the four double strip layers. Each of these layers consists of a slightly twisted pair of sensors. The ID is completed by up to 73 layers of drift tubes. Due to the small angle of incidence, adjustments are necessary in the end cap region. The layout is basically retained but the sensors are no longer parallel but perpendicular to the beam pipe.

Pixels: The three-layer pixel detector consists of 1744 n^+-in-n silicon sensors with a thickness of 250 µm. To form a module, 16 **f**ront-**e**nd (FE) read-out chips thinned to 180 µm thickness are bump-bonded to each sensor. For technical reasons, there are gaps between the individual readout chips. The nominal pixel size is $50 \times 400\,\mu m^2$, but to cover the gap in the direction of the long pixel side between two read-out chips, the edge pixels in every row are extended to a length of 600 µm. To cover the gap in the direction of the short pixel side between two read-out chips, four pixels in every column are connected via a metal trace to four pixels without dedicated read-out channels. This results in a total pixelated area of $60.8 \times 16.4\,mm^2$ with 46 080 readout channels per

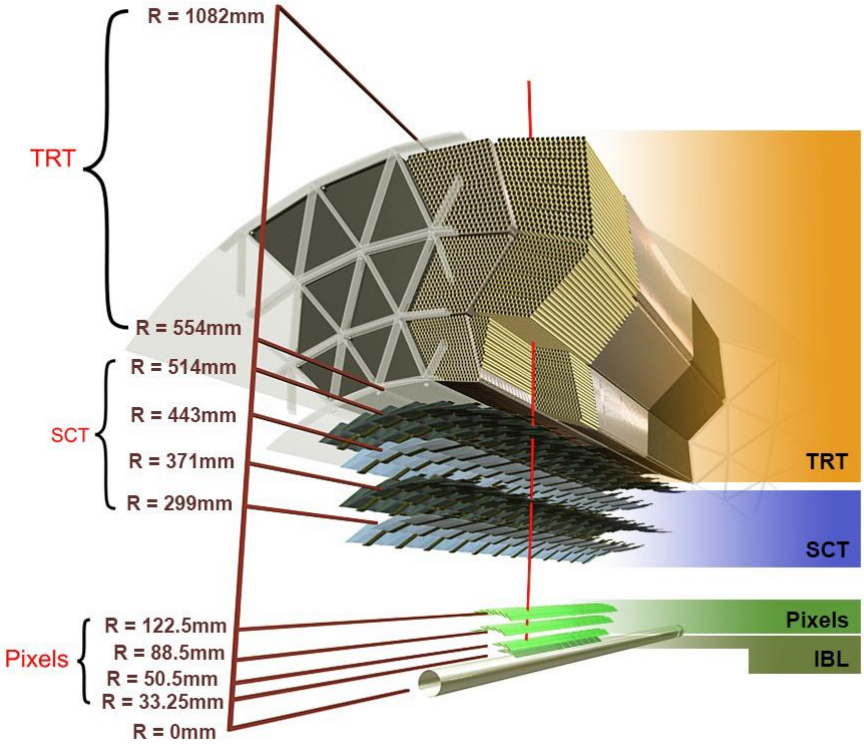

Figure 3.3: Sketch of the ATLAS inner detector showing all its components, including IBL. The distances to the interaction point are also shown. [31]

module.

All pixel modules are designed to withstand a fluence up to $1 \times 10^{15}\,\mathrm{n_{eq}\,cm^{-2}}$, which is expected at the innermost layer at its end-of-life. In order to be sufficiently efficient even after this irradiation, a bias voltage of up to 600 V can be applied. To reduce the resulting leakage current, the modules can be cooled to operating temperatures down to $-10\,°\mathrm{C}$.

The IBL will be introduced in subsection 3.3.1. Details on the ATLAS pixel sensor technology will be given in chapter 4.

Semiconductor Tracker (SCT): The **S**emi**c**onductor **T**racker (SCT) consists of 15 912 AC-coupled silicon strip sensors, single-side processed in p-in-n technology. The sensor thickness is 285 µm. The strips have a pitch of 80 µm for the rectangular sensors in the barrel region, and also a mean pitch of 80 µm for the trapezoidal sensors in the end cap region. To form a module, up to four sensors are glued back-to-back on a base board. The front and back are rotated with respect to each other by 40 mrad to increase space-point resolution. The resulting 4088 modules are loaded with a readout hybrid

which contains 12 128-channel **a**pplication-**s**pecific **i**ntegrated **c**ircuits (ASICs).

The SCT modules are designed to withstand a maximum fluence of $2 \times 10^{14}\,\mathrm{n_{eq}\,cm^{-2}}$, which is expected the SCT region at end-of-life.

Transition Radiation Tracker (TRT): The **T**ransition **R**adiation **T**racker (TRT) is a drift chamber detector. Its 4 mm diameter polyimide straw tube elements are filled with a $Xe/CO_2/O_2$ mixture. In between are polypropylene fibres to generate transition radiation. The transition radiation helps to distinguish electrons and hadrons by their different signal amplitudes.

The total number of readout channels is approximately 351 000. The TRT is operated at room temperature.

Electromagnetic and hadronic calorimeter

The ID is located within two sampling calorimeter systems. The high granularity electromagnetic calorimeter uses **l**iquid **ar**gon (LAr) as active and lead as passive detector medium in the barrel and the end cap region. Its accordion-shaped geometry is ideally suited for energy measurements of electrons and photons, as it offers complete coverage without gaps in the radial direction. The total thickness is at least 22 radiation lengths (X_0). Its experimentally measured fractional energy resolution after noise subtraction is $\frac{\sigma_E}{E} = \frac{10\,\%\sqrt{\mathrm{GeV}}}{\sqrt{E}} \oplus 0.17\,\%$ for electrons.

The hadronic **tile cal**orimeter (TileCal) in the barrel region uses steel as absorber and scintillator tiles for detection, segmented into three layers. In the wheels used in end cap region the detector media are changed to copper and LAr. The total thickness is about 11 interaction lengths (λ) at a perpendicular angle. The fractional energy resolution for a combined LAr and TileCal measurement, obtained at a pion testbeam, is $\frac{\sigma_E}{E} = \frac{52.0\,\%\sqrt{\mathrm{GeV}}}{\sqrt{E}} \oplus \frac{1.6\,\mathrm{GeV}}{E} \oplus 3.0\,\%$.

An additional special **f**orward **cal**orimeter (FCal) is installed in the end caps. Its electromagnetic module uses copper, its two hadronic modules use tungsten as absorber materials. The detector medium for all modules is LAr. The experimentally measured fractional energy resolutions after noise subtraction for the FCal are $\frac{\sigma_E}{E} = \frac{28.5\,\%\sqrt{\mathrm{GeV}}}{\sqrt{E}} \oplus 3.5\,\%$ for electrons and up to $\frac{\sigma_E}{E} = \frac{94.2\,\%\sqrt{\mathrm{GeV}}}{\sqrt{E}} \oplus 7.5\,\%$ for pions.

All calorimeters provide information for the **L**evel-**1 calo**rimeter trigger (L1Calo).

Muon spectrometer

The muon spectrometer surround the calorimeters. They are immersed in the magnetic field provided by the superconducting air-core toroid. This system not only measures the tracks and momenta of particles passing the calorimeter, but also provides signals for the **L**evel-**1 muon** trigger (L1Muon). Tracking is performed by drift tube chambers, using an Ar/CO_2 gas mixture. They are interspersed with fast trigger chambers with a space-time resolution of $1\,\mathrm{cm} \times 1\,\mathrm{ns}$.

The information of both L1Calo and L1Muon are handled in a central trigger processor. It provides the final Level-1 (LVL1) accept decision, which is distributed to trigger the read-out of the detector front-ends [32]. This first, hardware-based trigger decision is necessary to significantly reduce the initial event rate of 40 MHz by selecting only physically interesting event candidates. The event rate is later further reduced by software triggers.

3.2.2 CMS

The other multi-purpose detector at the LHC is the CMS (**C**ompact **M**uon **S**olenoid) experiment [33]. It is 22 m long, has a height of 15 m and a total weight of approximately 12 500 t. This makes it much denser than ATLAS. A sketch is shown in Figure 3.4b. Like ATLAS, the detector layout is based on the usual rules for hermetic detectors, but the implementation is considerably different. Core element of CMS is the central superconducting 4 T solenoid, large enough to house the tracking system and the calorimeters. The return field of the solenoid is used to bend the tracks in the muon chambers.

The CMS inner tracker consists of a three-layer pixel detector and a ten-layer microstrip detector. These are made of 1440 n^+-in-n silicon pixel modules with a nominal pixel size of $100 \times 150\,\mu m^2$ and of 15 148 p-in-n silicon strip modules with a strip pitch of 80 µm on the inner layers and 120 µm on the outer layers.

Energy determination is realized by an electromagnetic homogeneous calorimeter using lead-tungstate crystals ($PbWO_4$) and a hadronic sampling calorimeter using brass as passive detector medium and scintillator tiles for detection. Their total thicknesses are $25\,X_0$ and 7–11 λ, respectively.

The muon system uses drift tubes and cathode strip chambers for tracking and resistive plate chambers for triggering.

3.2.3 ALICE

The ALICE (**A** **L**arge **I**on **C**ollider **E**xperiment) experiment [34] is also a general-purpose detector but it is specialized on studying lead-lead or lead-proton collisions. The LHC delivers this collisions for a couple of weeks, usually at the end of the year. The detector is 26 m long, has a height of 16 m and a total weight of approximately 10 000 t. A sketch is shown in Figure 3.4c. The asymmetric layout features a central barrel part and a forward muon spectrometer arm.

The barrel part is within the reused 0.5 T normal conducting solenoid magnet of the L3 experiment. It houses a six layer silicon vertex detector, a time projection chamber and a transition radiation detector for tracking as well as two different electromagnetic calorimeters. One of them is dedicated to photons with energies in a wide dynamic range of 0.005 GeV to 80 GeV. The barrel part features no dedicated hadronic calorimeter.

The forward muon detector uses the usual tracking planes and triggering chambers.

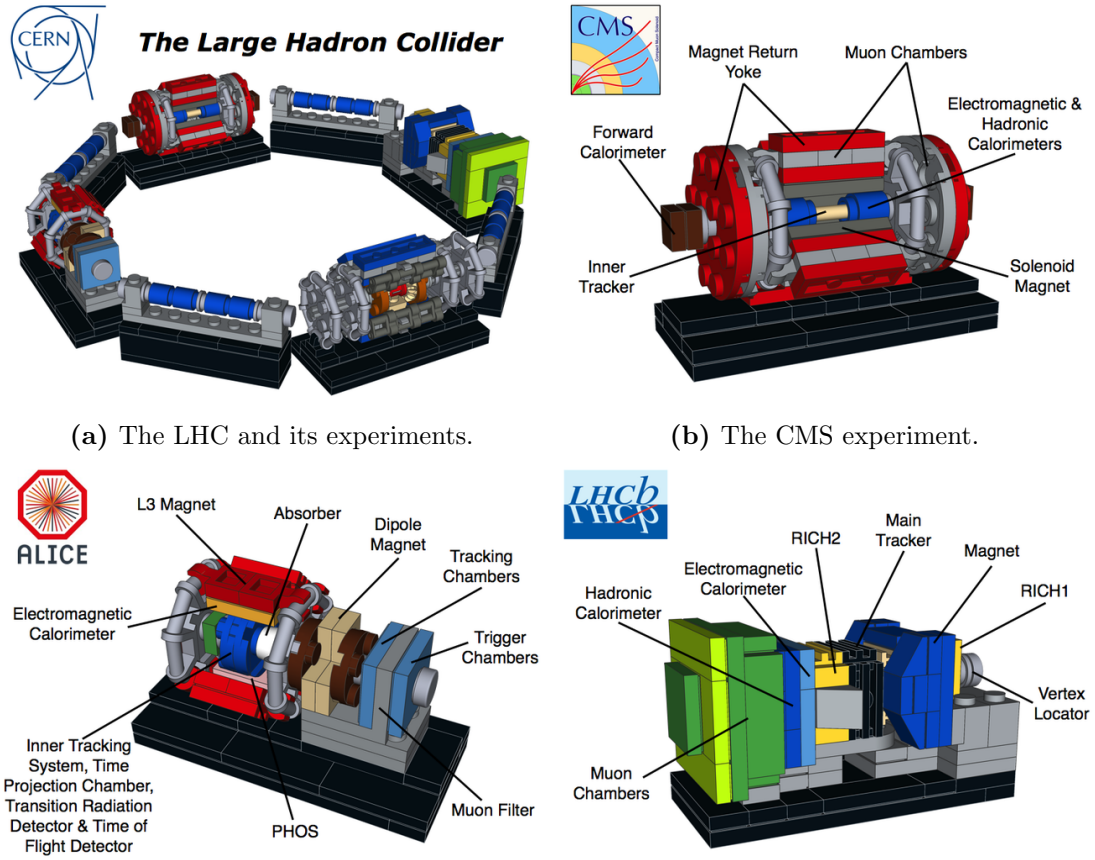

(a) The LHC and its experiments.

(b) The CMS experiment.

(c) The ALICE experiment.

(d) The LHCb experiment.

Figure 3.4: The LHC and its other experiments. Simplified schematic views. [30]

3.2.4 LHCb

The LHCb (**LHC-b**eauty) experiment [35] is specialized to precision measurements of CP violation and rare decays of beauty and charm hadrons at the LHC. It is 21 m long, 12 m wide, has a height of 10 m and a total weight of approximately 5600 t. A sketch of the detector is shown in Figure 3.4d. The layout is designed for a detailed investigation of b-hadrons, which are predominantly produced in a narrow cone along the beam axis. The single-arm detector therefore covers an angle of 10 mrad to 300 mrad from the collision point.

Tracking is performed by a vertex locator system closest to the collision point and a silicon tracking system after a spectrometer magnet. The particle identification is supported by **r**ing-**i**maging **Ch**erenkov (RICH) detectors, especially to distinguish pions and kaons. Next are electromagnetic and hadronic calorimeter, and the muon chambers.

3.3 Upgrades of ATLAS tracking systems

3.3.1 Phase-0 upgrade – IBL

Since the initial start-up in 2008, major parts of the LHC and its experiments have been refurbished, modernized and upgraded. During **l**ong **s**hutdown **1** (LS1) the **I**nsertable **B**-**L**ayer (IBL) [36, 37] was installed in ATLAS in 2014 [38]. Its 14 staves form an additional pixel layer, closest to the beam pipe. The stave layout of the chosen mixed sensor scenario is shown in Figure 3.5. The central region is populated with twelve planar n^+-in-n sensors while the two stave extremities are populated with four 3D sensors. For their read-out, a new generation of front-end electronics, the FE-I4 ASIC, was developed [39] which features a smaller pixel pitch and a larger pixel matrix, leading to 26 880 read-out channels per chip.

The IBL is designed to withstand a fluence of $5 \times 10^{15}\,\mathrm{n_{eq}\,cm^{-2}}$ and an ionising dose of 2.5 MGy. The operating temperature can be down to −15 °C.

The planar sensors [40] are based on the very well known and reliable sensors of the three-layer pixel detector [41], but their design layout was revised [42] to reduce the width of the inactive edge. Also their pixel size was shrunk to $50 \times 250\,\mu\mathrm{m}^2$ and the pixel matrix was enlarged to be suitable to the new read-out chips. The sensors have a thickness of 200 µm and each is read out by two FE-I4, thinned to 150 µm thickness. To cover the gap between these two read-out chips, the edge pixels in every row are extended to a length of 500 µm.

The 3D sensors [43] are based on a novel concept for radiation hard silicon sensors. They are placed at the stave extremities due to their vertical electrode orientation. To increase production yield, the sensor size fits to one FE-I4.

Both sensor technologies will be introduced in detail in section 4.1

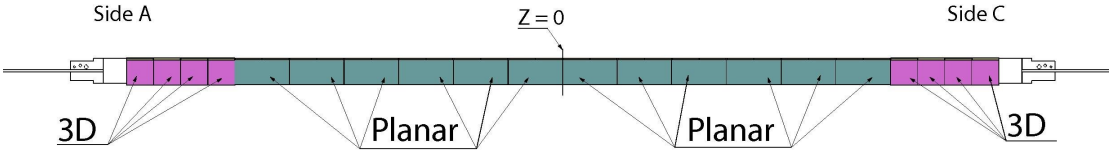

Figure 3.5: Layout of an IBL stave for the chosen mixed sensor scenario. The total length is 724 mm. [38]

3.3.2 Phase-2 upgrade – ITk

To cope with the increased luminosity, data rate and radiation damage at the HL-LHC [3], major upgrades of the ATLAS experiment are necessary and foreseen [44, 45]. One upgrade will be the replacement of the current inner detector with a new all-silicon tracker, starting in 2024. The proposed new **I**nner **T**rac**k**er (ITk) is designed to operate under conditions featuring an increased track density, following from approximately $\langle\mu\rangle = 200$ inelastic proton-proton collisions per beam crossing, and a high radiation

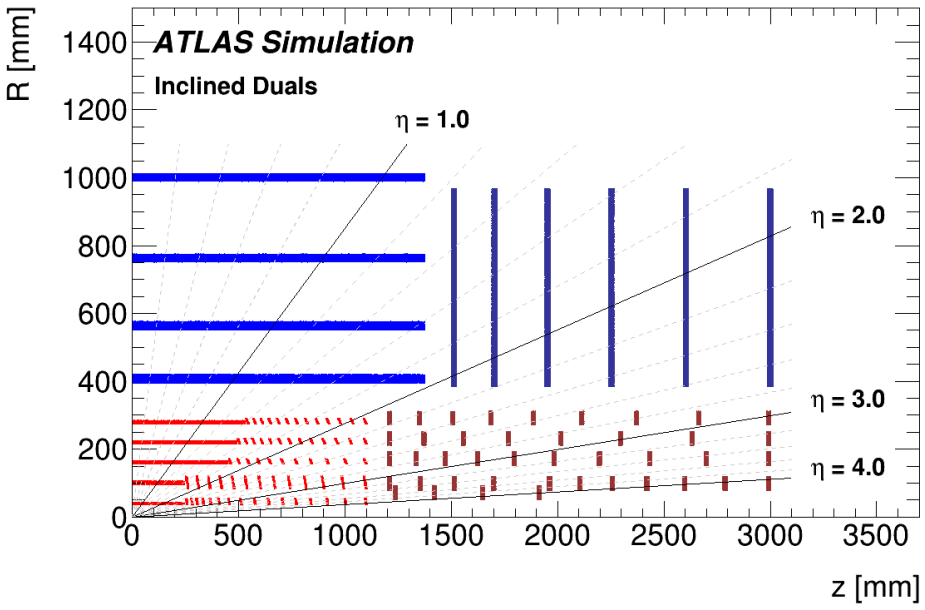

Figure 3.6: Schematic representation of one quadrant of one of the possible ITk layouts. The sensors of the barrel and end-cap Strip Detector are shown in blue and in dark blue, respectively. For the Pixel Detector the sensors are shown in red for the barrel layers and in dark red for the end-cap rings. [8]

dose estimated from the expected integrated luminosity of $4000\,\mathrm{fb}^{-1}$ over twelve years of operation. A more detailed description can be found in the TDRs for the Pixel Detector subsystem [8] and the Strip Detector subsystem [7].

The ITk will be an all-silicon tracker with five pixel and four strip layers in the central region, enclosed by end-caps with six strip disks and a number of pixel rings on each side. A schematic representation of one quadrant of one of the possible ITk layouts is shown in Figure 3.6 which features the pixel layout as presented in [8]. The use of quad chip modules is foreseen in the pixel barrel layers with the exception of the innermost layer and in the rings of the pixel end-cap area. Due to the high track density resulting from the high number of collisions, the track separation capability must be increased. For this reason, pixel pitches of $50 \times 50\,\mu\mathrm{m}^2$ or $100 \times 25\,\mu\mathrm{m}^2$ are considered, resulting in better track resolution compared to the previous detector. The final layout of the Pixel Detector is expected to be concluded by July 2018.

Radiation background simulations [8] predict fluences of $1.3 \times 10^{16}\,\mathrm{n_{eq}\,cm^{-2}}$, including a safety factor of 1.5, after an integrated luminosity of $2000\,\mathrm{fb}^{-1}$ for the innermost layer. Due to this high fluence, the barrel layers *0* and *1*, including the corresponding end-cap region, are designed to be exchangeable. An exchange will probably take place after half of the planned runtime. The maximum predicted fluence for the outer barrel layers and the end-cap disks is $3.8 \times 10^{15}\,\mathrm{n_{eq}\,cm^{-2}}$ after an integrated luminosity of $4000\,\mathrm{fb}^{-1}$, also

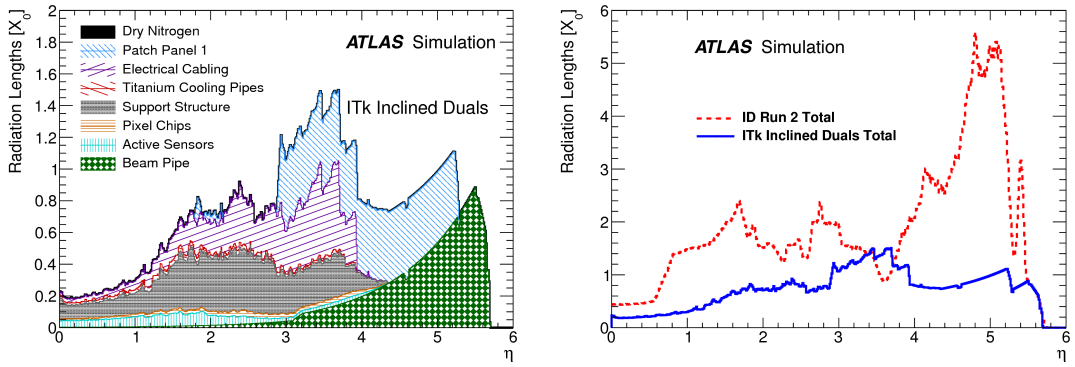

(a) Material distribution for the ITk.

(b) Comparison of the Material distribution of the ITk and the current Inner Detector.

Figure 3.7: Material distribution in terms of radiation length X_0 as a function of the pseudorapidity η. [8]

including a safety factor of 1.5. No replacement is planned for these detector regions, as they are not easily accessible.

With growing distance from the interaction point, the radiation damage is increasingly caused by particles backscattered in the detector. For this reason, but also because of the great influence on the tracking performance, the material budget is reduced as much as possible. A simulation of the material distribution of the ITk is shown in Figure 3.7a. A comparison of this material distribution to the one of the current Inner Detector is shown in Figure 3.7b. The significant improvement results primarily from the reduced material budget of the patch panels, the electrical cabling and the supporting structures.

All these improvements will be made to increase physics performance in identifying charged particles and measuring of their properties while operating under HL-LHC conditions. An example for the improved momentum resolution is shown in Figure 3.8a for muons. Especially at large transverse momenta, the greater precision in the muon momentum measurement of the ITk compared to the current Inner Detector is visible.

Another improvement is the increased efficiency to identify τ-leptons, which is shown in Figure 3.8b for the τ reconstruction from jets containing one associated track (1-prong) for different selection cuts. It also shows the higher angular coverage, which is increased from $\eta = 2.5$ in the current Inner Detector to $\eta = 4.0$ in the ITk by extending the pixel end cap region as shown in Figure 3.6. A similar result for the τ reconstruction from jets containing three associated tracks (3-prong) can be found in [8].

When studying physic channels containing photons, like $H \to \gamma\gamma$ events, the conversion of photons to electron-positron pairs in the detector volume by pair production must be taken into account. The reduced probability for photon conversions in the ITk, shown in Figure 3.8c, is a direct result of the reduced material distribution, shown in

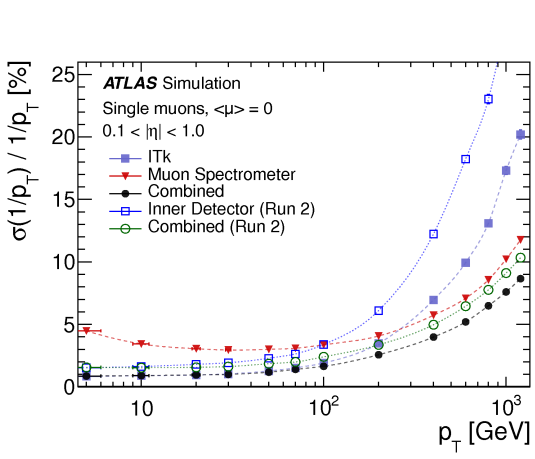

(a) Combined muon momentum measurement and the individual contributions from the ITk and the Muon Spectrometer.

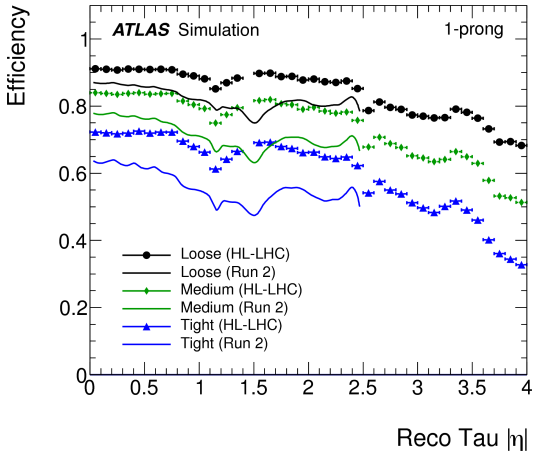

(b) Identification efficiency for 1-prong τ-leptons versus the pseudorapidity η.

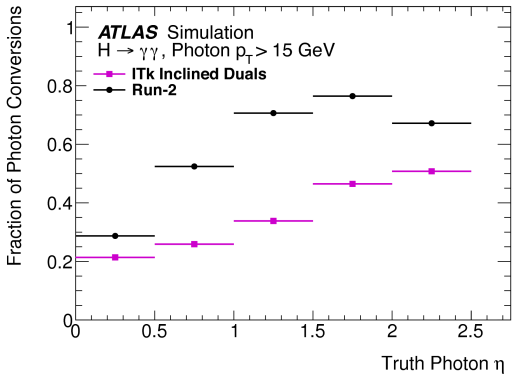

(c) Probability for a photon to covert when traversing the detector.

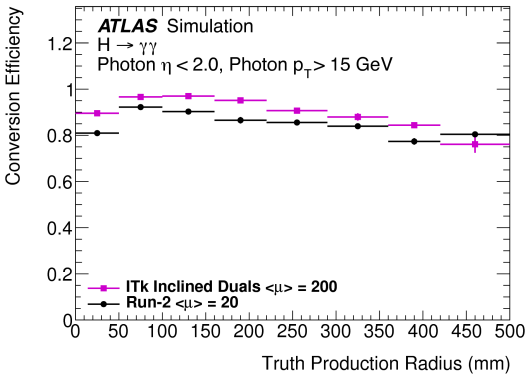

(d) Photon conversion reconstruction efficiency at the expected pileups.

Figure 3.8: Examples for the improved performance of the ITk in comparison to the Run 2 detector [8].

Figure 3.7. To increase the overall photon reconstruction performance, the secondary tracks originating from these photon conversions are reconstructed. The reconstruction efficiency of these converted photons is shown in Figure 3.8d.

In conclusion, the ITk is expected to perform even better in an even harsher environment than the current Inner Detector.

Chapter 4

ATLAS pixel detector modules

As described in chapter 2, the detection of particles using silicon is based on signal creation within the depleted region of a pn-junction. These signals are amplified and digitized by specialised read-out circuits. To cope with the the high collision rates of modern particle physic experiments and the resulting radiation damage, state of the art detectors use the hybrid concept, where individual sensors and read-out chips are connected by either conductive or capacitive coupling. This enables independent research on both components.

The current research also addresses the development of monolithic detectors which unite sensor and readout electronics [46], which are described elsewhere.

4.1 Sensor technologies

4.1.1 Planar n^+-in-n

Except for the stave extremities of IBL, the current ATLAS pixel detector consists of planar n^+-in-n silicon pixel sensors. A schematic cross section of such a sensor is shown in Figure 4.1. Each processed wafer side has five different layers. Each of these layers requires a different mask during the photolithography process. A high-resistivity, lightly n-doped wafer is used as bulk material. On the front or n-side the pixel matrix is formed

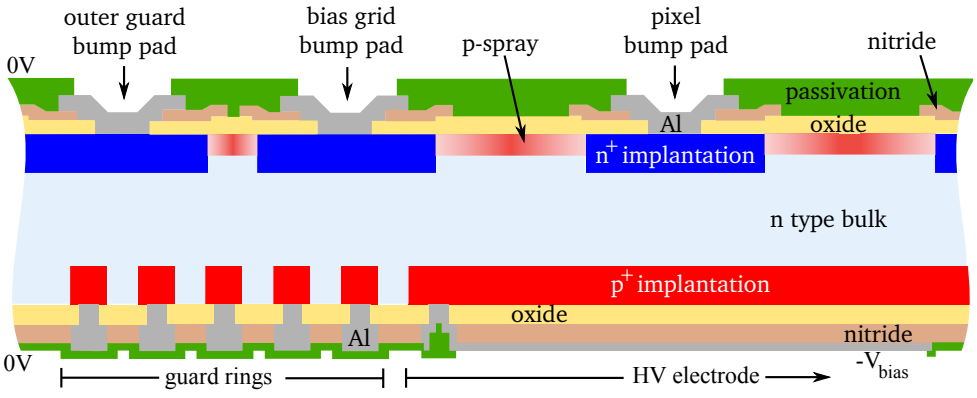

Figure 4.1: Schematic cross section of a n^+-in-n ATLAS pixel sensor. [47]

by an n^+-implantation layer, which is shielded by an oxide passivation layer and an inner nitride passivation layer. After these steps the p-spray, a homogeneous p-doping, is applied to the n-side. The p-spray concentration is higher than the concentration in the bulk but much lower than the concentration in the pixel implants, so it is compensated within the pixels, affecting only the area among them, leading to an electrical isolation. To improve breakdown behaviour, the p-spray profile has a concentration gradient. Openings in the nitride layer leads to high dose application in the central region between pixels, otherwise the dose is reduced by the nitride layer. Therefore the technique is called moderated p-spray. The next layer is used to create conductive connections. Its metal traces connects the n-implant with the pads leading to read-out. The final part is formed by the outer nitride passivation layer which is only punctuated by openings for bump bonding.

The processing of the back or p-side consists of comparable steps. One large p^+-implant serves for the application of **h**igh **v**oltage (HV). Since there is a conductive connection to the n-side through the cutting edge, this HV pad is surrounded by **g**uard **r**ings (GRs), which ensure safe potential reduction until the cutting edge. Details about ATLAS pixel sensors can be found in [47, 48].

A disadvantage of this technology is the two-sided wafer process, which requires additional masks and production steps, leading to increased costs.

4.1.2 Planar n-in-p

In this technology, a lightly p-doped wafer is used as bulk material. The processing of the n-side is comparable to the n^+-in-n technology, but here the pixel matrix is surrounded by the guard rings. Because of that the p-side can be realised as one unsegmented p^+-implantation which requires no masks. Therefore it is called single-sided process.

Less masks translates into reduced costs which makes this technology a promising candidate for most pixel layers in ITk [49, 50].

A disadvantage of this technology is the high voltage on the pixel side, very close to the read-out chip. Therefore additional passivation is added, since electric discharges could damage the electronics.

4.1.3 3D

This technology follows a different approach. Unlike planar, the surface is punctuated with vertical electrodes. This allows smaller distances between the electrodes, leading to higher field strength and thus requires lower operation voltages, even after irradiation. Their radiation hardness up to full HL-LHC fluences has been shown [51]. A comparison of the charge collection in planar and 3D sensors is shown in Figure 4.2. The decoupling of active thickness and collection distance is highlighted.

Disadvantages of this technology are the high production costs and the reduced production yield due to the more complex manufacturing process.

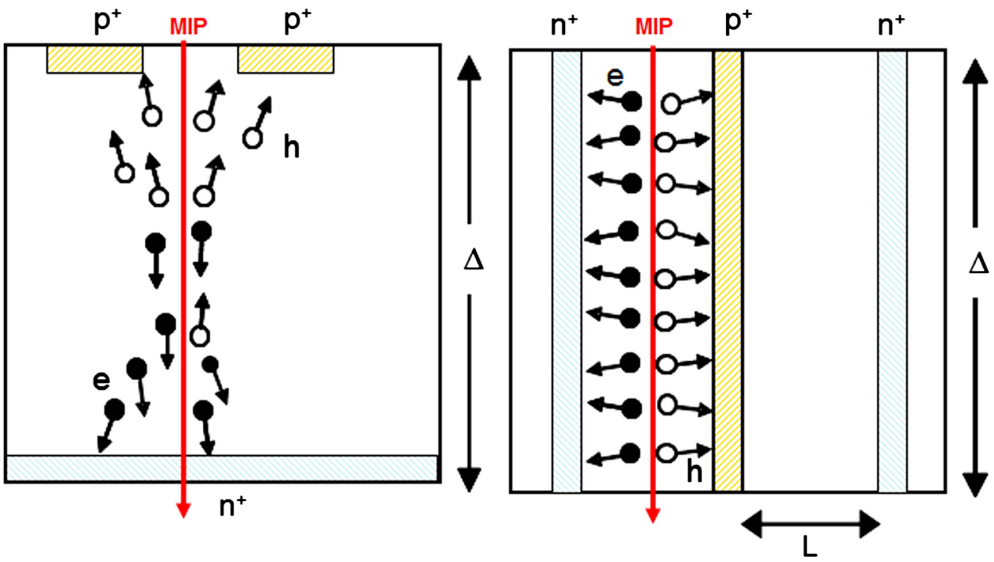

Figure 4.2: Schematic cross-sections of (left) a p-in-n planar sensor, and (right) a 3D sensor, emphasizing the decoupling of active thickness (Δ) and collection distance (L) in 3D sensors. [43]

4.2 Read-out chips

4.2.1 FE-I3

The FE-I3 read-out chip [48] was developed for the application in the ATLAS pixel detector. It is used in the three original barrel layers and the end caps. The chip features 2880 pixel cells, arranged in 18 columns with 400 µm pitch and 160 rows with 50 µm pitch, produced by means of a commercial 0.25 µm feature size **c**omplementary **m**etal–**o**xide–**s**emiconductor (CMOS) process. Its external dimensions are $7.6 \times 10.8\,\mathrm{mm}^2$. It became available in late 2003. It was also used for sensor research until it was replaced by the FE-I4.

4.2.2 FE-I4

The FE-I4 read-out chip [39, 52] is the successor of the FE-I3 and used in the IBL. Compared to its predecessor, it offers a much larger size while the inactive area is reduced. An engineering version, the FE-I4A, was fabricated in 2010. Due to its outstanding performance, only minor design modifications were necessary for the production version, the FE-I4B, which became available in 2011. Both chips features 26 880 pixel cells, arranged in 80 columns with 250 µm pitch and 336 rows with 50 µm pitch, produced by means of a commercial 130 nm feature size CMOS process. Its external dimensions are $20 \times 19\,\mathrm{mm}^2$.

The schematic layout of the analogue circuit of a FE-I4 pixel cell is shown in Figure 4.3.

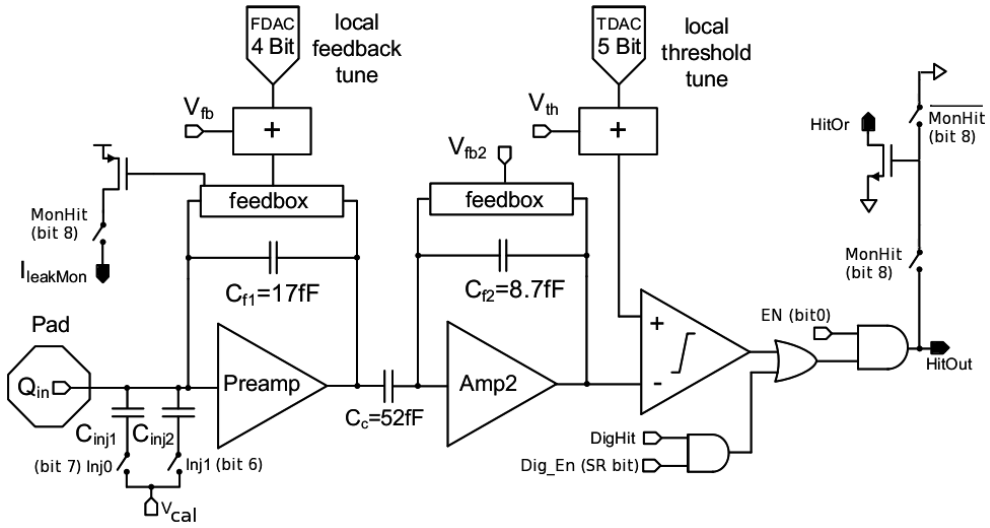

Figure 4.3: Detailed schematic diagram of the analogue circuit of a pixel cell. [52]

Each read-out cell connects to the sensor via its bump bond pad. For testing purposes, the sensor signal can also be simulated by the controlled charging of two injection capacities. The signal reaches a two-stage charge sensitive preamplifier, followed by a discriminator. Both the feedback current of the amplifier and the threshold of the discriminator are independently adjustable to change the shape of the digitized signal. On the one hand, there are global settings that change the response of all pixels. On the other hand, there are also local settings with which each pixel response can be adjusted individually.

If an amplified signal from the sensor exceeds the threshold, the **t**ime **o**ver **t**hreshhold (ToT) is measured in units given by an external clock, usually in **b**unch-**c**rossing **u**nits (BCUs) which uses the LHC clock cycles of 25 ns. This ToT is therefore directly related to the induced charge in the sensor. For large signals, the rise time of the amplifier until the signal exceeds the threshold can be neglected. For small signals, with a ToT of 1 or 2, it is possible that the signal only exceeds the threshold after one or more BCU due to a slow rise. It is therefore measured later than it was induced. This effect is known as timewalk.

Regions of two by two analogue pixels form the simplest digital unit. It stores the hit and ToT information as well as a time counter until a trigger arrives or the hit is discarded.

The nominal voltages required for operation are 1.5 V for the analogue circuit and 1.2 V for the digital circuit. While these voltages can be applied externally, the chip features two Shunt-LDO voltage regulators, which can generate the operation voltages from a single external support line.

4.2.3 RD53A

The RD53A read-out chip [53], developed by the RD-53 collaboration[1], is not intended to be used in experiments, but it is the basis for the production version of future read-out chips for both ATLAS and CMS, thus it is the prototype for the ITk read-out chip. The chip features 76 800 pixel cells, arranged in 400 columns with 50 µm pitch and 192 rows with 50 µm pitch, produced by means of a commercial 65 nm feature size CMOS process. Its external dimensions are $20 \times 11.8\,\mathrm{mm}^2$. First chips became available in December 2017.

Compared to the FE-I4, it not only has a much denser pixel matrix, but also significantly higher data transfer rate of $1.28\,\mathrm{Gbit\,s^{-1}}$. This is necessary to be able to reconstruct all tracks even at the increased collision rate in the HL-LHC.

4.3 Module assembly

The hybridisation of sensor and read-out chip makes use of a flip-chip process employing tin-lead or indium bumps. For preparation, an **u**nder-**b**ump **m**etallisation (UBM) must first be applied to the corresponding spots on sensor and read-out chip to ensure good electrical and mechanical connection. The bump bond balls are distributed on the read-out chip, which is flipped and positioned onto the sensor. The connection is established by heating of the solder balls during the reflow soldering process. The entire technique requires the highest precision. To ease this, alignment marks are implemented on the sensor surface. This procedure is generally valid for the assembly of hybrid modules. For the IBL modules it is described in detail in [38].

Flip-chipping is the cost-driving step in module assembly. In addition to the monolithic approach, current research is therefore also investigating novel connection methods in which sensor and chip are capacitively coupled via a thin glue layer [54].

The connection of a module to the outside world is realized in the detector by flexible **p**rinted **c**ircuit **b**oards (PCBs). They hosts and routes the signal and supply lines with low material costs. Rigid PCBs are therefore used for measurements in the laboratory and at testbeams. In addition to their robustness, they also offer further possibilities to examine a module.

4.4 Quad module prototypes

4.4.1 Modules

Sensor layout

Several 4" sensor wafers were produced at CiS[2] using the n^+-in-n technology with moderated p-spray isolation, which is described in subsection 4.1.1, and a wafer layout

[1] `https://www.cern.ch/RD53`
[2] CiS Forschungsinstitut für Mikrosensorik GmbH, Erfurt, Germany

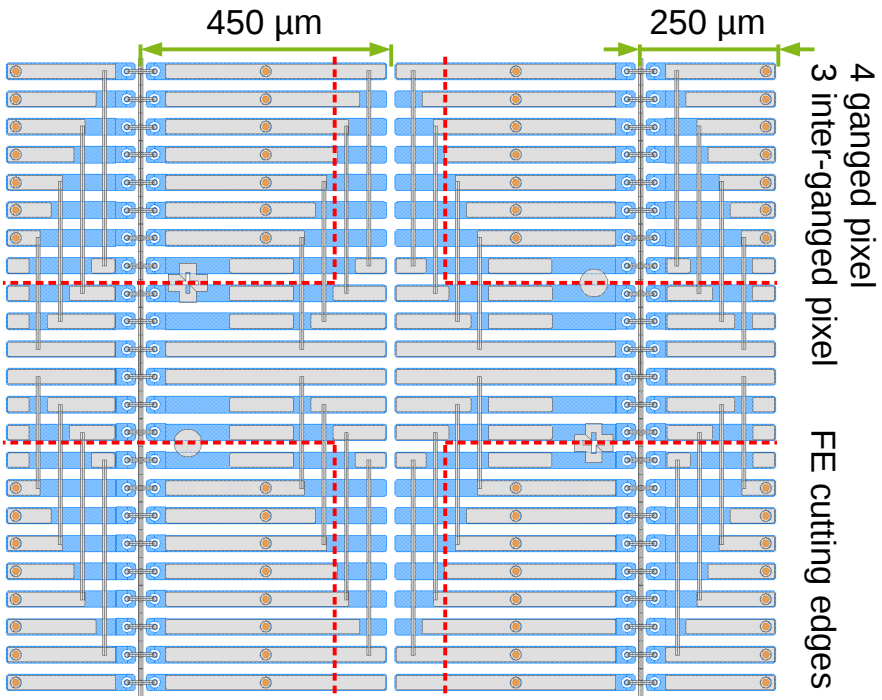

Figure 4.4: Schematic layout of the sensor central region with 'ganged', 'inter-ganged', 'long ganged' and 'long inter-ganged' pixel cells. The n^+ implantation is displayed in blue, the metal in grey and the orange circles represent openings for the bump bond connections. For the sake of clarity, the other layers are not visible. The two crosses and dots are alignment marks to ease the flip-chip process. The red dashed lines represent the FE edges.

referenced as MNPix01. The n-bulk thickness is 285 µm. One wafer features two identical quad sensors. Each of them matches the size of four read-out chips. For technological reasons, two of these chips should not touch each other, so there are gaps in the horizontal and the vertical direction. To be able to detect particles also in these regions, there are different types of special pixels implemented in the sensor layout. To cover the gap in the direction of the columns between two read-out chips, two 'long' pixels are extended to a length of 450 µm in every row. To cover the gap in the direction of the rows between two read-out chips, in every column four 'ganged' pixels are connected via a metal trace to four pixels without dedicated read-out channel, with three 'inter-ganged' pixels in-between. The 'inter-ganged' pixels are standard $250 \times 50\,\mu m^2$ pixel cells with a own dedicated read-out channel. As their performance could be influenced by the metal trace running over them or by crosstalk of the 'ganged' pixels enclosing them, they are treated separately. The layout of the middlemost region of the sensor is shown in Figure 4.4, where the combination of these designs leads to special pixels like 'long-ganged' pixels. The edges of the FE chips are indicated by a red dashed line. To reduce the inactive

sensor area, the width of the HV pad is reduced by 250 µm on each side. This results in the very first and last pixel column being located entirely beneath the guard rings. These columns, together with the very first and the very last row, are referred to as 'edge' pixels.

If all these pixels are taken into account, the sensor consists of 160×680 individual pixels with the external dimensions of $40.4 \times 34.0\,\mathrm{mm}^2$, resulting in 108 800 read-out channels and a total sensitive area of $13.736\,\mathrm{cm}^2$.

Re-dicing of front-end chips

To form a quad module, four FE-I4B were bump-bonded at IZM[3] to such a sensor. The FE-I4B read-out chip was developed for the IBL and already introduced in subsection 4.2.2. On the top it has 86 wire bond pads, each 62 µm high. They are only connected for initial tests and are not necessary for operation. They do not represent a challenge for IBL's double-chip modules, but due to the tight gap between the read-out chips on quad modules, FEs used for quad assembly have to be re-diced.

The implementation of four ganged pixels allows a maximum distance of 200 µm per FE from the topmost pixel to the dicing edge. In a first dicing attempt, the chips were cut at a distance of 150 µm from the topmost pixel, as a compromise between distance and safety margin. The cut went through the top row pads, which is in principle not a problem, since they are only meant for testing purposes, but there was a failure of all FEs after bump bonding. It was revealed that this cut led to short circuits between power and ground layers of the FE, which are on top of each other in the pads. After intense investigations it turned out that more aggressive dicing, which means removing the remaining parts of the top row pads, eliminates the shorts. This final cut distance was finally set to 80 µm from the topmost pixel. The temporary damaged chips returned to be operational after the re-dicing step [55].

4.4.2 PCB

For easy handling a custom made PCB is used which was developed at IFAE Barcelona[4]. Two quad modules were glued and wirebonded to such PCBs at University of Göttingen. An image of a PCB loaded with a quad module is shown in Figure 4.5. The quad module is in the middle. Its four FEs are numbered clockwise, starting with FE1 at the bottom left of the sensor.

On the left side there are the four connectors for data transmission. Commands are only sent via the FE1 connector and then simultaneously distributed to all FEs on the card. Therefore, this must always be connected during measurements, even if FE1 is excluded or not operated. Also on the left side is the 8-pin Molex connector for **l**ow **v**oltage (LV) supply. Its upper leftmost pin is used for ground, its direct neighbour for

[3] Fraunhofer-Institut für Zuverlässigkeit und Mikrointegration IZM, Berlin, Germany
[4] Institut de Física d'Altes Energies, Barcelona, Spain

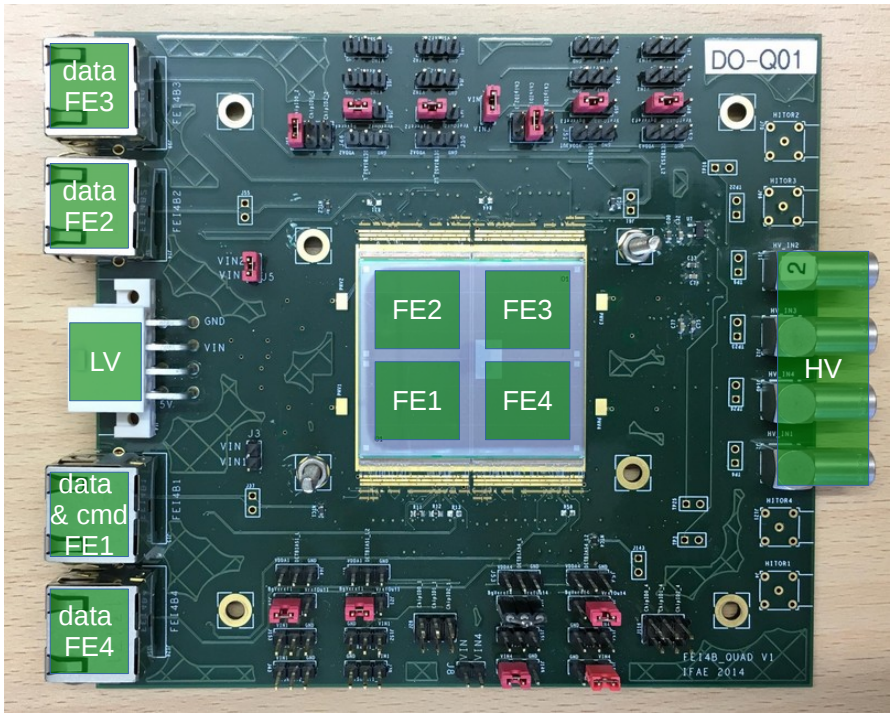

Figure 4.5: Top view of a loaded quad PCB.

power connection. All other pins are unused. Each FE can be connected to this power line via a 2-pin jumper.

On the right side there are four connectors for bias voltage supply, as the card is also designed for use with four **s**ingle **c**hip **m**odules (SCMs). For quad modules, only one of these is connected to a power supply.

Four **n**egative **t**emperature **c**oefficient (NTC) temperature resistors are located close to the module to provide environmental information.

The thickness of the PCB is 1.5 mm. It has four rectangular openings of $1.0 \times 0.8\,\mathrm{cm}^2$ beneath the middle of each read-out chip to reduce material budget to ease the passing of particles. A few PCBs have an additional opening beneath the center of the sensor.

Chapter 5

Methodology

Various read-out systems are available for the operation of FE-I4 modules. This chapter introduces the methods for data acquisition and analyses used for the investigations in the laboratory and at testbeams in this thesis. In addition, facilities frequently used to irradiate modules are briefly presented.

5.1 Read-out systems

5.1.1 USBpix

Multiple read-out systems are available for FE-I4 based modules. For measurements in the laboratory, the *USBpix* [56] system was used. An image of a setup using a gen. 2 **M**ulti-**IO** board (MIO2) with a **B**urn-**I**n **c**ard (BIC) is shown in Figure 5.1. The MIO2 provides connection to various adapter cards. It hosts a USB microcontroller (µC) which

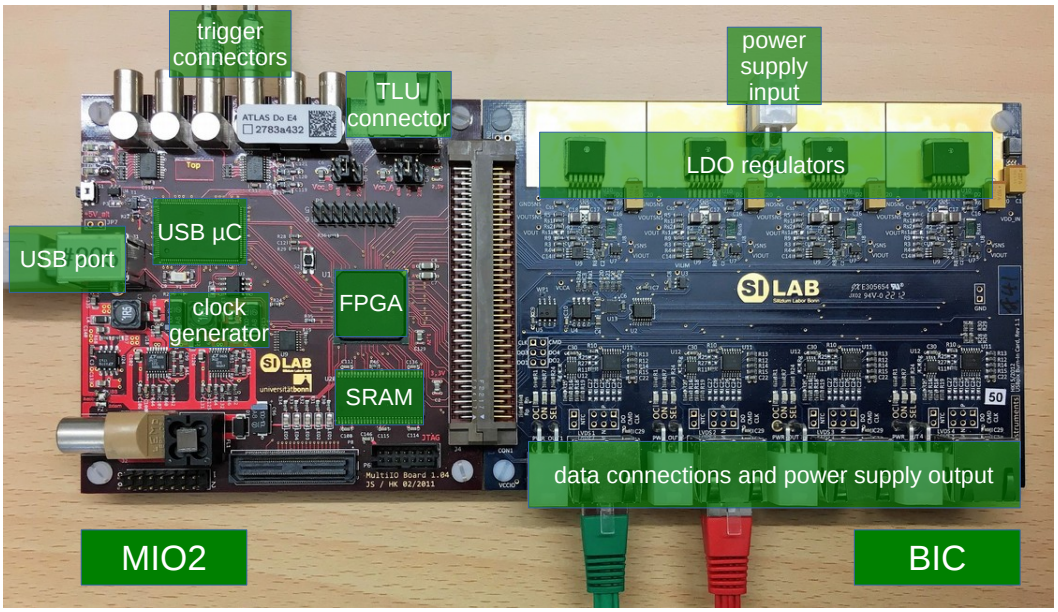

Figure 5.1: USBpix setup using a Multi-IO board with a Burn-In card.

provides an interface to the programmable FPGA. External asynchronous SRAM extends the FPGA memory by 16 Mbit. There is also a clock generator to emulate the 40 MHz clock of the LHC and connectors for trigger logic, either LEMO or RJ-45.

The BIC allows parallel operation of up to four FE-I4 chips. Their command and data lines are connected via the RJ-45 sockets using standard Ethernet cables. There are also four voltage regulators which can provide four independent output voltages from the input voltage, but this feature is usually not used since the FEs are powered directly.

The **g**raphical **u**ser **i**nterface (GUI) for this system is given by *STcontrol* [57]. The software allows to initialize and operate the hardware, but also to update the firmware. In addition, it also provides the configuration files for the front-ends and scans and tuning algorithms to test and alter the configuration parameters of the front-ends.

5.1.2 RCE

Another read-out system is *RCE* [58], which was used for all measurements in testbeams. The components of the setup are pictured in Figure 5.2. Main component is the HSIO-II development board. It requires a 12 V power supply and a Gigabit Ethernet connection to its host computer. A pixel interface board is attached to the Zone 3 interface connector. It hosts 18 RJ-45 connectors, allowing parallel operation of up to 18 FE-I4 chips.

The GUI for this system is given by *calibGui*. While this system is based on plain text configuration files which could be edited by every simple text editor, it is also used to run predefined scans and primlists to test and alter the configuration parameters of the front-ends.

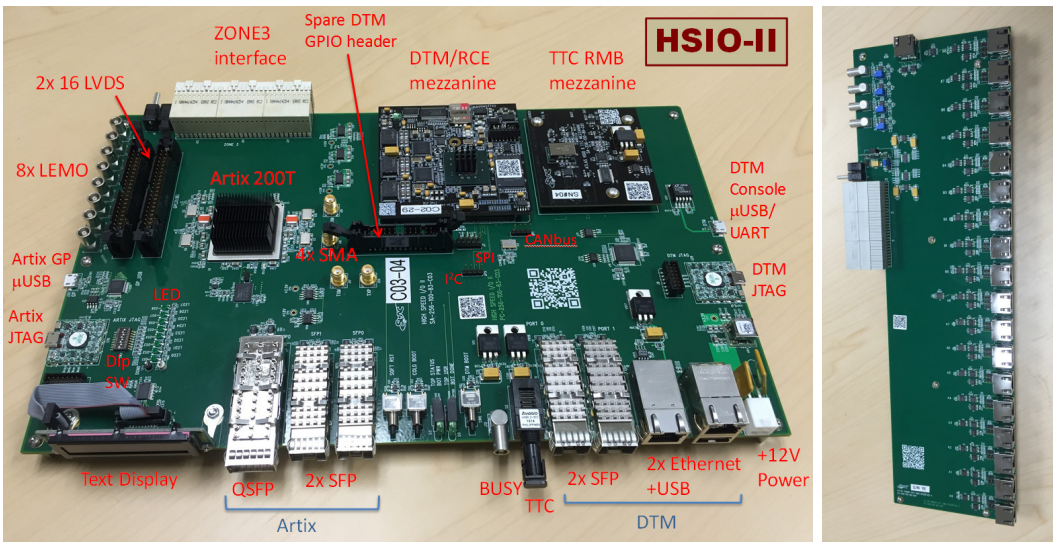

(a) The HSIO-II development board.

(b) Pixel interface board.

Figure 5.2: RCE setup using a HSIO-II and a pixel interface board. [59]

5.2 Operation of FE-I4 modules

5.2.1 Tuning procedure

There are minor differences in the electronic components of an FE-I4 due to the production process. They are also influenced by external effects such as temperature or radiation. Therefore the chip features various **d**igital/**a**nalog **c**onverters (DACs), which can be altered to guarantee homogeneous responses under different operating conditions. The corresponding values of the DACs are stored in a configuration file.

The pixel cell is described in subsection 4.2.2. The basic functionality of the analogue and digital parts is checked by dedicated hit injection circuits. For a working pixel, the number of responses should correspond to the number of injections, if the injected charge is above the threshold.

Most important for the operation are the settings for the amplifier stage and the discriminator, as they influence the measured signal. The specific setting of their parameters for all pixels, i.e. the procedure of adjusting the threshold value and the ToT response, is called *tuning*.

A short explanation of the most important configuration parameters for the operation of modules with FE-I4 read-out chips is given in Appendix A. More details and information about all configuration parameters can be found in [52]. A short overview of the general tuning procedure is given in Appendix B.

5.2.2 Determination of threshold and ToT response

The ideal discriminator response curve is a step function. However, the real discriminator response curve is smeared by electronic noise. It is described by the convolution of the step function with a Gaussian distribution, the so-called error function

$$\mathrm{erf}(x) = \frac{2}{\sqrt{\pi}} \int_0^x e^{-t^2} \mathrm{d}t \quad . \tag{5.1}$$

To determine the set threshold, test charges are injected multiple times and the discriminator output is counted. This is repeated with increased charge. An error function is fitted to the distribution of discriminator hits against the injected charge. The symmetry point of the error function, where the discriminator fires in half of the cases, defines the threshold value. The width of the distribution describes the electronic noise. This procedure of threshold determination is called *threshold scan*.

To determine the ToT response, a fixed test charge is injected multiple times. A mean value is formed from the responses. This procedure is called *ToT verify scan*.

5.3 Source measurements

5.3.1 Source setup

As described in section 2.4, charged particles are detected by their energy loss in the sensor material. Because they are easy to handle, β-sources are often used in laboratory measurements to mimic particles resulting from beam collisions. A very common source for β-particles is the strontium isotope with the longest half-life, Sr-90. Its decay chain via yttrium to the stable zirconium is given by

$$^{90}_{38}\mathrm{Sr} \xrightarrow[28.79\,\mathrm{a}]{} {}^{90}_{39}\mathrm{Y} + e^- + \bar{\nu}_e \tag{5.2}$$

$$^{90}_{39}\mathrm{Y} \xrightarrow[64.00\,\mathrm{h}]{} {}^{90}_{40}\mathrm{Zr} + e^- + \bar{\nu}_e \quad . \tag{5.3}$$

The decay energy of (5.2) is 546.0 keV with a mean electron momentum of 195.8 keV [60]. This equals an average of $\beta\gamma = 0.4$, with values up to $\beta\gamma = 1.1$. The decay energy of (5.3) is 2280.1 keV with a mean electron momentum of 933.6 keV [60]. This equals an average of $\beta\gamma = 1.8$, with values up to $\beta\gamma = 4.5$. Especially the electrons of the latter decay are close to the minimum of the stopping power, which is at $\beta\gamma = 2.4$ for electrons in silicon [61]. They are therefore suitable candidates for MIPs.

As γ-sources have discrete energies and therefore the expected deposited energy is known very precisely, they are often used in laboratory measurements as well. A very common γ-source is the americium isotope Am-241. Its decay to neptunium is given by

$$^{241}_{95}\mathrm{Am} \xrightarrow[432.6\,\mathrm{a}]{} {}^{237}_{93}\mathrm{Np} + {}^{4}_{2}\alpha + \gamma \tag{5.4}$$

where the photon has an energy of 59.5409 keV [62].

To perform the measurements, the source is placed above the sensor. If an emitted particle is detected within the sensor, the FE sends a hitbus signal. If the particle is not deflected or annihilated, it can be also detected in the trigger scintillator placed underneath the sensor, which will then send a signal as well.

Two different *source scan* modes are available in *STcontrol*. In *self-trigger* mode the internal hitbus signal is used to start the read-out. This method is error-prone because it is affected by defective pixels that indicate a hit even without a passing particle due to malfunction or radiation damage. In *external-trigger* mode, where the scintillator has to be connected to the *USBpix* system, the scintillator signal is used to start the read-out. This method reduces background hits caused by noise or scattered particles, but noise hits can still be in coincidence with triggered hits.

One output of a source scan in *STcontrol* is a raw data file with a stream of the FE output.

5.3.2 Analysis of raw data

To obtain detailed information about the hits in the sensor, the *fei4Analyzer* tool [63] is used. It reads and analyses the raw data file produced by *STcontrol*. The obtained data

record of each hit contains the column and the row, the ToT value and the LVL1 timing information, as well as the corresponding FE chip.

Clustering is then performed for the data set of each chip used. Hits in adjacent pixels and with matching time information are merged into hit clusters since the probability is high that they are caused by the same crossing particle. The cluster charge is obtained from the sum of the ToT values of all hits involved. The cluster position is obtained from the coordinates of its hit with the largest ToT value. From the clustered data hit maps, ToT and cluster size distributions are generated, for each chip, but also as a summary for the entire module.

The tool is able to process this for multiple input files and thus combine the data of several measurements. Also it is able to perform simple fits of a Landau-Gauss-convolutions to the ToT data, but this function is not used.

5.3.3 Fitting of ToT-data

As indicated in section 2.4, a Landau-Gauss convolution is used to describe the ToT distribution. Its MPV corresponds to the energy loss of MIP-like particles and is therefore the most stable and most important parameter for comparison in sensor investigation. It is determined by means of a regression analysis.

By definition, MIPs deposit the smallest amount of charge in the sensor. However, since significantly lower ToT values are also measured, it is plausible that these are caused by all kinds of electronic noise. To represent this non-suppressed background, a Gauss distribution is added to the fit function, whose mean is necessarily smaller than the Landau-Gauss MPV.

Two different algorithm are tested to fit the function, consisting of the sum of the Landau-Gauss convolution and the additional Gauss distribution, to the data. Although the further implementation differs significantly, both methods are derived from the algorithm of CERNLIB G110 *Landau Distribution* [64], which again is based on a numerical routine for calculating the Landau distribution [65].

The first method uses Python [66] only. It features a Landau-Gauss convolution provided by *pyLandau* [67]. To fit the function to the data, *curve_fit* from *scipy.optimize* [68] is used, which applies a non-linear method of least squares.

The second method embeds the ROOT framework [69] via PyROOT. A numerical convolution of ROOT's Landau and Gauss functions is performed to create the fit function. To fit this function to the data, the MIGRAD minimizer algorithm of MINUIT [70] is used, which applies a variable-metric method with inexact line search.

Both methods provide comparable results. The first method is more performant in terms of a faster runtime, fewer function calls and, in particular, less memory usage. The second method provides better results in terms of lower χ^2/dof values and is therefore used.

5.4 Testbeam measurements

5.4.1 Testbeam facilities

The most important facility for test beam measurements with ATLAS pixel modules is located in the SPS North Area, as described in detail in subsection 3.1.4. It features a pion beam of typically 120 GeV.

Another frequently used facility is located at the electron-synchrotron DESY II. It provides an electron or positron beam of up to 6 GeV.

5.4.2 EUDET-type telescopes

Since 2009, a series of beam telescopes have been developed to provide high tracking resolution for detector development in high energy physics testbeam environments. Since the first one was built within the EUDET project [71], they are called EUDET-type telescopes.

A photo of such a telescope is shown in Figure 5.3. For particle tracking, so-called MIMOSA26 (**m**inimum **i**onizing **MOS** **a**ctive pixel sensor) planes are used. These are **m**onolithic **a**ctive **p**ixel **s**ensors (MAPS), produced by means of the AMS 350 nm CMOS process. Each sensor features 663 552 pixel cells of size $18.4 \times 18.4\,\mu m^2$, arranged in 1152 columns and 576 rows. Its external dimensions are $21.5 \times 13.8\,mm^2$, its thickness

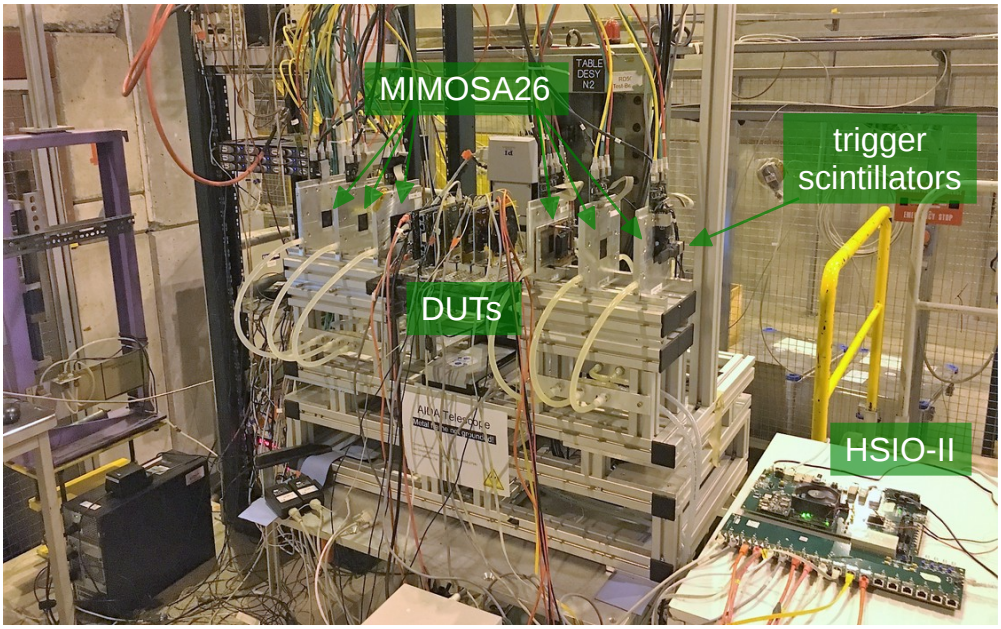

Figure 5.3: The AIDA telescope at CERN-SPS testbeam area H6B, loaded with six DUTs. On the table on the right is the HSIO-II which is used for DUT read-out.

is 50 µm. The binary hit information of the sensors is read out row by row using a rolling-shutter, leading to a full integration time of 112.5 µs per frame [72].

Each EUDET-type telescope consists of two arms, one upstream and one downstream of the **d**evice **u**nder **t**ests (DUTs). Three aluminium frames are mounted on each arm. A MIMOSA26 sensor is embedded in each frame which is water cooled to a stable operating temperature of 18 °C.

Two scintillators with photomultiplier tubes are mounted on each end of the telescope. They are connected to a coincidence circuit in the **t**rigger **l**ogic **u**nit (TLU). A passing beam particle will lead to coincidence. Then the TLU adds a time stamp and distributes the trigger signal to the **d**ata **ac**q**u**isition (DAQ) systems of the telescope and the DUTs. It also handles the busy signals, vetoing subsequent triggers as long as the DAQ systems are not ready.

The data acquisition framework EUDAQ [73] is used to merge all data streams. It provides the *Run Control* to which the TLU and the DAQ systems of telescope and DUTs are linked by so-called producers. All correlated data from the subsystems is merged into single events. A fixed number of events is combined into a run, which is stored on hard disk. EUDAQ also provides the *OnlineMonitor* tool to get a quick overview during data taking about hit maps and correlation plots of the recorded data. Immediate intervention is possible in the event of loss of synchronisation between the DAQ systems, noisy sensors, or other problems.

Examples for EUDET-type telescopes are ACONITE and AIDA at CERN-SPS testbeam areas H6A and H6B and DATURA at DESY testbeam area TB21. More details on EUDET-type telescopes can be found in [74, 75].

5.4.3 EUTelescope

Track reconstruction is performed with *EUTelescope* [76]. It is a modular software framework for generic pixel telescope data analysis. Its initial version was also developed within the EUDET project.

EUTelescope is embedded in the ILCsoft software collection, which is being developed within the **I**nternational **L**inear **C**ollider (ILC) community. It makes use of MARLIN (**M**odular **A**nalysis & **R**econstruction for the **Lin**ear collider) processors to convert any kind of testbeam input data into a standard format and finally, after various processing steps, reconstruct particle tracks.

The different processing steps and the required databases to move from raw testbeam data to final particle track data are shown in Figure 5.4. The five data processing steps are briefly introduced below. These processors are configured using steering files that are created individually from templates for each run. The required geometric information about all telescope planes and DUTs are stored in a GEAR (**Ge**ometry **A**PI for **R**econstruction) file. It contains the sensor ID, its position in a global coordinate system, its rotation, its size and the number and pitches of its pixels.

Detailed information about *EUTelescope* can be found on its website and in [75, 77, 78].

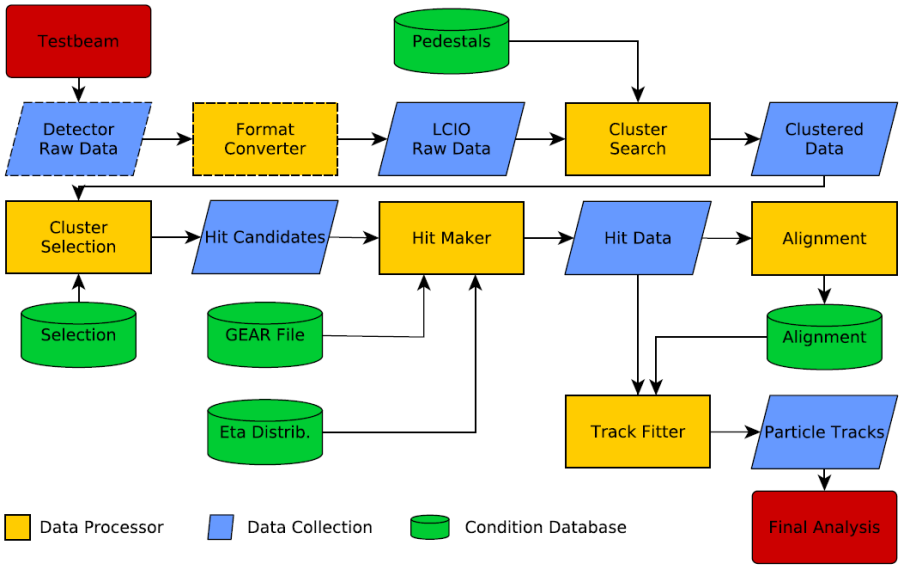

Figure 5.4: Testbeam data reconstruction scheme of EUTelescope. [75]

Converter As the first processing step the raw testbeam data is converted into the LCIO (**L**inear **C**ollider **I**nput/**O**utput) data format which is the standardized format used by *EUTelescope*. The conversion plug-in has to be provided by the user. In the case of ATLAS pixel devices it is included in EUDAQ.

During the converting step pixels are tagged hot/noisy if they fire more frequently than a given cut value, usually in the range of 0.001 to 0.005. A hot pixel database is created from the tagged pixels. This step is performed separately for telescope and DUT data. An example of a noisy pixel map is shown in Figure 5.5a, revealing 182 or 0.05 % noisy pixels in this plane.

Clustering The clustering processor comprises two steps, cluster search and cluster selection. The first merges hits in adjacent pixels into hit clusters since it is very likely that the hits are caused by the same passing particle. The latter uses the hot pixel database to identify and remove clusters containing at least one noisy pixel. An example of a cluster size distribution is shown in Figure 5.5b. It is dominated by one-hit clusters, but there is also a large fraction of two-hit clusters.

The cleaned collections are stored in a new LCIO file. Again, this step is performed separately for telescope and DUT data.

Hit Maker In this step the position of the clusters is determined. For devices with binary hit information such as the MIMOSA26 a simple geometric mean of all hits in the cluster is calculated, while for ATLAS pixel devices a charge-weighted center of gravity algorithm can be used because they provide this additional information. The

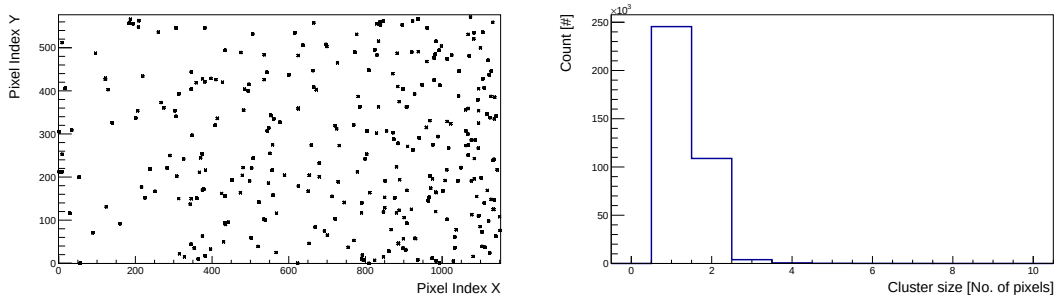

(a) Noisy pixel map of the first telescope plane. The marker size is largely increased.

(b) Cluster size in x of the first telescope plane.

Figure 5.5: Converter and Clustering example plots for noisy pixels and cluster sizes. Data taken at CERN-SPS, October 2016, run 575.

cluster coordinates are then transformed from local columns and rows to a global spatial position, with the origin at the center of the first MIMOSA26 plane. The geometric information as well as translation and rotation found in the GEAR file are used for this.

With the global hit information, correlation plots are filled for all planes. Since DUT orientation varies often, these can be used to check if the correct rotations were applied. The data is also used for a pre-alignment to get a good starting point for the further processors. Cuts are used in Correlator and PreAligner to remove uncorrelated hits from the collection. Then the difference in x- and y-positions of the planes in relation to the positions of the first plane for each event are histogrammed. The mean of this histogram is used to correct the plane position and to create new GEAR file.

Example plots for correlation and pre-alignment are shown in Figure 5.6, revealing the required positive correlation and a slight shift of about 1 mm.

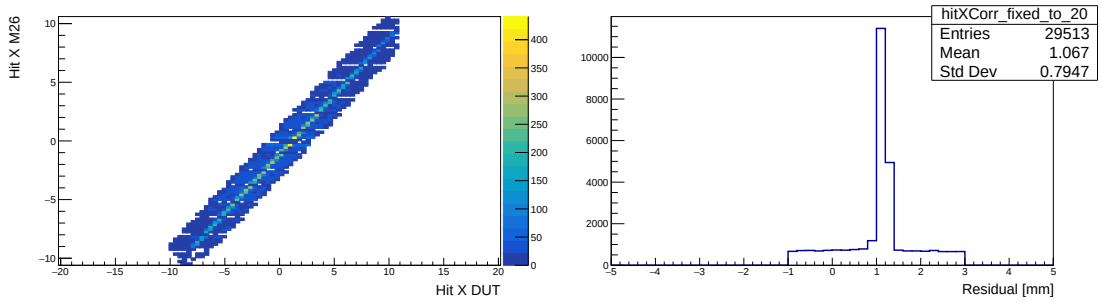

(a) Correlation plot in x between the first telescope plane and the first pixel module.

(b) Pre-alignment histogram of the first pixel module.

Figure 5.6: Hit Maker example plots for correlation and pre-alignment. Data taken at CERN-SPS, October 2016, run 575.

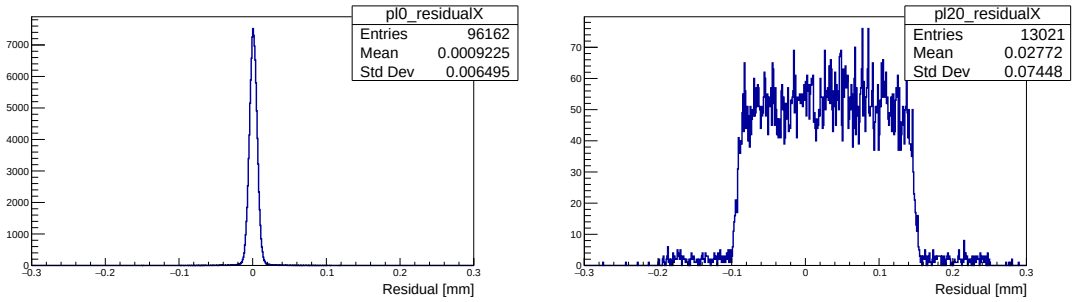

(a) Residual plot in x of the first telescope plane.

(b) Residual plot in x of the first pixel module.

Figure 5.7: Fitter example plots for residuals. Data taken at CERN-SPS, October 2016, run 575.

Alignment To align the final plane positions, tracks are fitted by means of a **d**eterministic **a**nnealing **f**ilter (DAF) fitter, which is a variation of a Kalman filter [79]. The pre-aligned hits are used for this, but the value of the expected intrinsic resolution of the planes is significantly increased to take misalignment into account. The final alignment values are obtained from the track residuals, using the *Millepede II* framework [80]. It will perform an overall least squares fit, including all local as well as global parameters to provide unbiased alignment corrections. Residual cuts are used to reduce combinatorial background.

This step creates the final aligned GEAR file.

Fitter The track fitting is repeated with the same fit processor as in the alignment step, but using full resolution and the latest GEAR file. The resulting tracks are saved in a so-called *tbtrack* files, which are then analyzed with *TBmonII*.

Example plots for the residuals after fitting are shown in Figure 5.7. The different pixel widths are clearly visible: 18 µm for the MIMOSA26 telescope plane, 250 µm for the ATLAS pixel module.

5.4.4 TBmon II

The *TBmonII* framework [81] is used for detailed analysis of the performance of ATLAS pixel modules in testbeams. Its analysis scheme is shown in Figure 5.8. Central part is the core processor, which executes the preprocessing and the analyses of the *EUTelescope* input data. Besides the *tbtrack* files, two configuration files are also required. The *mainConfig* contains general information such as data paths, which runs are to be processed and a list of all used DUTs. It also controls which analyses are performed. The settings for the analyses themselves, individual for each DUT, are in a separate configuration file, the *analysisConfig*. Also important are the DUT configs. They contain

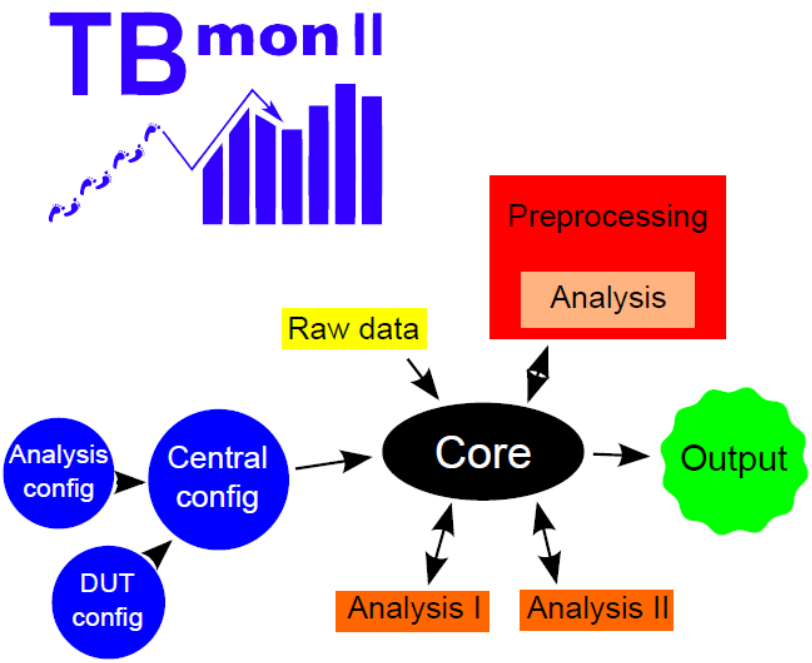

Figure 5.8: ATLAS pixel testbeam data analysis scheme of TBmonII. [78]

detailed information about pixel geometries and arrangement, again individual for each DUT.

The raw data is first preprocessed to ensure that only valid pixel module hits are taken into account. These are then used for a wide variety of analyses. The preprocessors used for this work are briefly introduced. More information about *TBmon*, the predecessor of *TBmonII*, are presented in [82]. The basic principles of the preprocessors and the analyses were transferred to *TBmonII*, but fundamental structural changes were made in the software, which significantly improved the usability and operability.

Preprocessors

EuBuildTrack Since the read-out time per frame of the MIMOSA26 telescope planes is more than two orders of magnitude longer that of the ATLAS pixel modules, most tracks contain only telescope hits. For this timing reason, the reference plane method is used. An unirradiated, well known and performing ATLAS pixel module is placed along the DUTs. Only tracks given by the telescope with matching hits in the reference plane are considered in the analyses.

EuBuildTrack checks all tracks if they have hits in the planes used for matching. It also flags the hits if they are in the edge region of the sensor. These are treated separately because they have different boundary conditions than the central pixels.

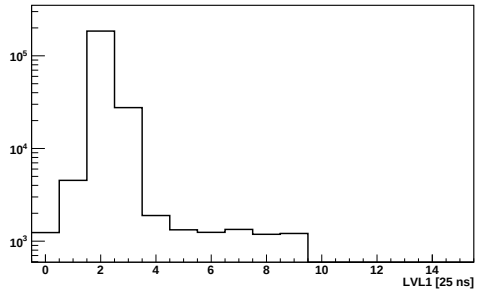

(a) LVL1 distribution of the reference pixel module (logarithmic scale). A cut will be applied between bins 1 and 3.

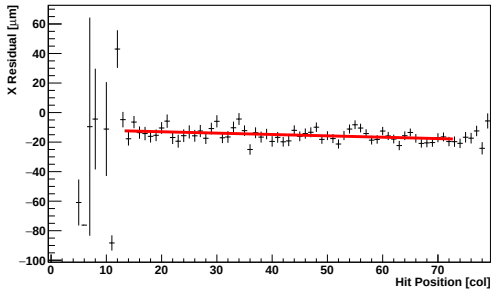

(b) Hit position in x vs. residual in x for the reference pixel module. The edge values have large errors due to low statistics.

Figure 5.9: Example plots for HotPixelFinder and CheckAlign. Data taken at CERN-SPS, October 2017, run 5583.

HotPixelFinder For all hits the same latency time is expected between LVL1 trigger and read-out. Hits that miss a window around the expected value are very likely caused by noise. These out-of-time hits are determined by cuts on the LVL1 distribution and discarded. An example of a LVL1 distribution is shown in Figure 5.9a, revealing about 10^3 noise hits in every LVL1 bin. After that, all pixels with an out-of-time hit are checked if they reach a certain fraction of all hits. Pixels to which this applies are flagged as hot. The *HotPixelFinder* also checks for empty pixels without any hits, either due to malfunction or due to low statistics. These empty or dead pixels are masked, along with the hot pixels and all pixels adjacent to hot pixels.

Additional user-selected pixels can be masked via a text file, using the *PixelMasker* preprocessor.

ClusterFinder & ClusterMatcher The *ClusterFinder* runs through all hits and collates neighbouring hits into clusters since it is assumed that those hits are caused by the same track. The cluster inherits the flag information like hot, dead or edge region from its hits.

The *ClusterMatcher* calculates a charge-weighted mean position of the clusters. If the distance between the cluster position and the track is smaller than an adjustable matching radius, the cluster and its flags are assigned to the track.

CheckAlign Investigated sensors may be slightly shifted or rotated. This is taken into account in *EUTelescope*, but not passed on in the *tbtrack* file. To correct this, *CheckAlign* calculates and histogramms the residuals from the difference between matched cluster and track position. If a dependence of the hit position on the device and the residual is detected, this is an indication of a rotation not yet considered. An example of such a plot for the x-direction is shown in Figure 5.9b, along with a first-order polynomial

fit. Its intercept indicates the displacement, while the slope indicates the rotation. This information is used to correct the position.

Main analyses

Efficiency All tracks and hits that pass the preprocessor checks are described as 'good' and used for the efficiency analyses. A track is considered good, if it has a matching hit in the reference plane. A hit is considered good if it is within the matching radius of a good track, if it belongs to a cluster that does not contain noisy or hot pixels, or if it is not masked otherwise. For an ideal detector, the number of hits n_{hits} and the number of tracks n_{tracks} are identical. Therefore, the efficiency ε is defined as

$$\varepsilon = \frac{n_{\text{hits}}}{n_{\text{tracks}}} \tag{5.5}$$

and its uncertainty σ_ε is defined as

$$\sigma_\varepsilon = \sqrt{\frac{\varepsilon \cdot (1-\varepsilon)}{n_{\text{tracks}}}} \quad . \tag{5.6}$$

The efficiency analysis calculates the global efficiency for the entire sensor area. For a more detailed view of the individual pixels, the hits and tracks from all pixels of the same geometry are mapped into one so-called in-pixel efficiency maps. This increases the statistics drastically under the assumption that all pixels of a geometry behave the same and allows precise statements within the scope of the spatial resolution.

EfficiencyVsGeometry This most in-depth analysis calculates the efficiency independently for every run and every pixel geometry. An example for the efficiency as a function of the run is shown in Figure 5.10. The uncertainty given by Equation 5.6 is

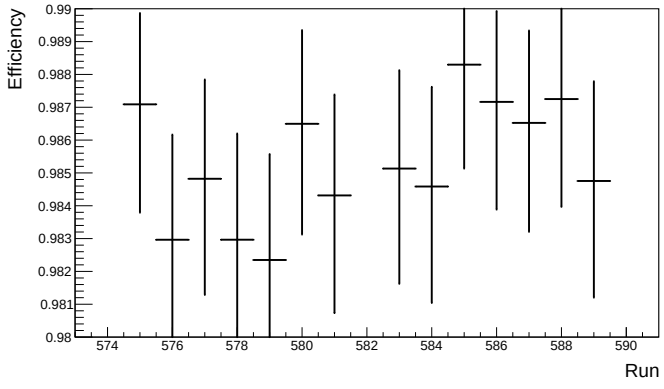

Figure 5.10: Example for the efficiency vs. run for geometry 0 for DUT 21. Excerpt of 15 runs from data taken at CERN-SPS, October 2016.

replaced by a Clopper-Pearson confidence interval [83] in this analysis, using a confidence level of $\gamma = 95\,\%$. The overall efficiency of the investigated module is estimated by an average of the individual efficiencies per run, weighted by the number of tracks. To take the fluctuations in the efficiency values into account, the overall confidence interval is calculated using the cumulative distribution function of the efficiency values. The interval limits are determined by the $\frac{1-\gamma}{2}$-quantile for the lower and by the $\frac{1+\gamma}{2}$-quantile for the upper limit.

5.5 Irradiation facilities

The NIEL hypothesis introduced in section 2.5 states that a fluence Φ_x can be normalised to the fluence of 1 MeV neutrons via

$$\Phi_{\mathrm{eq}} = \kappa \cdot \Phi_x \quad . \tag{5.7}$$

This turns the hardness factor κ to a key parameter of each irradiation facility.

5.5.1 Irradiation with protons

The irradiation with protons typically take place at accelerators. Due to the typical dimensions of particle beams these irradiations are often inhomogeneous. To compensate for this and to be able to irradiate devices larger than the FWHM, the beam is scanned across the device.

Examples are the 27 MeV cyclotron used in the Birmingham Irradiation Facility with a hardness factor of ≈ 2 [84, 85] and the 24 GeV CERN-PS at IRRAD, already described in detail in subsection 3.1.2. For IRRAD usually a hardness factor of 0.62 was used [86], but there are indications that after the refurbishment the factor is slightly lower [87], in the range of 0.56 to 0.60.

5.5.2 Irradiation with neutrons

The irradiation with neutrons typically take place in research reactors. These offer easy availability of reactor neutrons with typically a broad energy range up to a few MeV.

Examples for neutron irradiation facilities are the TRIGA reactor at IJS[1] with an effective hardness factor of 0.9 [88] and the **A**nnular **C**ore **R**esearch **R**eactor (ACRR) at Sandia[2].

[1] Institut "Jožef Stefan", Ljubljana, Slovenia
[2] Sandia National Laboratories, Albuquerque, USA

Chapter 6

Quad module investigation

The sensor properties of two quad modules are investigated in the laboratory and at testbeams. Their sensor layout and the PCB on which the modules were mounted has been described in section 4.4. The world's first investigated planar n^+-in-n quad module is named DO-Q01. Its PCB does not have the additional opening in its center. The HV is wirebonded to HV connector 2. The world's second investigated planar n^+-in-n quad module is named DO-Q02. Its PCB has the additional opening in its center. The HV is wirebonded to HV connector 1.

The identifiers for the sensors and the front-ends of both investigated quad modules are listed in Table 6.1. Their FEs are numbered clockwise, starting with FE1 at the bottom left of the sensor when viewed from the top, as shown in Figure 4.5.

Table 6.1: Quad module properties. All FEs are from the wafer A8PL4WH.

Module	Sensor	No. FE1	No. FE2	No. FE3	No. FE4
DO-Q01	330873-06-01	26	37	59	33
DO-Q02	330873-06-02	38	51	53	49

Parts of the results in subsection 6.1.2, subsection 6.4.2 and subsection 6.5.1 were published in [89]: A. Gisen et al. *Planar n-in-n quad module prototypes for the ATLAS ITk upgrade at HL-LHC*, JINST **12** (2017), C12032.

6.1 Leakage current

Current-voltage characteristics (IV curves) reveal important sensor properties and are also a main criterion for quality control. The technical specifications and acceptance criteria for planar pixel sensors to be used in the ATLAS ITk are defined in [90]. These acceptance criteria must be fulfilled by the sensors in order to be considered for the ITk. For unirradiated planar pixel sensors, the leakage current at 20 °C should be less than $0.75\,\mu A\,cm^{-2}$ at the operating voltage. The operating voltage equals the bias voltage at $V_{depl} + 50\,V$. The breakdown voltage is defined as the voltage at which the current rises by 20 % over a voltage step of 5 V. The breakdown voltage should be at least 20 V higher than the operating voltage.

The pixelated area of the investigated quad sensors is 13.736 cm^2. Thus, the leakage current requirement equals a maximum current of 10.3 µA for these sensors. The depletion voltage is 70 V, determined for the wafers by the manufacturer. This results in an operating voltage of 120 V. The slope s between two voltages of an IV characteristic is defined as

$$s(V_{\mathrm{min}},V_{\mathrm{max}}) = \frac{I(V_{\mathrm{max}}) - I(V_{\mathrm{min}})}{V_{\mathrm{max}} - V_{\mathrm{min}}} \quad . \tag{6.1}$$

A small slope is expected, as it is the behaviour of an ideal diode. An increase in the slope of more than 4 % is equivalent to the breakdown criteria.

For both quad modules, the current was measured up to a maximum voltage of 300 V at different temperatures in a climate chamber. The given temperature corresponds to the set temperature of the climate chamber. A small offset in sensor temperature caused by self-heating is expected but not taken into account. The humidity inside the climate chamber was controlled and kept low by its environmental control circuit, but it was not monitored.

6.1.1 DO-Q01

The leakage current characteristics of DO-Q01 are shown in Figure 6.1. No plateau is visible, the leakage current increases continuously, with an increase in the slope starting at approximately 210 V and finally resulting in a temperature-independent breakdown at 300 V. The values for currents and slopes at different bias voltages and different

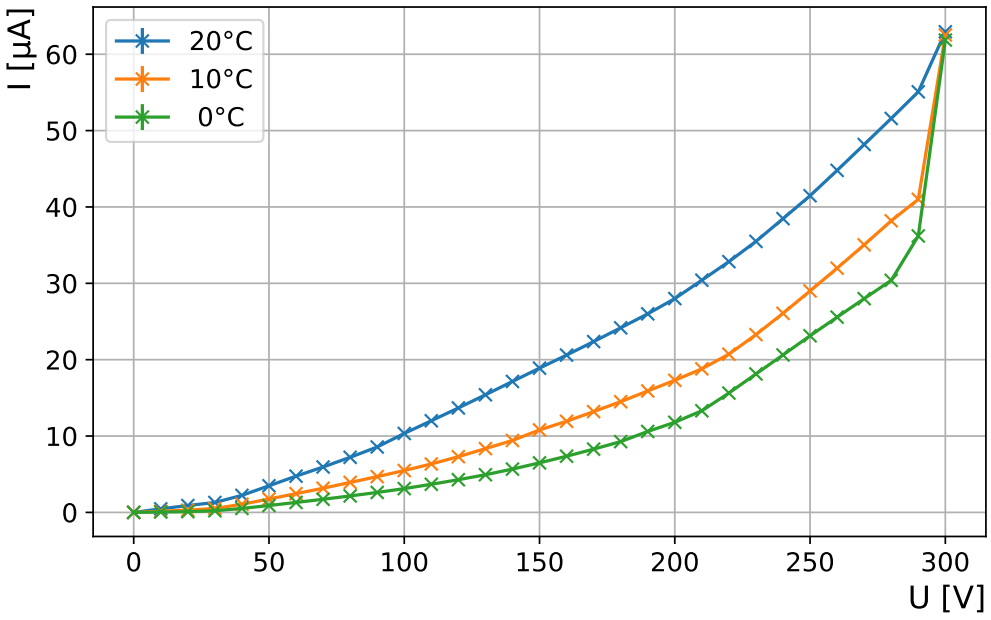

Figure 6.1: IV characteristics for DO-Q01 at different temperatures.

Table 6.2: Currents and slopes at different bias voltages and different temperatures for DO-Q01.

Temperature	20 °C	10 °C	0 °C
Current at 120 V	17.5 µA	11.9 µA	8.75 µA
Slope s(100 V,210 V)	302 nA V^{-1}	129 nA V^{-1}	116 nA V^{-1}
Current at 210 V	44.6 µA	23.6 µA	19.2 µA
Slope s(210 V,280 V)	423 nA V^{-1}	292 nA V^{-1}	277 nA V^{-1}

temperatures are shown in Table 6.2. An adjustment according to Equation 2.6 of the currents at 120 V results in an expected temperature difference of 3.1 °C between the currents measured at 0 °C and 10 °C and in an expected temperature difference of 4.1 °C between the currents measured at 10 °C and 20 °C. This indicates that only a small part of the measured current is generated in the bulk, since the temperature dependency of the bulk current, given by Equation 2.5, is violated. A current of 2.46 µA at 120 V was measured on the undiced sensor on its wafer which is less than 15 % of the value measured for the module. The increased current is therefore a consequence of damage to the surface during dicing or bump-bonding. It may also be an indication of a damage in the front-ends, as their pixel cells provide grounding for modules.

6.1.2 DO-Q02

The leakage current characteristics of DO-Q02 are shown in Figure 6.2. The plateau starts at 100 V, where a current of 2.12 µA is measured. At the operating voltage, a current of 2.17 µA is measured, which is far below the requested 10.3 µA. The slope between 120 V and 300 V is determined to 1.87 nA V^{-1}. No breakdown occurs up to the maximum measured voltage. Thus, the acceptance criteria are fully met for DO-Q02.

The values of the currents at the operating voltage and the slopes in the range of 120 V to 300 V for different temperatures are shown in Table 6.3. The temperature dependence is given by Equation 2.5 and thus the measured current is dominated by bulk current. A current of 2.27 µA at 120 V was measured on the undiced sensor on its wafer, which matches the current measured for the module.

Table 6.3: Currents and slopes for different temperatures for DO-Q02.

Temperature	20 °C	10 °C	0 °C
Current at 120 V	2.17 µA	0.747 µA	0.233 µA
Slope s(120 V,300 V)	1.87 nA V^{-1}	0.883 nA V^{-1}	0.520 nA V^{-1}

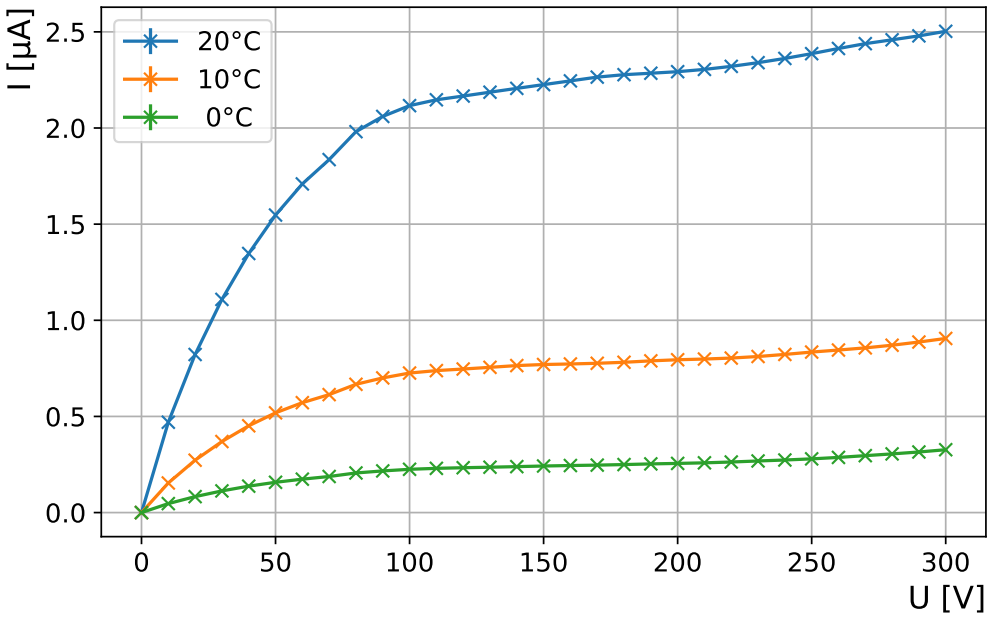

Figure 6.2: IV characteristics for DO-Q02 at different temperatures.

6.2 Tuning of quad modules

The module under test was placed in an insulated box which includes a metal heat exchanger connected to a regulated chiller. The box was flushed with pre-cooled dried air to improve the cooling performance and to keep the humidity low and preclude condensation. Configuration and read-out were performed using a *USBpix* BIC setup and *STcontrol*. Information about the configuration parameter and the tuning methodology can be found in section 5.2.

A bias voltage of 150 V was applied to the sensor. The voltage regulators were supplied with 2 V, resulting in a total current consumption of 1.3 A after configuration in case of DO-Q01 and 1.5 A in case of DO-Q02. The power dissipation of multiple FEs in operation had a notable influence on the sensor temperature, thus the device had to be cooled. Therefore, the chiller was set to 10 °C. The temperature resistors mounted on the PCB were reading a temperature around 16 °C.

6.2.1 Basic functionality tests

The basic functionality is checked with a *digital* and an *analog test* at first. For both test scans a response of 200 hits per pixel is expected, corresponding to the number of injections. Deviations can indicate defective pixels.

DO-Q01

The results of the initial tests for DO-Q01 are show in Figure 6.3a and Figure 6.3b. One of the four chips, FE4, did not respond at all. A short circuit between the analogue power line (VDDA) and ground was measured on the corresponding pins of the PCB. It is assumed that the performed necessary re-dicing, described in section 4.4.1, did not work properly for this chip and the short circuit remained. It is therefore excluded in all further measurements. The defect chip explains the reduced current consumption of DO-Q01 with respect to DO-Q02.

For the other three FEs, each topmost row contains three groups of 8 non-responsive, or empty, pixels each. These groups are in the columns 23 to 30, 35 to 42 and 47 to 54. This is a known FE-I4 feature that results from the dicing of the top row pads, which is why these pixels are excluded from all following investigations.

The number of pixels revealed by the *analog test* with no hits at all or fewer or more hits than the expected 200 are shown in Table 6.4 for DO-Q01. For the reasons mentioned above, the number of empty pixels is reduced by 24 at every working FE. According to IBL criteria, the number of defective pixels in a module should be less than 1 % [38]. For FE2 and FE3, the number of defective pixels is very low and clearly within

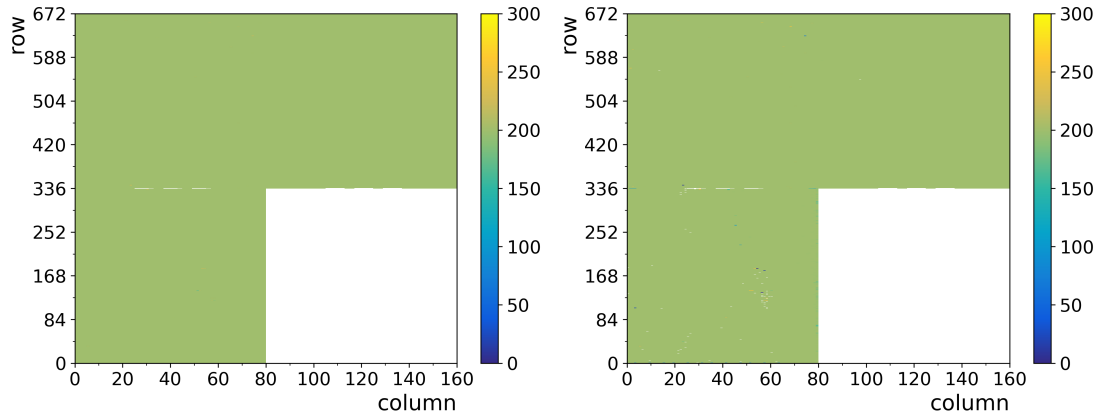

(a) Digital test. **(b)** Analog test.

Figure 6.3: Initial *digital* and *analog* tests of DO-Q01.

Table 6.4: Defective pixels revealed by the *analog test* for DO-Q01.

pixels	empty	hits < 200	hits > 200	total	percentage
FE1	64	114	13	191	0.71 %
FE2	1	2	19	22	0.08 %
FE3	3	1	–	4	0.02 %
FE4	26 880	–	–	26 880	100 %

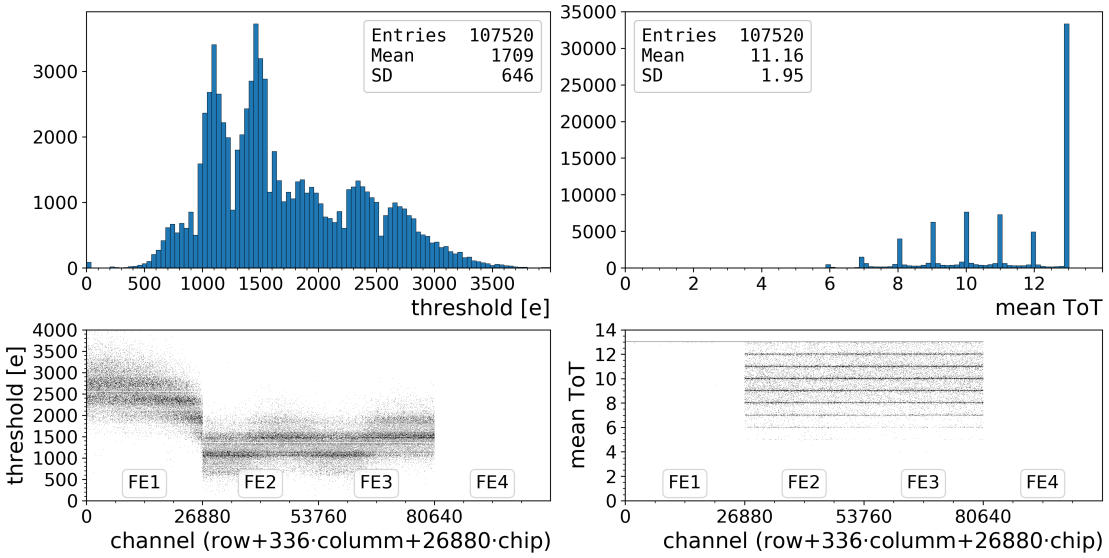

(a) *Threshold scan.* **(b)** *ToT verify scan.*

Figure 6.4: Initial *threshold* and *ToT verify scan* of DO-Q01.

this range. FE1 has a significantly higher share of problematic pixels but it is still less than 1 %.

After these initial tests, a *threshold scan* and a *tot verify scan* were performed, using standard configuration parameters. The threshold distribution is shown in Figure 6.4a. The distribution has a standard deviation of 646 e, which is very wide, but there are two peaks between 1000 e and 1600 e, to which both FE2 and FE3 contribute. With the same configuration, FE1 has a significantly higher threshold, it contributes to two peaks between 2200 e and 2900 e.

The ToT distribution is shown in Figure 6.4b. The responses of FE2 and FE3 are normally distributed without strong deviations between the two chips. The ToT response of all pixels of FE1 is 13, the maximum possible value, which therefore represents the overflow. This ToT signal corresponds to a long discharge time, resulting from a very low feedback current of the amplifiers. Changes in the configuration value controlling the DAC of the preamplifier did not affect the response. A failure of the preamplifier stages can be excluded, as the *analog test* provided a satisfactory result. The threshold of this FE can be tuned, which doesn't have much influence on the ToT answer as expected, but this shows that there is no general communication problem with the chip, as other values can be adjusted. This is a very rare behaviour that has never been seen before or thereafter in another module. It is assumed that this is an intrinsic FE malfunction that was either imperceptible by wafer probing or caused by the re-dicing. The first case is more probable, as in the latter case a total failure due to the short circuits would be more likely, as with FE4.

This first tests on DO-Q01 have shown that two FEs are working perfectly fine.

Another one has a very specific problem concerning its ToT response, which has not been investigated further. The last one fails electrically, very likely due to mistreatment in the preparation of the bump-bonding step. Since the cause was probably identified, a comparable failure should not occur in the future.

DO-Q02

The first tests on DO-Q02 revealed that all FE are operational, but a high occupancy was found in the edge pixels on column 160, as shown in Figure 6.5a. Although the effect did not occur always, further investigations revealed a dependence on the operating voltage. Near to the conspicuous area were wirebonds located, leading to a redundant HV pad. After pulling of all wirebonds leading to all unconnected, floating HV pads, the effect stopped occurring. The result of the *analog test* after this procedure is shown in Figure 6.5b.

The number of pixels revealed by the *analog test* with no hits at all or fewer or more hits than the expected 200 are shown in Table 6.5 for DO-Q02. The number of defective pixels in all FEs is very low and clearly within the expected range of less than 1 %, which indicates good bump bond quality. A *threshold* scan and a *ToT verify* scan, performed

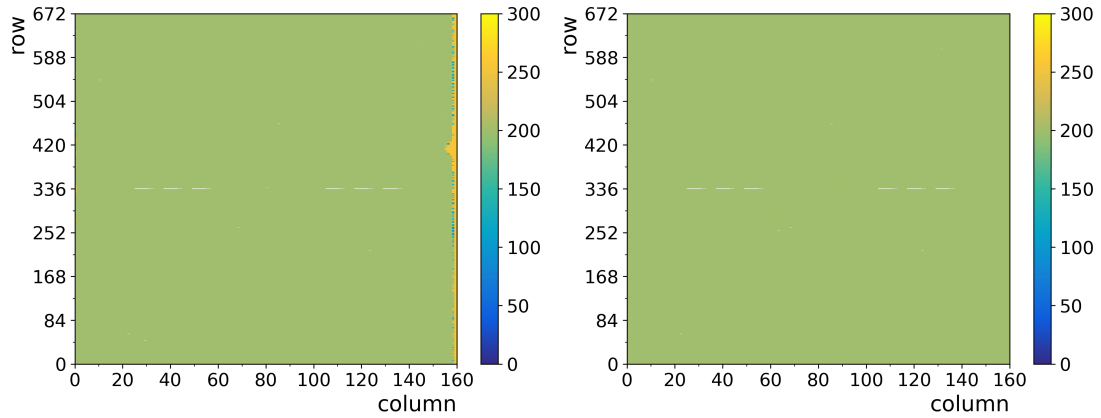

(a) *Analog test* before HV wirebond pulling. **(b)** *Analog test* after HV wirebond pulling.

Figure 6.5: Result of the initial *analog* tests.

Table 6.5: Defective pixels revealed by the *analog test* for DO-Q02.

pixels	empty	hits < 200	hits > 200	total	percentage
FE1	3	–	5	8	0.03 %
FE2	1	–	8	9	0.03 %
FE3	2	–	4	6	0.02 %
FE4	2	–	7	9	0.03 %

using standard configuration parameters, revealed no irregularities. All FEs showed a comparable performance. These first tests on DO-Q02 have shown that the module is operating as expected and even better than DO-Q01.

6.2.2 Tuning results

Main investigations for both quad modules were performed at a target tuning with a threshold of 3200 e and a ToT response of 6 at a reference charge of 20 ke. On DO-Q01 the two fully functional FEs were used while on DO-Q02 all four FEs were operated. The final tuning results for both quad modules are shown in Figure 6.6, Figure 6.7 and Figure 6.8. For DO-Q01 the configuration features a threshold of (3203 ± 69) e with a noise of (124 ± 14) e and a response of (6.00 ± 0.08) ToT at a reference charge of 20 ke. For DO-Q02 the configuration features a threshold of (3194 ± 76) e with a noise of (137 ± 17) e and a response of (6.00 ± 0.09) ToT at a reference charge of 20 ke.

There are no visible differences between the different pixel types in the threshold or the ToT distributions which is the expected outcome of the tuning algorithm. Deviations can only be observed in the noise distributions. For both quad modules, there is a cloud of significantly increased values over the majority of values and there is a group with slightly increased values at one edge of each chip. The latter can obviously be assigned to 'long' pixels, while the former probably stems from 'ganged' pixels, of which four can be found in each column. Due to the increased area of both special pixel types, an increased capacitance and thus an increased noise is expected. The results of a noise investigation per pixel type are shown in Table 6.6. The noise of DO-Q02 is

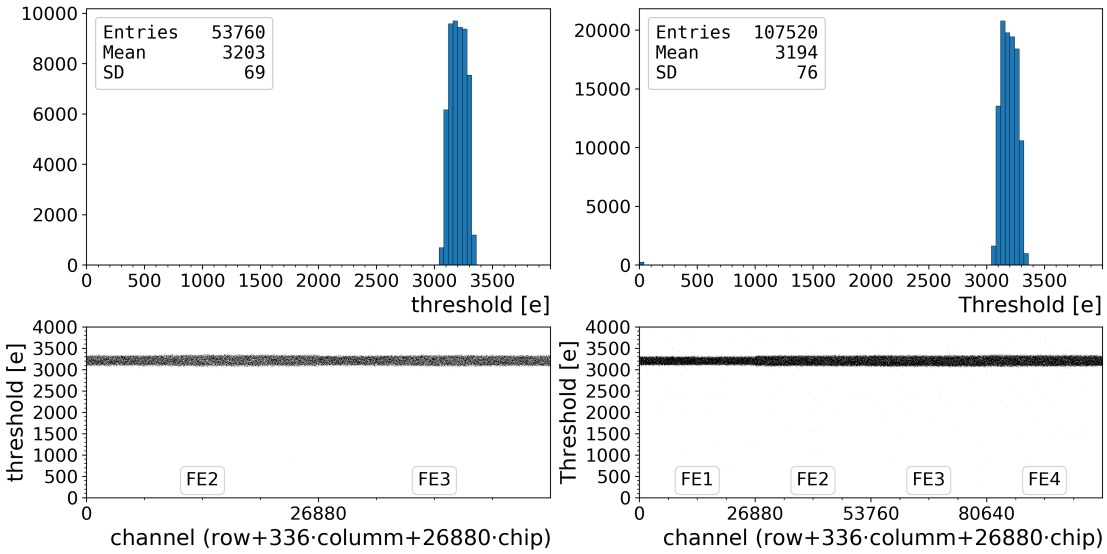

(a) *Threshold scan* of DO-Q01. **(b)** *Threshold scan* of DO-Q02.

Figure 6.6: Threshold distributions after tuning.

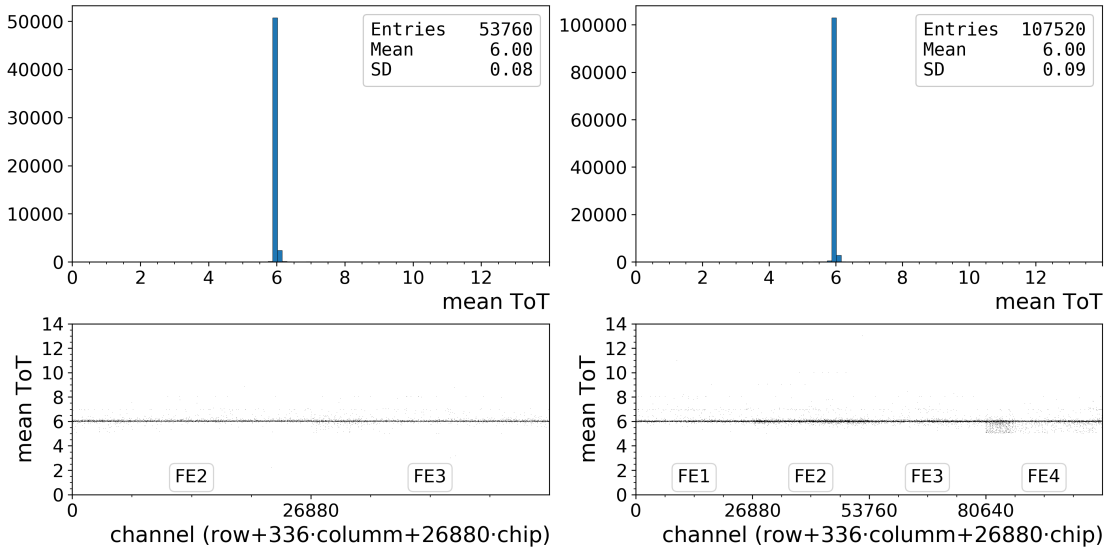

(a) *ToT verify scan* of DO-Q01. **(b)** *ToT verify scan* of DO-Q02.

Figure 6.7: ToT response distributions after tuning.

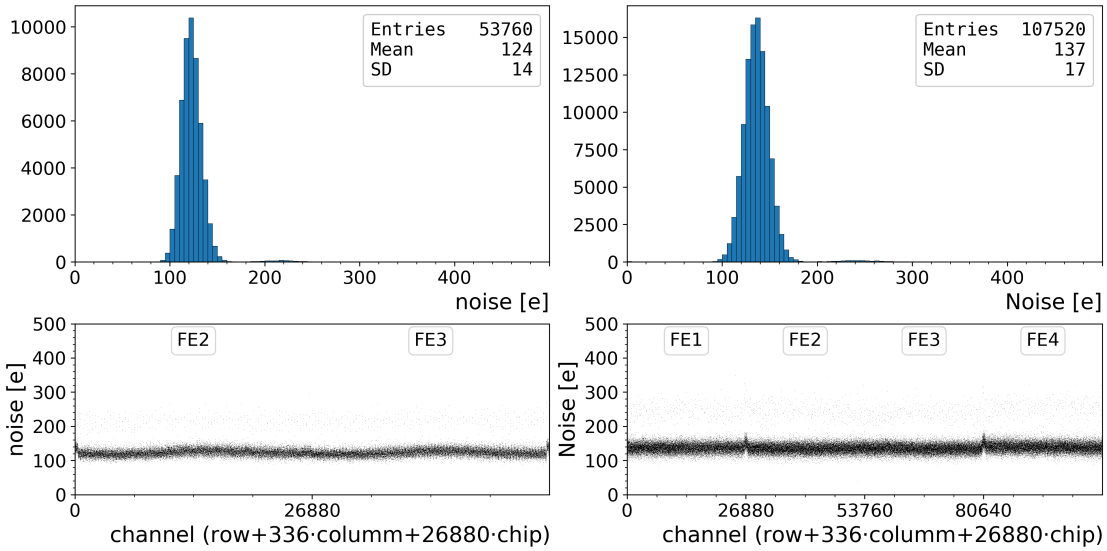

(a) *Noise scan* of DO-Q01. **(b)** *Noise scan* of DO-Q02.

Figure 6.8: Noise distributions after tuning.

Table 6.6: Mean threshold noise per pixel type at a threshold tuned to 3200 e.

pixel type	'standard'	'ganged'	'inter-ganged'	'long'
DO-Q01	(122 ± 10) e	(216 ± 18) e	(137 ± 11) e	(137 ± 9) e
DO-Q02	(137 ± 15) e	(246 ± 23) e	(149 ± 15) e	(136 ± 16) e

higher than the noise of DO-Q01, except for 'long' pixels. At both modules, all types of special pixels show increased noise compared to standard pixels. The difference between 'ganged' and 'long' pixels indicates a strong influence of the metal traces rather then the implantation area which is roughly the same for both types. The mean noise of the 'inter-ganged' pixels is on the level of the 'long' pixels, an indication that they are influenced by their neighbouring 'ganged' pixels. Because of their small number, 'long-ganged' and 'long-inter-ganged' pixels were excluded from this investigation.

6.2.3 Threshold tunings

Starting from the final tuning, for both quad modules attempts were made to reach lower thresholds by lowering the value of the *Vthin_AltFine* parameter, followed by some fine tuning using the *TDAC* parameter of each pixel. The mean of the distribution of the different thresholds is plotted against the corresponding noise in Figure 6.9. The error bars represent the standard deviation of the respective distribution.

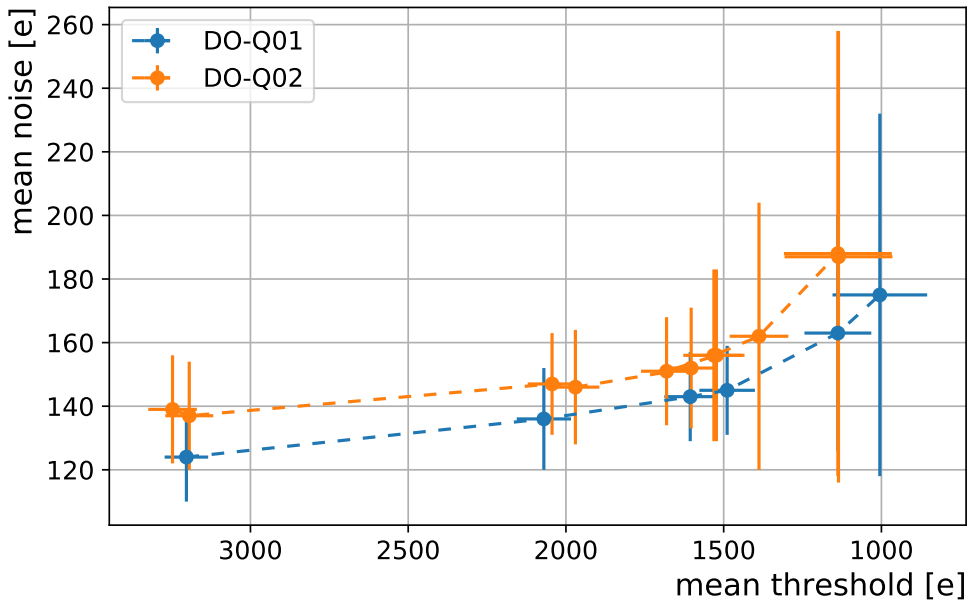

Figure 6.9: Mean threshold as a function of the mean noise for various scans of DO-Q01 and DO-Q02.

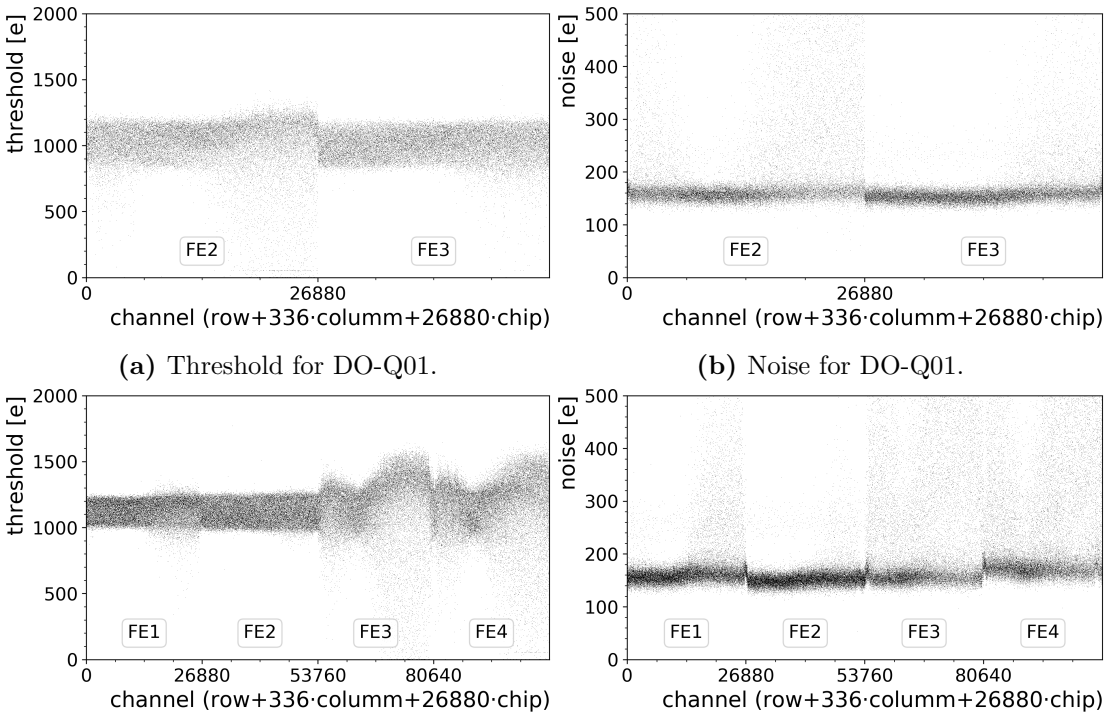

(a) Threshold for DO-Q01.

(b) Noise for DO-Q01.

(c) Threshold for DO-Q02.

(d) Noise for DO-Q02.

Figure 6.10: Threshold and noise at the lowest reachable thresholds of DO-Q01 and DO-Q02.

The lowest achievable threshold before failing for DO-Q01 is about 1000 e, while it is about 1100 e with DO-Q02. As also observed in subsection 6.2.2, the noise of DO-Q02 is about 10 % higher than the noise of DO-Q01, but both distributions show the same trend. There is a slight increase in noise and standard deviations for thresholds down to 1500 e. Afterwards, towards the lowest reachable thresholds around 1000 e, the dispersion largely increases. This spread prevents reaching lower thresholds.

The reasons for the dispersion are revealed in Figure 6.10, where the threshold and the noise distribution at the lowest reachable threshold of DO-Q01 and DO-Q02 are shown. A comparison of the threshold distribution with the noise distribution in Figure 6.11 shows the expected correlation between pixels with lower threshold values and pixels with higher noise values. However, there are significant differences between the FEs of a module. On the first chip of DO-Q01, the behaviour is very distinctive while on the second chip, this effect is less pronounced. Similar differences can be observed on DO-Q02. While the behaviour is very distinctive on the last two chips, the effect is less pronounced on the second chip. This makes a correlation of this feature with the position of the chip on the PCB unlikely. It is probably a feature of the used front-ends and the differences are therefore production-related.

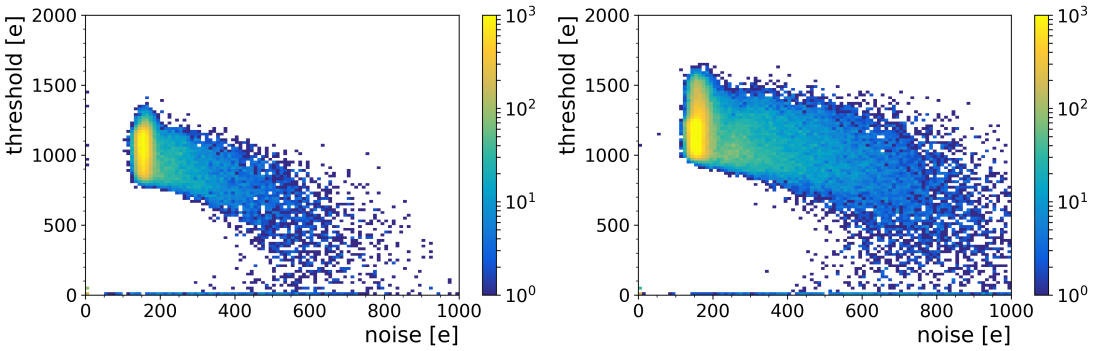

(a) Correlation for DO-Q01.

(b) Correlation for DO-Q02.

Figure 6.11: Correlation plot of threshold and noise at the lowest reachable thresholds of DO-Q01 and DO-Q02.

In conclusion, stable thresholds down to 1500 e could be achieved for both quad modules. However, lower thresholds come at the cost of higher noise. This prevents reaching even lower thresholds as it causes the *threshold scan* algorithm to fail.

6.3 Source measurements

The source measurements took place in the same isolation box setup as the tunings, described in section 6.2. The source setup, described in subsection 5.3.1, using a Sr-90 source and a trigger scintillator, was installed in this box. The trigger signal was routed to the USBpix system via a discriminator and a pulse shaper to suppress noise signals. The tunings presented in subsection 6.2.2, with a threshold of 3200 e and a ToT response of 6 at a reference charge of 20 ke, were used. The outside is shielded against the setup by 5 cm thick lead blocks.

The applied bias voltage was kept at 150 V for both modules. While testing DO-Q01, the LV current was now 0.8 A, since only two FE were in operation. The chiller was set to a temperature of 10 °C. During measurements a sensor leakage current of 17 µA to 20 µA was recorded. The on-board temperature resistors read a temperature of around 16 °C. While testing DO-Q02, the LV current remained at 1.5 A. The chiller was therefore set to a cooling temperature of 5 °C. During measurements a sensor leakage current of 5 µA to 6 µA was recorded, which indicates a sensor temperature around 25 °C when compared to the values in subsection 6.1.2.

6.3.1 Source scan hitmaps

DO-Q01

For DO-Q01 two different vertical source positions were investigated. At both positions, the Sr-90 source is placed centrally above FE2 and the measurements were performed

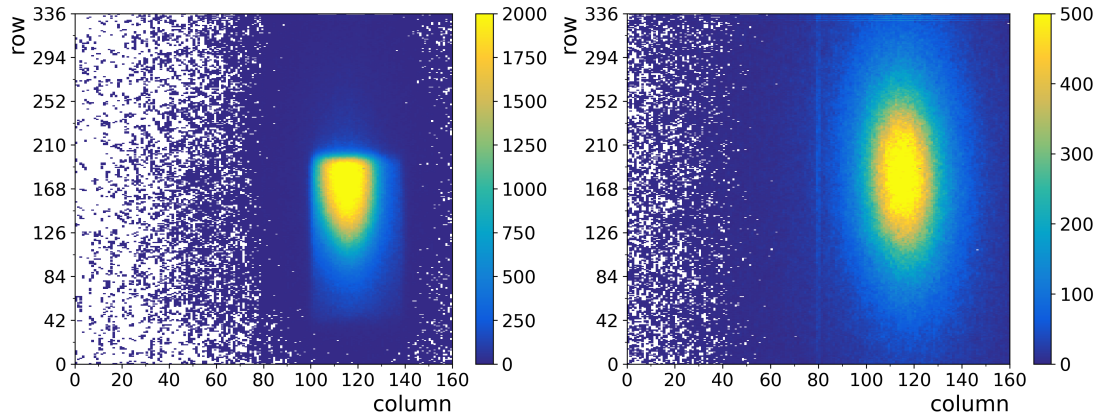

(a) Externally triggered hitmap. **(b)** Self-triggered hitmap.

Figure 6.12: External triggered and self-triggered hitmaps for DO-Q01 at positions A.

once with an external scintillator trigger and once with the FE internal self-trigger. At the first position, position A, the distance from the sensor to the source mount was about 2 cm. At the second position, position B, the distance from the sensor to the source mount was increased to roughly 3 cm.

The hitmaps for external triggered and self-triggered source measurements for DO-Q01 at position A are shown in Figure 6.12. The hitmaps of the source scans taken at position B looks similar. The material distribution of the PCB can only be seen in the hitmap taken with external triggering. Only in this trigger mode, the particles have to pass through the PCB before they can trigger a hit. The additional material increases the probability of interaction of the electrons and thus decreases the trigger rate. For the same reason, the hitmap taken with self-triggering shows a symmetric, pronounced beam spot, as there is no additional material between source and sensor, where the trigger signal is initiated.

DO-Q02

For DO-Q02, nine different horizontal positions were investigated to cover different areas of the quad sensor. The vertical distance between source and module was comparable to position A of DO-Q01, with a distance of 2 cm from the sensor to the source mount. The positions were in a 3×3 grid with distances of 1 cm. All measurements were performed using the external scintillator trigger.

The superposition of all hitmaps of all nine source positions is shown in Figure 6.13. As for DO-Q01, the material distribution of the PCB can be seen in the hitmap. At the openings five areas with increased number of hits are clearly visible. The four further measurements are between those openings with a reduced number of hits. Also recognizable is the increased number of hits in ‘long’ and ‘ganged’ pixels due to their increased size.

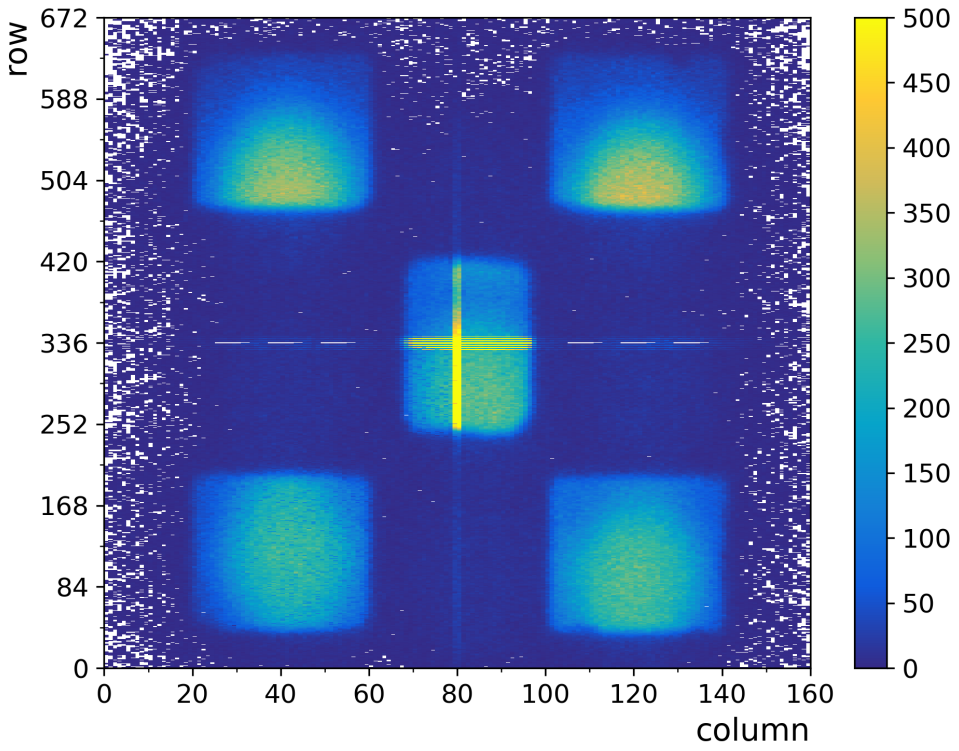

Figure 6.13: Superimposed hitmap for nine individual measurements at different positions for DO-Q02. The FEs are numbered clockwise, starting with FE1 at the bottom left.

6.3.2 Cluster size distribution

To increase the statistics, the different data sets, which are recorded with different numbers of maximum triggers and used to investigate the rate, are combined. Before the charge collection of this new data set is examined, its distribution of cluster sizes is inspected.

Electrons from the source impinge on the sensor at small angles with respect to the surface normal. To reach the trigger scintillator, these electrons must not be scattered at too large angles. For a vertical passage, only clusters with small sizes are expected, because thereby only one pixel is hit and the amount of charge sharing to neighbouring pixels is expected to be low. A frequently occurring effect is the division of ionized charge into two adjacent pixels, the so-called charge sharing, which can happen more easily on the long pixel side.

To generate clusters with large sizes, a particle must pass through the detector very obliquely. This happens either by scattering or by delta rays. These are high-energy electrons that have been knocked out of the nuclear orbit and are now able to ionize the medium as well.

DO-Q01

The cluster size fractions for the source scans performed with DO-Q01 are shown in Table 6.7. There are only minor differences between the two positions A and B, but there are major differences between the two trigger types 'external' and 'self'. This was expected, as while the external trigger filters the hits strongly by energy, all hits are accepted with the self-trigger, since they all trigger a hit signal. This is visualized for the results at position A in Figure 6.14. For both trigger methods, the most ToT values lie in the range of 1 ToT to 15 ToT. While for the external trigger the distribution decreases significantly at higher values, this is not the case for the self-trigger distribution. This is due to the large cluster sizes, which make a significant contribution to the ToT distribution. To be able to describe the entire distribution with a function as discussed in subsection 5.3.3, these contributions are summarized in a further, very broad Gaussian distribution. Their exact contribution is not relevant to the purpose of this study, the determination of the deposited charge of a MIP in the quad sensor.

The Americium measurement is completely different from the strontium measurements. Due to the nature of photons interaction with matter, there is no large cluster formation.

DO-Q02

Similar results as for DO-Q01 are observed for the cluster size distribution of DO-Q02. Since its measurements are only performed with Sr-90 and the external trigger, the majority of the measured clusters have a size of 1 or 2. The fraction of clusters with a size larger than 4 is less than 1.5 %.

6.3.3 Charge collection measurements using Sr-90

According to the Bethe equation, the mean energy loss for a MIP is $1.664\,\mathrm{MeV\,g^{-1}\,cm^2}$ in silicon [13], which equals $388\,\mathrm{eV\,\mu m^{-1}}$. However, as described in section 2.4, the MPV is the more important parameter for comparisons. A most probably energy loss Δ_p/x of $260\,\mathrm{eV\,\mu m^{-1}}$ was determined for MIP-like 500 MeV pions in a 320 µm thick silicon detector [13].

The sensors of the investigated quad modules have a thickness of 285 µm. Taking the mean energy required to create an electron-hole pair, 3.68 eV for β-particles [10], into account, this results in an expectation of a mean signal amplitude of 30 000 electrons and a most probable signal amplitude of 20 100 electrons.

Choice of starting values for the fit

To obtain the deposited charge in a sensor, a fit is performed on the ToT histogram as described in subsection 5.3.3. The selection of the starting values for the fit parameters are based on the investigated distribution.

The Landau-Gauss convolution requires 4 parameters. The starting value of its MPV is set to the center of the bin with the most entries. The starting values of the widths of

Table 6.7: Cluster size fractions for the source scans performed with DO-Q01. The last column summarizes all cluster sizes that are not displayed in detail.

Position	Cluster	CS1	CS2	CS3	CS4	CS5	CS> 5
A, ext. tr.	2 557 489	39.8 %	46.8 %	10.1 %	2.0 %	0.6 %	0.7 %
A, self-tr.	1 178 768	26.2 %	33.6 %	17.6 %	9.1 %	5.2 %	8.4 %
A, Am-241	1 865 404	83.4 %	16.6 %	0.0 %	0.0 %	0.0 %	0.0 %
B, ext. tr.	2 088 373	39.3 %	47.1 %	10.3 %	2.0 %	0.6 %	0.6 %
B, self-tr.	10 848 191	26.1 %	33.8 %	17.4 %	8.9 %	5.1 %	8.6 %

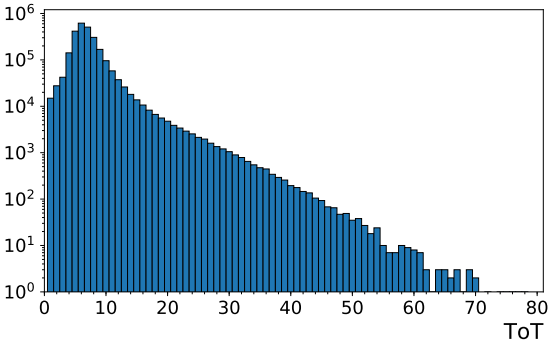

(a) Total ToT distribution for external triggering.

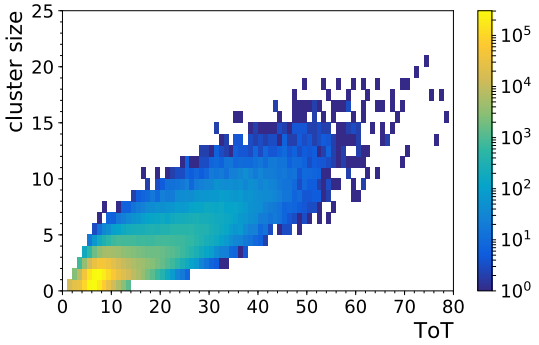

(b) ToT distribution as a function of the cluster size for external triggering.

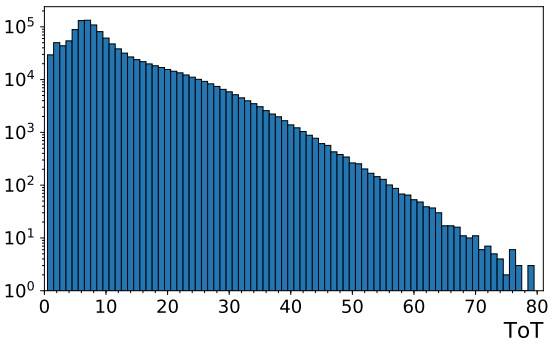

(c) Total ToT distribution for self-triggering.

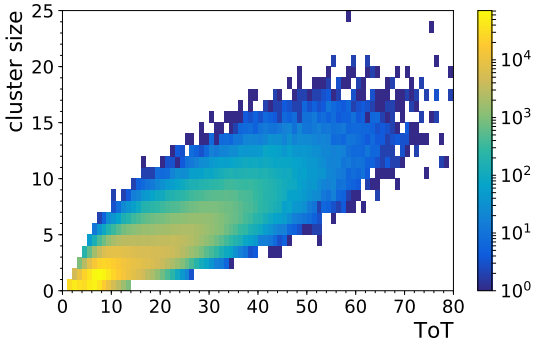

(d) ToT distribution as a function of the cluster size for self-triggering.

Figure 6.14: Total ToT distributions and ToT distributions per cluster size for DO-Q01 at position A.

Landau and Gauss are set to be 0.35, since it is expected that they are rather narrow. The starting value for the function's scaling parameter, which corresponds to its area, is guessed with 90 % of the distribution's integral.

The background Gauss distribution requires 3 parameter. The starting value of its mean is set to the center of the second bin as the entries well below the Landau-Gauss MPV are considered as noise. The starting value of its scaling parameter is set as height of this bin. The starting value of its width is set to 1.

If the additional background has to be taken into account, the starting value of its mean is expected to be far beyond the MPV, so it is set to bin 20. The starting value of the scaling parameter is accordingly set to the height of this bin. Since this is expected to be a wide distribution, the starting value of the width is set to 10.

No boundaries were set to any of these fit parameters.

DO-Q01

To obtain the charge deposited in DO-Q01, fits are performed on the ToT histograms of the combined data set recorded at source position A. To estimate the deviation in the case of repetition, measurements were carried out more than once for three measuring points. All ToT distributions of each group were fitted individually and a mean and its standard deviation was calculated from the MPV values. These results, along with the total variation range of the values and the relative deviation of the total range to the mean value, are shown in Table 6.8. These measurements show a statistical uncertainty below 1 %.

The interesting parts of the ToT distributions with the resulting fit functions for the entire data set are shown in Figure 6.15. For the source scan conducted with external triggering, the MPV obtained from the fitted Landau-Gauss convolution is (5.8670 ± 0.0014) ToT. The mean of the distribution is (7.1 ± 3.3) ToT. For the source scan conducted with self-triggering, the MPV is (6.1029 ± 0.0045) ToT. The mean of the distribution is (10.6 ± 7.9) ToT. Both MPVs are in good agreement with the expectation, since the module was tuned to a ToT response of 6 at a charge of 20.000 electrons. The self-trigger measurement shows a 4 % higher value than the externally triggered measurement. This value is well above the expected statistical fluctuation. The reasons for this can be found in the distribution of electron momenta. The first distribution does not take electrons with low momenta into account, which are absorbed before they reach the trigger scintillator. These low momentum electrons deposit large charges

Table 6.8: Deviation in MPV for repeated measurements.

Position	Trigger	mean MPV [ToT]	rel. deviation
A	$7 \times 50\,000$	5.864 ± 0.012	0.63 %
A	$5 \times 100\,000$	5.877 ± 0.018	0.76 %
A, s.t.	$6 \times 100\,000$	6.114 ± 0.015	0.76 %

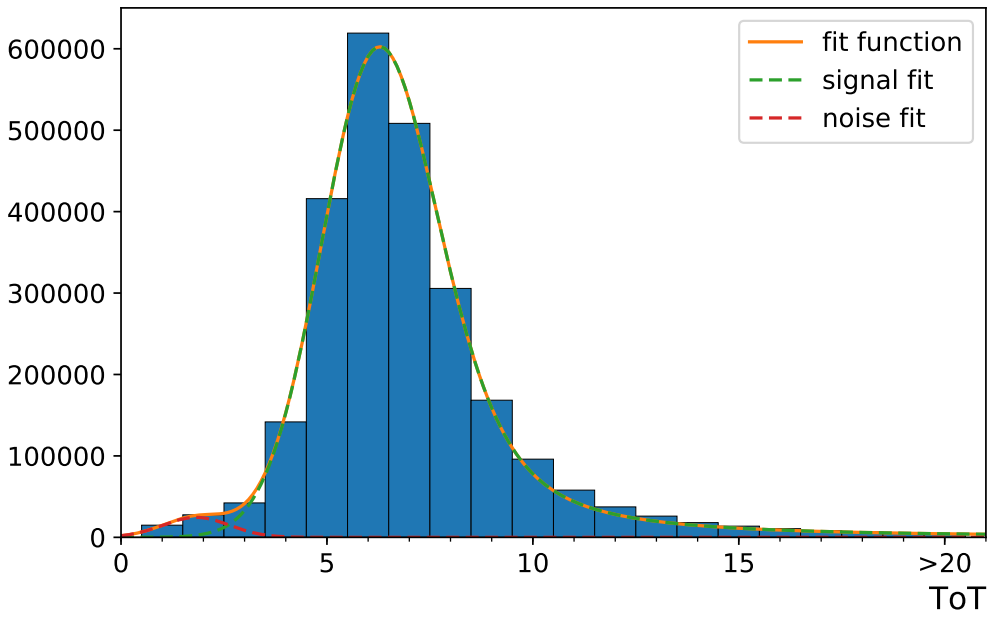

(a) ToT distribution for external triggering with fit function.

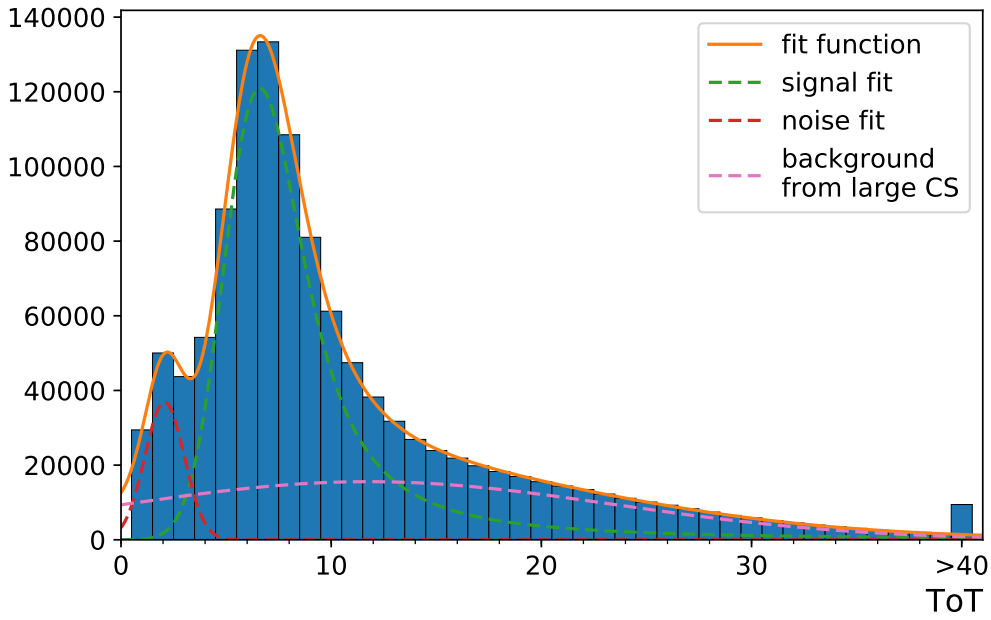

(b) ToT distribution for self-triggering with fit function.

Figure 6.15: ToT distributions with fit functions for source scans of DO-Q01 at position A. The last bin represents the overflow.

corresponding to high ToT values. This leads to the significant spread in the ToT distribution taken with external triggering.

DO-Q02

A comparable evaluation was performed with the ToT histograms of DO-Q02. Two data sets were created for this purpose. The first contains the four source positions centrally above the front ends and thus contains mainly hits in 'standard' pixels, the second contains the four source positions between the front ends and the source position in the middle of the module and thus contains an increased amount of hits in 'long' and 'ganged' pixels. Both data sets are also distinguishable by the amount of PCB material that the electrons have to pass, as the openings are located only under the FE and in the middle.

For the first data set, the MPV is (6.0376 ± 0.0016) ToT. For the second data set, the MPV is (6.1173 ± 0.0028) ToT, which is equivalent to an increase of the MPV of 1 % and in statistical fluctuation. Both values match the expected value of 6 ToT for the most probable energy loss, but a reduced charge was expected for the second data set, as the additional material reduces the amount of detected low-energy electrons. However, the hitmap shows many hits in the area of the openings in this data set as well. For this position, it is much more likely for a traversing particle to reach the trigger scintillator.

6.3.4 Charge collection measurements using Am-241

While not all defective bump-bond connections between pixel and front-end can be detected in the *analog test*, a source measurement allows a clear statement. To investigate bump-bond quality and because of their precisely known discrete energies, γ-sources are used for charge collection measurements.

The measurements were performed with DO-Q01 at position A, using an Am-241 source, as described in subsection 5.3.1. Since the α particles are stopped within the source's shielding, it only acts as a γ source. Due to the interactions of photons with matter, as described in section 2.4, only self-triggered source scans were possible. The photons have an energy of of 59.54 keV while the mean energy required to create an electron-hole pair is 3.66 eV for photons [10], so a signal of 16.2 ke is expected. The threshold was kept at 3200 e, but the module was retuned to a response of 8 ToT at a reference charge of 16 ke.

The hitmap for this source scan is shown in Figure 6.16a. In contrast to the used Sr-90 β-source, the Am-241 source irradiates the sensor homogeneously. Therefore the hits are uniformly distributed, only with a reduced number of hits on the left side. The source mount with a circular opening with a diameter of 20 mm was between source and sensor. This shape explains the reduction, the projected arc of the opening can be recognized. Also visible are the increased number of hits in the 'ganged' pixel at the top and the 'long' pixel between the FEs.

The measurement revealed 2 or 0.01 % empty pixel for FE2, which is 1 more pixel than

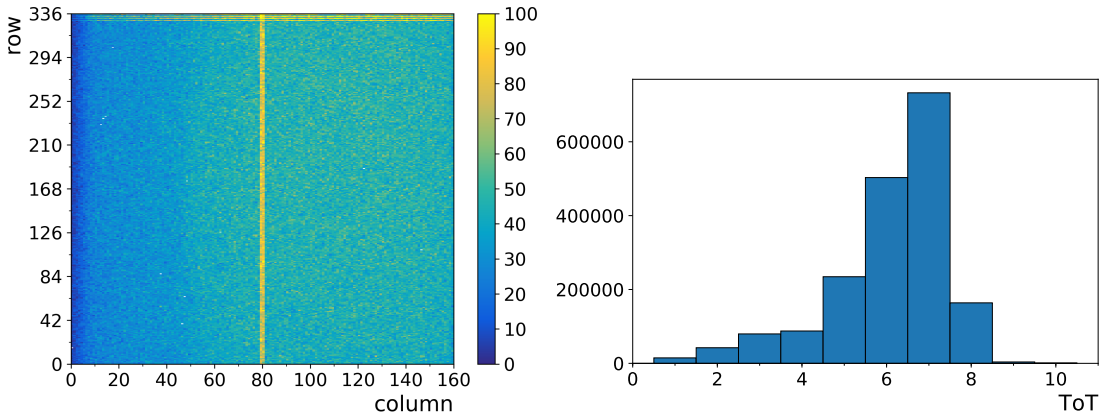

(a) Self-triggered hitmap. **(b)** ToT distribution.

Figure 6.16: Result of a source scan using Am-241 for DO-Q01.

the result of the *analog test* in section 6.2.1. It also revealed 10 or 0.04 % empty pixel for FE3, which are 7 more pixel than the result of the same *analog test*. The number of defective pixels is still very low and clearly within the acceptance limit of 1 %.

The ToT distribution is shown in Figure 6.16b. The entries at small ToT values result from backscattering and Compton scattering. Since the FE-I4 chip is not designed for precise charge measurements, no details are visible due to the low energy resolution. The spectrum is dominated by the photo peak. From the tuning, the photo peak position would be expected at 8 ToT, but most entries are at 7 ToT. This implies that the charge calibration circuit of the FEs is slightly miscalibrated, as the true values of the injection capacities may differ from the set values or, more likely, that not the entire induced charge is detected, since charges up to 3200 e, which are shared into adjacent pixels, are not detected as they are below the threshold value.

6.4 Testbeam measurements

For testbeam investigations, the quad sensor is divided into 55 sections, so-called geometries. For each of the FEs, there is one geometry describing the central 'standard' pixels. Seven additional geometries per FE describe the 'ganged' and 'inter-ganged' pixels. There is a geometry for the 'long' pixels between FE1 and FE4 and another for the 'long' pixels between FE2 and FE3. For the 'edge' pixels, the opposite edges of two FEs are combined into one geometry. This method reduces the number of required geometry descriptions in half, but still allows conclusions to be drawn about the corresponding FE based on the beam position. It is geometrically impossible to illuminate both edges of a quad module simultaneously due to the limited size of the sensors used as reference and the beam spot of the test beam.

Testbeam measurements were performed with both quad modules at a testbeam at

CERN in October 2016, using the 120 GeV pion beam and the AIDA telescope in H6B. The front-ends of the DUTs and the reference plane were read out with the RCE system. Details about the test beam setup and the read-out system can be found in chapter 5. During all measurements a bias voltage of 150 V was applied. The modules were tuned to a threshold of 3200 e and a ToT response of 6 at a reference charge of 20 ke. A fan provided air circulation in the setup, but no dedicated cooling was used.

The data was recorded in runs, containing roughly 16 k events each. Track reconstruction was performed with *EUTelescope* as described in subsection 5.4.3. As the number of events per geometry strongly depends on the beam position, the *EfficiencyVsGeometry* analysis of *TBmon2*, described in subsection 5.4.4, was used to calculate the efficiency and its uncertainty separately for each pixel geometry and each run. For each geometry, a mean efficiency weighted by the number of events was determined for all runs taken under the same conditions. The stated uncertainty represents the confidence interval of the cumulative distribution function of the individual efficiency values. It is calculated in a way that it comprises at least 95 % of the values above and below the mean value.

6.4.1 DO-Q01

It was possible to include DO-Q01 into the readout chain although only two of its FEs were operational. Due to desynchronization of the readout system components, only 5 % of the recorded data could be used, which led to low statistics. The resulting efficiencies are $99.86^{+0.14}_{-0.63}$ % and $99.89^{+0.11}_{-0.85}$ % for the 'standard' pixels of FE2 and FE3 with 50 500 and 43 500 tracks per pixel design, respectively. The efficiency for the 'long' pixels between those two FEs is $99.89^{+0.11}_{-0.83}$ % with 7000 tracks per pixel design.

Although the two working frond-ends of DO-Q01 showed good results in the test beam, the main investigations were carried out with DO-Q02, since all of its four front ends were functional. This is particularly important for measurements in the interchip area.

6.4.2 DO-Q02

With DO-Q02 three different positions on the sensor were examined. The first position, with the beam located centrally, focused on 'ganged' and 'inter-ganged' pixels and 'standard' pixels of all FEs. The second position, with the beam located on the edge of FE1 and FE2, focused on the 'edge' pixels located under the guard rings. The third position, with the beam located on the edge of FE1 and FE4, focused on the 'long' and the top 'edge' pixels, which are not shifted beneath the guard rings. A superimposed efficiency map of all three positions is shown in Figure 6.17. Because of the limitation to these positions and the different measurement times for these positions, not enough statistics are available for all 55 pixel designs on all front-ends.

Efficiencies of 'standard' pixels

With a share of 95 % of all read-out channels, the 'standard' pixels have the greatest influence on the functionality and overall tracking efficiency of a pixel module. The

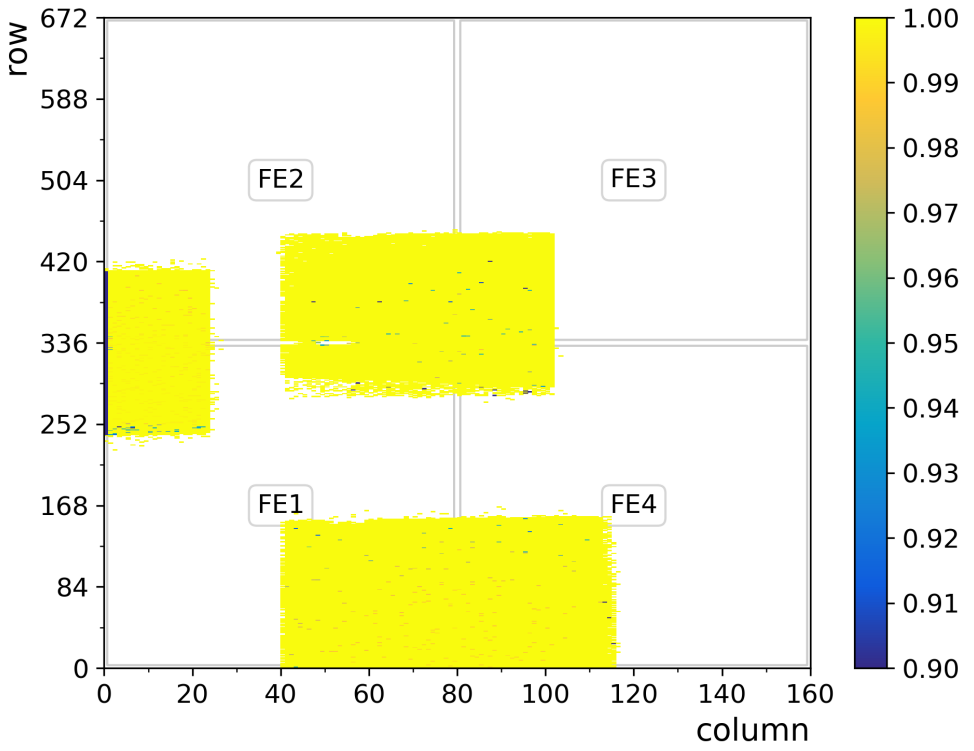

Figure 6.17: Efficiency map for measurements at three different beam positions for DO-Q02.

in-pixel efficiency maps for the 'standard' pixels of all FEs are shown in Figure 6.18. The visible differences can be explained solely by the different number of available tracks. The resulting efficiencies are $99.97^{+0.03}_{-0.09}$ % for FE1, $99.97^{+0.03}_{-0.18}$ % for FE2, $99.96^{+0.04}_{-0.09}$ % for FE3 and $99.97^{+0.03}_{-0.10}$ % for FE4. This shows an excellent tracking efficiency for the 'standard' pixels, and the uncertainties indicates a low fluctuation of the efficiency per run.

Efficiencies of 'ganged' and 'long' pixels

Each FE features four 'ganged' pixel types with different intermediate distances, caused by their 'inter-ganged' pixels, as shown in Figure 4.4. Examples for the in-pixel efficiency maps of these different 'ganged' pixel types are shown in Figure 6.19. They are overlayed with the layout of the two pixels connected via a metal trace at a distance of 300 µm, 250 µm, 200 µm and 150 µm, respectively. For simplicity reasons, the layout of the pixels between them is not drawn. The bump bond connection to the read-out chip is located at the bottom left for the pixels of FE1. The bias grid with its bias dot connections to each pixel is located at the right.

All investigated 'ganged' and 'inter-ganged' pixels show an excellent tracking efficiency,

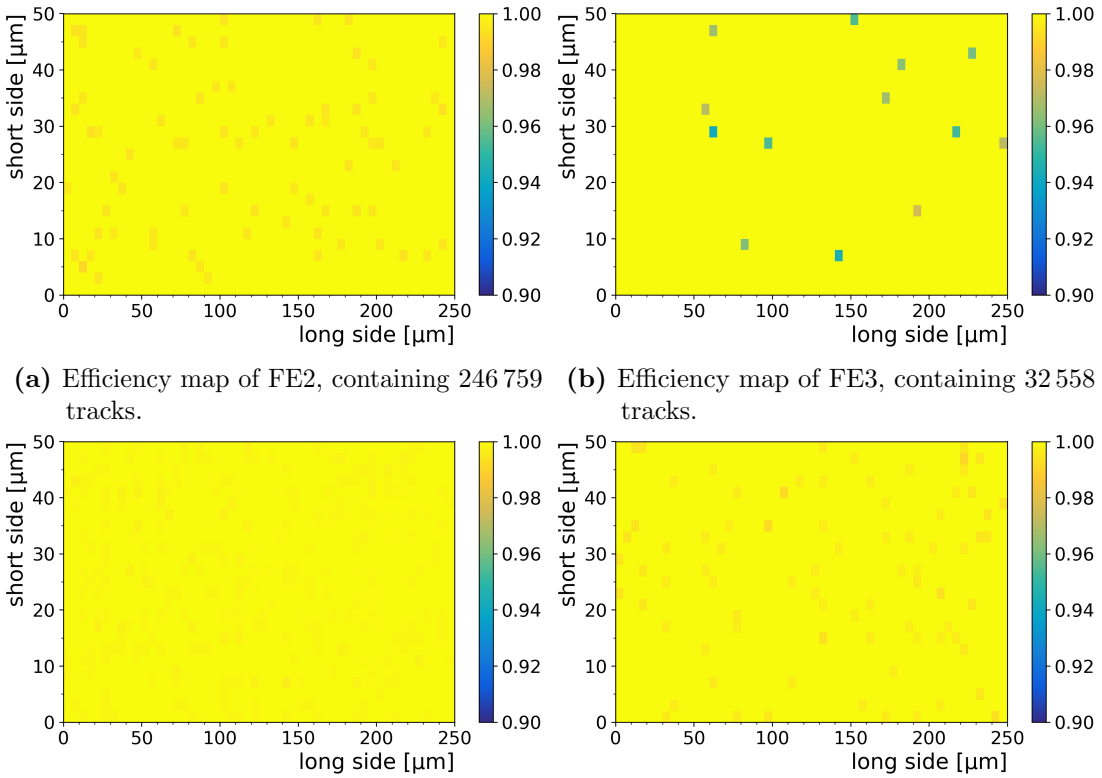

(a) Efficiency map of FE2, containing 246 759 tracks.

(b) Efficiency map of FE3, containing 32 558 tracks.

(c) Efficiency map of FE1, containing 1 047 460 tracks.

(d) Efficiency map of FE4, containing 333 468 tracks.

Figure 6.18: In-pixel efficiency maps for the 'standard' pixels of DO-Q01.

but it is noticeable that there is a slightly reduced efficiency in the area of the bias dot of the connected pixel in Figure 6.19a and in Figure 6.19b. This also is the case for the geometries of the other FEs, which are not shown here. It is known [91, 92] that the bias dot leads to reduced charge collection and hit efficiency in its area, especially after irradiation. Since the effect does not occur with all 'ganged' pixel types, it is likely that it is increased by the longer metal traces. Even if no reduced efficiency can be found in the other areas of the connected pixel, large distances of more than 200 µm between both ganged pixels should be avoided in future layouts, e.g. by omitting the 'inter-ganged' pixels, to avoid this efficiency loss. Each inter pixel increases the distance to be bridged by the metal trace by 50 µm. In the presented design the distance to be bridged is 150 µm for the innermost 'ganged' pixel and 300 µm for the outermost 'ganged' pixel due to 3 'inter-ganged' pixels.

The 'long' pixels also show excellent tracking efficiency close to 100 %, with no remarkable irregularities.

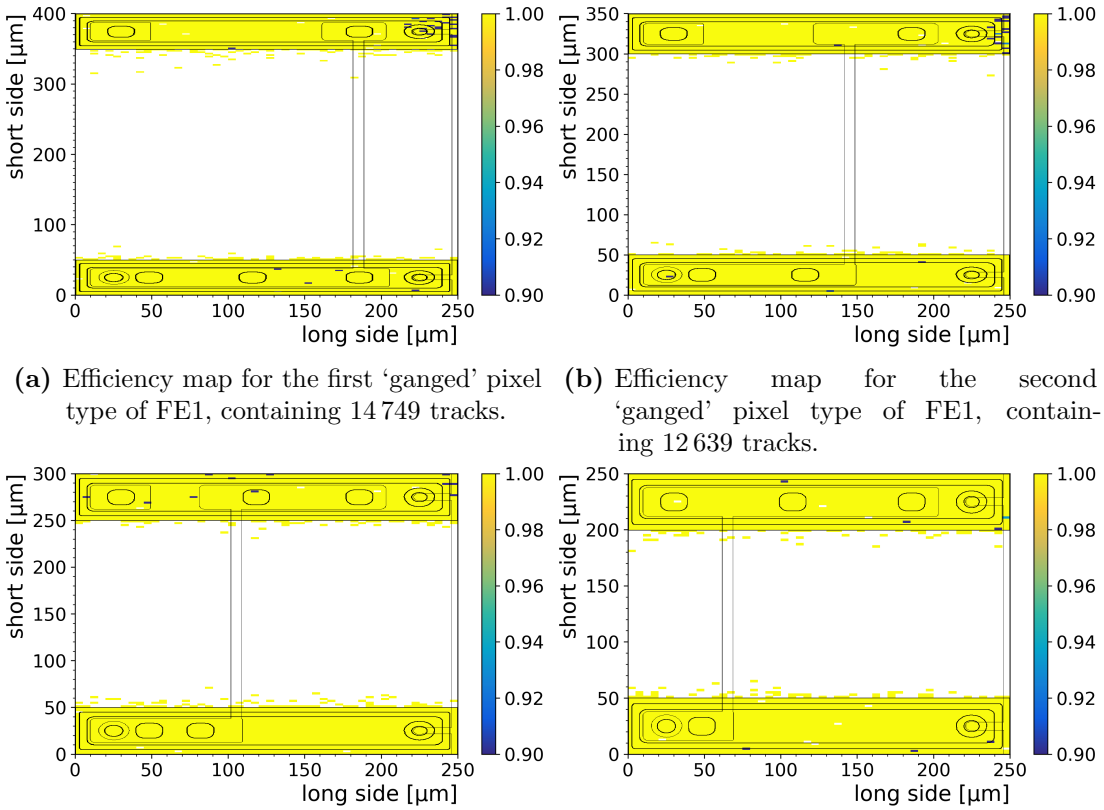

(a) Efficiency map for the first 'ganged' pixel type of FE1, containing 14 749 tracks.

(b) Efficiency map for the second 'ganged' pixel type of FE1, containing 12 639 tracks.

(c) Efficiency map for the third 'ganged' pixel type of FE1, containing 14 611 tracks.

(d) Efficiency map for the fourth 'ganged' pixel type of FE1, containing 13 337 tracks.

Figure 6.19: In-pixel efficiency maps for the four different 'ganged' pixel types of DO-Q01, overlayed with their layouts.

Efficiencies of 'edge' pixels

The first pixel column on the left side and the last pixel column on the right side are completely beneath the guard rings to enlarge the sensitive area and thus reduce the inactive area up to the cutting edge of the sensor. Since the bias voltage and thus the electric field is reduced by the guard rings, tracking efficiency is expected to be decreased for these pixels. To determine the effective active area, the measured in-pixel efficiency of these edge pixels is projected onto the long pixel side. To describe the progression of this projection, a parameterized Gaussian error function of the form

$$f_1(x) = \frac{\varepsilon}{2} \cdot \left[1 + \operatorname{erf}\left(\frac{x - x_0}{\sqrt{2}\sigma}\right)\right] \tag{6.2}$$

is used, where ε describes the plateau value of the distribution, x_0 is the shift parameter of the point of symmetry and σ is a dimension for the width. The plateau value ε can be

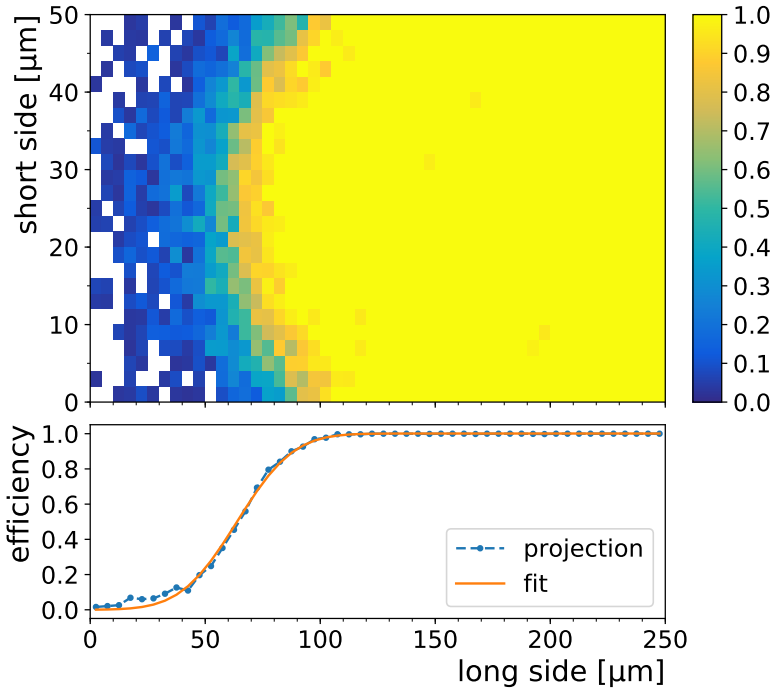

Figure 6.20: In-pixel efficiency map for the lateral edge pixels for FE1 of DO-Q02, along with a fitted projection of the efficiency to the long pixel side.

Table 6.9: Fit parameters for the function describing the efficiency of lateral edge pixels of DO-Q02.

	ε [%]	x_0 [µm]	σ [µm]
FE1	100.1 ± 0.3	63.8 ± 0.4	19.2 ± 0.5
FE2	100.0 ± 0.3	62.0 ± 0.3	22.0 ± 0.5

identified as maximum efficiency for this pixel design. The shift parameter x_0 describes the point at which the tracking efficiency reaches 50 % of its maximum value. It is used as benchmark. The in-pixel efficiency map for the lateral edge pixels of FE1 is shown in Figure 6.20, along with the projection onto the long pixel site. The fit was performed using the MIGRAD minimizer of MINUIT [70]. The fit results for the pixels of FE1 and FE2 are quite similar and are listed in Table 6.9. The plateau efficiencies are in agreement with 100 %. The point of symmetry is located at a distance of less than 65 µm from the pixel edge. This means that the sensor is efficient up to at least 185 µm beneath the guard rings. This is consistent with results of IBL pre-studies [47, 92], where 500 µm long pixels were partially shifted beneath the guard rings.

The first pixel row on the bottom and the last pixel row on the top are completely inside the guard rings, so their efficiency should not be affected by the reduced electric

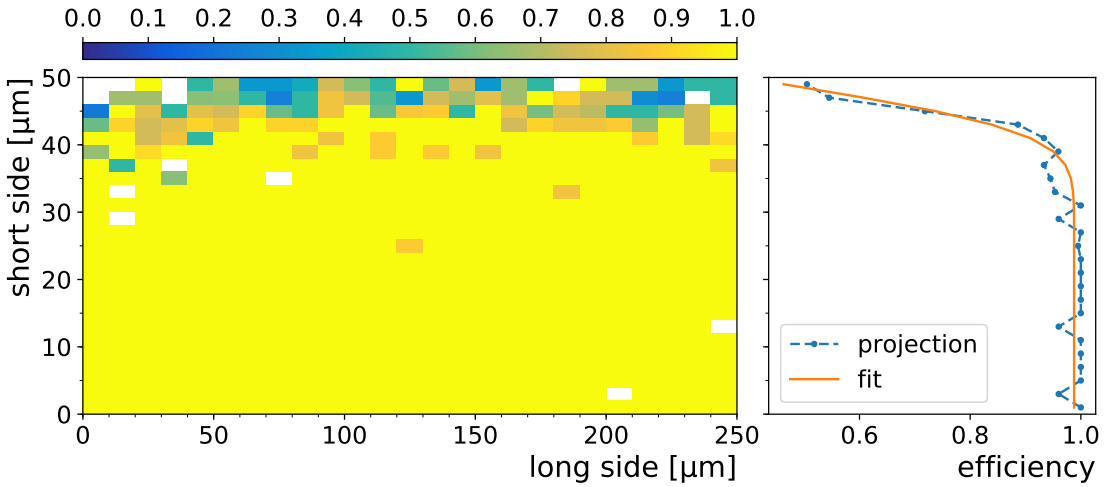

Figure 6.21: In-pixel efficiency map for the edge pixels at the bottom of FE1 of DO-Q02, along with a fitted projection of the efficiency to the short pixel side.

Table 6.10: Fit parameters for the function describing the efficiency of edge pixels at the bottom of DO-Q02.

	ε [%]	x_0 [µm]	σ [µm]
FE1	98.8 ± 0.7	48.6 ± 0.3	5.4 ± 0.5
FE4	98.6 ± 0.5	49.5 ± 0.3	5.8 ± 0.4

field. However, since they are located on the edge of the active surface, they cannot be resolved with unlimited resolution. To determine the spatial resolution, the measured in-pixel efficiency of these edge pixels is projected onto the short pixel side. The fit function has to be slightly modified to

$$f_2(x) = \frac{\varepsilon}{2} \cdot \left[1 - \mathrm{erf}\left(\frac{x - x_0}{\sqrt{2}\sigma}\right)\right] \tag{6.3}$$

to take the different origin into account. The nomenclature of the parameters does not change. The in-pixel efficiency map for the bottom edge pixels of FE1 is shown in Figure 6.21, along with the projection to the short pixel side. The fit results for the pixels of FE1 and FE4 are quite similar and are listed in Table 6.10, revealing a good efficiency in the plateau region. The point of symmetry is located close to the edge of the active area, as expected for a smeared resolved edge. The width of the function confirms the spatial resolution of the telescope of about 5 µm, otherwise determined from the residual distribution of the telescope tracks..

6.5 Irradiation

The use of quad modules is foreseen for the outer barrel layers and for the end-caps of the ITk. Radiation background simulations predict fluences of $2.8 \times 10^{15}\,\mathrm{n_{eq}\,cm^{-2}}$ to $3.8 \times 10^{15}\,\mathrm{n_{eq}\,cm^{-2}}$, including a safety factor of 1.5, after an integrated luminosity of $4000\,\mathrm{fb^{-1}}$ in this regions [8]. To test the behaviour of a module after receiving this end-of-life fluence, DO-Q02 was irradiated in the CERN-PS.

Starting in November 2016, the irradiation had to be interrupted due to the year-end technical stop of the accelerators. This interruption made it possible to examine the module at a fluence lower than the target fluence. The irradiation was continued in July 2017.

In the irradiation setup, the fluence received is estimated by putting aluminium foils close to the device-under-irradiation and measure their activation afterwards. For the first irradiation step, dosimetry information is available from 5 foils on the front and 5 foils on the back with a width of 2 cm each. For the second irradiation, dosimetry information is available only from 10 foils at the front, but with a width of 1 cm each.

The module was irradiated with its PCB, as modules are often damaged when attempting to remove them from its holders. Since other devices were also in the setup, the beam was scanned over the entire width of the PCB. The setup was cooled to $-25\,^{\circ}\mathrm{C}$ during the most of the irradiation.

The uncertainty of the initial fluence determination is stated to be 7 % [93]. To convert the fluence of the 24 GeV protons into a 1 MeV neutron equivalent fluence, a hardness factor $\kappa = 0.6$ is used. The converted dosimetry results of both irradiation steps are shown in Figure 6.22. The shape at the bottom marks the position of the quad module on the PCB. For the first step, the mean fluence for the quad module, obtained from the 3 central foils of front and back, is $(4.2 \pm 0.3) \times 10^{14}\,\mathrm{n_{eq}\,cm^{-2}}$. For the second step, the mean fluence for the quad module, obtained from the 4 central foils, is $(4.6 \pm 0.2) \times 10^{15}\,\mathrm{n_{eq}\,cm^{-2}}$. The total fluence, the sum of both irradiations, is $5 \times 10^{15}\,\mathrm{n_{eq}\,cm^{-2}}$.

The duration of the first irradiation was 1 week and the duration of the second irradiation was 11 weeks. This is consistent and results in an effectively achievable fluence of $4.2 \times 10^{14}\,\mathrm{n_{eq}\,cm^{-2}}$ per week for large devices such as quad modules.

6.5.1 Laboratory measurements

Due to the interruption of irradiation, laboratory investigations could be performed at a fluence of $4.2 \times 10^{14}\,\mathrm{n_{eq}\,cm^{-2}}$. This corresponds approximately to the expected fluence after one year of HL-LHC operation. The measurements were done at the University of Glasgow.

The activation of DO-Q02 was determined with the help of a Geiger counter. On the surface, the measured activity was 200 Bq, which is 800 times the underground and thus equals approximately $100\,\mathrm{\mu Sv\,h^{-1}}$. This high value is probably a result of the scanning of the entire PCB, which is not done when irradiating FE-I4 single chip modules.

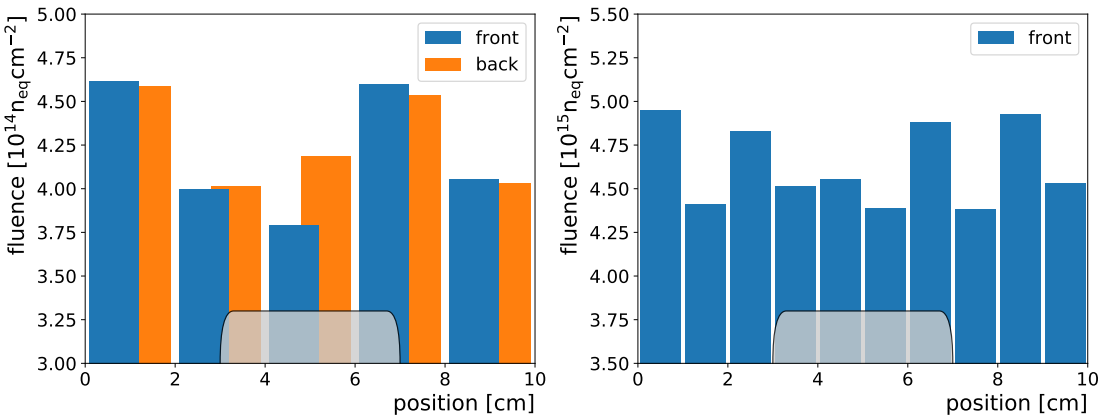

(a) Dosimetry result of the first irradiation step.

(b) Dosimetry result of the second irradiation step.

Figure 6.22: Dosimetry results of the irradiations. The shape at the bottom marks the position of the quad module.

Measurements were performed at different temperatures in a climate chamber. The resulting IV characteristics are shown in Figure 6.23a. No breakdown occurs up to 1000 V. The stated temperature corresponds to the set temperature of the climate chamber. A temperature offset of the sensor due to self-heating is expected, since there is no dedicated cooling of the module apart from air circulation. It can be observed in the increasing slope of the leakage current at bias voltages larger than 600 V, since both observables are directly related via Equation 2.5.

According to the ITk acceptance criteria [90], after an irradiation of $2 \times 10^{15}\,\mathrm{n_{eq}\,cm^{-2}}$ the leakage current should be less than $20\,\mu\mathrm{A\,cm^{-2}}$ at 400 V for a planar sensor of thickness 150 µm at −25 °C and after 10 days of room temperature annealing. The leakage current measured at 400 V equates to $10.4\,\mu\mathrm{A\,cm^{-2}}$. If fluence and thickness of the investigated module are scaled linearly to the values stated in the acceptance criteria, this corresponds to $26.1\,\mu\mathrm{A\,cm^{-2}}$ which exceeds the limit by 30 %. No annealing was considered in this estimation which could result in a reduction of up to 40 % [36].

Initial tests and tuning of all front-ends of DO-Q02 was successful, performed using a *USBpix* BIC setup and *STcontrol*. The sensor temperature was estimated via leakage current comparison to be −23 °C during operation due to the power dissipation of the four chips, when the climate chamber was set to −40 °C. The tuning procedure was performed at a bias voltage of 400 V. The resulting mean and standard deviation are (3190 ± 70) e for the threshold, (129 ± 22) e for the noise and (6.1 ± 0.3) ToT at a reference charge of 20 ke for the ToT. These values are comparable to the tuning values before irradiation.

Since no dedicated source setup was available, self-triggered source scans were performed during which the hits caused by the PCB's activity were measured. The energy spectrum is unknown, but a variety of β- and γ-decays can be assumed. Also α-decays

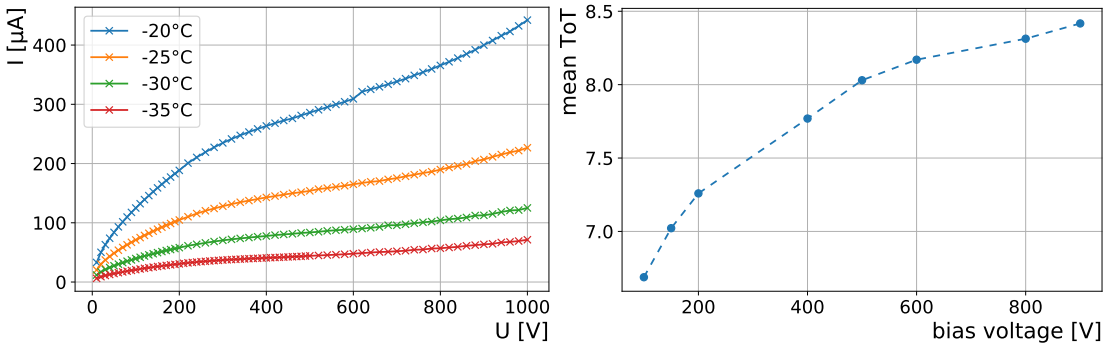

(a) IV characteristics at different temperatures.

(b) Mean ToT as a function of the applied bias voltage. The error bars resulting from the uncertainty of the fit are too small to be visible.

Figure 6.23: Result after the first irradiation.

cannot entirely be excluded. Source scans with 500 000 trigger each were recorded for different bias voltages between 100 V and 900 V.

Due to nature of interaction of photons with matter, γ-decays lead mainly to clusters of size 1, as shown in Table 6.7. To determine the energy loss of charged particles, only the ToT signal of size 2 clusters is considered. The resulting ToT distribution is still very broad, indicating that the detected particles do not behave like MIPs. Therefore a Gaussian function is used instead of a Landau function to describe the distribution. The resulting Gaussian mean is plotted against the applied bias voltage in Figure 6.23b. As expected, the mean value increases with increasing voltage, since on the one hand a higher voltage increases the width of the depletion zone and on the other hand the higher electric field increases the drift velocity of the charge carriers, which leads to reduced trapping and thus to an increased collected charge.

Before irradiation, a most probable energy loss of about 6 ToT was determined, but due to the differences in methodology, these values cannot be compared.

6.5.2 Testbeam measurements

After the second irradiation, testbeam investigations could be performed at a total fluence of $5 \times 10^{15}\,\mathrm{n_{eq}\,cm^{-2}}$. This value exceeds the predictions for the quad layers after ten years of operation under HL-LHC conditions by about 30 %. The activation of DO-Q02 was determined to approximately 1 mSv on the surface.

The measurements took place during a testbeam campaign at CERN in October 2017, using the setup as described in section 6.4. All DUTs were mounted in an insulated box which includes a heat exchanger connected to a regulated chiller. Since each of the up to 8 DUTs represents a heat source, the temperature of −44 °C, measured at the heat exchanger, is only a rough approximation of the temperature near the DUTs.

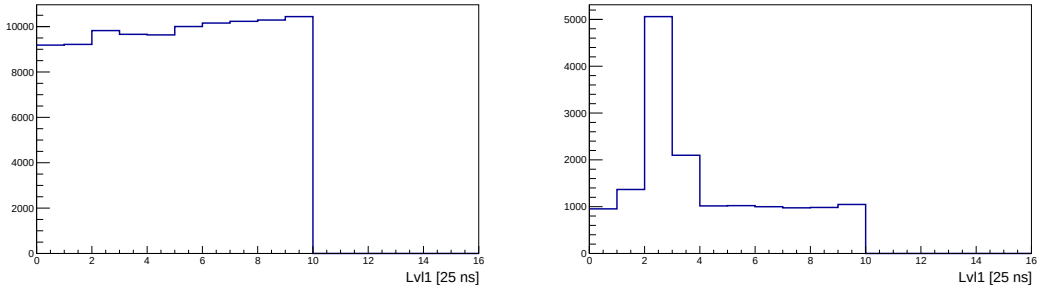

(a) LVL1 distribution for a run taken at a threshold of 3000 e.

(b) LVL1 distribution for a run taken at a threshold of 4000 e.

Figure 6.24: LVL1 distributions for measurements taken during the testbeam campaign in October 2017.

Initial test and tuning of all front-ends of DO-Q02 was successful, performed using an RCE setup. Different configurations were established with thresholds ranging from 2000 e to 3000 e, each with a ToT response of 8 at a reference charge of 16 ke. Although the tunings were good, it was not possible to obtain data until the threshold value was raised to 4000 e in a new tuning. The reason for this becomes clear when the LVL1 distributions are investigated, as they indicate the amount of noise in the data as described in section 5.4.4. The LVL1 distributions of runs taken at thresholds of 3000 e and 4000 e are shown in Figure 6.24. The reason for the high noise at the lower threshold is very likely the module's high intrinsic activity due to the irradiation of the PCB.

The IV characteristics were measured once during the operation of the FEs and once when they were not in operation as the LV was switched off. Even if the sensor temperature is not exactly known, a temperature rise of 19 K due to the power dissipation of the front ends can be determined by current scaling as described by Equation 2.6. The IV characteristics are shown in Figure 6.25a. According to the ITk acceptance criteria, after an irradiation of $5 \times 10^{15}\,\mathrm{n_{eq}\,cm^{-2}}$ the leakage current should be less than $36\,\mu\mathrm{A\,cm^{-2}}$ at 600 V for a planar sensor of thickness 150 µm at −25 °C and after 10 days of room temperature annealing. If the sensor temperature is assumed to be 25 °C, then the leakage current measured at 600 V equates to $77.2\,\mu\mathrm{A\,cm^{-2}}$. If the thickness is scaled linearly, this corresponds to $40.7\,\mu\mathrm{A\,cm^{-2}}$, which exceeds the limit by 13 %.

Tracks were recorded at different bias voltages between 400 V and 700 V using a configuration with a threshold of (3996 ± 75) e, a noise of (166 ± 21) e and a response of (8.2 ± 0.4) ToT at a reference charge of 16 ke. Due to upper limits for the leakage current, no higher voltages could be set. The analysis was performed with *EUTelescope* and *TBmon2* as described in section 6.4 for the unirradiated quad module. The efficiency map for the sensor at the highest bias voltage of 700 V is shown in Figure 6.25b. The mean efficiency is (33 ± 4) %. It was shown [92] that after an irradiation of $5 \times 10^{15}\,\mathrm{n_{eq}\,cm^{-2}}$, threshold values of 1600 e or lower and bias voltages of up to 1000 V are required to

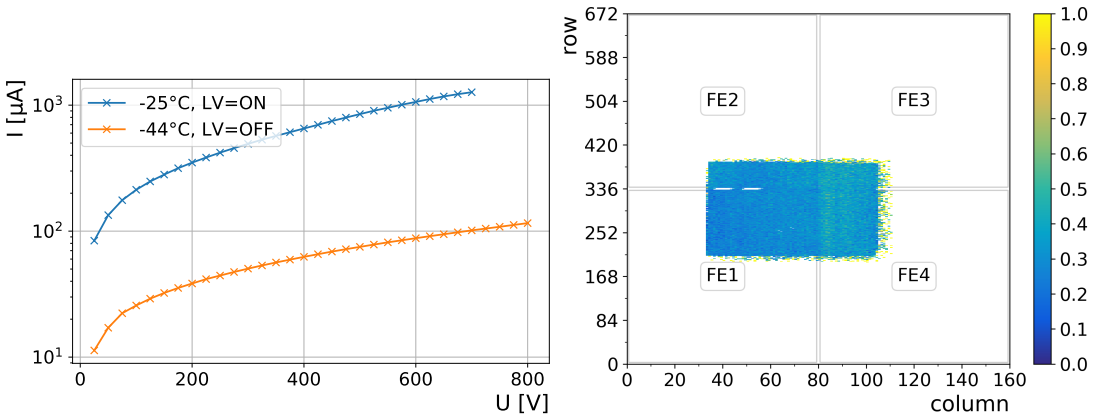

(a) IV characteristics taken with and without front-end operation.

(b) Efficiency map at a threshold of 4000 e and a bias voltage of 700 V.

Figure 6.25: Measurements of DO-Q02 after the second irradiation step, taken during the testbeam in October 2017.

achieve tracking efficiencies above 97 %, which is the requirement for ITk. This efficiency requirement is therefore missed due to the too high threshold and the too low bias voltage of the investigated quad module.

In the unirradiated state, the investigated quad modules are suitable candidates for the ITk. This is not confirmed by the investigations in the irradiated state, but there are still big differences to the quad sensors intended for use in the ITk. The leakage current requirements are not fulfilled because the investigated prototypes examined do not have the final thickness. For the final detector, the use of thinner sensors with thicknesses of 100 µm or 150 µm is foreseen. Activation of PCBs should be avoided, as it makes high thresholds necessary, which then prevent the achieving of high efficiencies. In the detector this is solved by using flexible printed circuits which have a significantly lower material budget. At the expense of stability, rigid PCBs can be replaced by such flex circuits also in laboratory and testbeam measurements. Finally, the cooling of quad modules within the testbeam setup must be largely improved so that higher voltages can be applied.

Chapter 7

Design improvement studies

The design of the ATLAS pixel sensors [41] has proven itself in detector operation. But as the demands on the sensors, such as higher granularity or irradiation doses, continue to increase, there are always efforts to improve the layout. For this purpose, changes to the sensor design are made and tested in new wafer productions.

It is necessary that even after irradiation a sufficient signal charge is induced and detected in the sensor and thus a high particle tracking efficiency is achieved. A lower power dissipation of the sensor is also an improvement, as the cooling capacity is always limited. Therefore, new designs compared to the standard design should achieve a high signal and a high tracking efficiency at low bias voltages to be considered as an improvement.

The results in section 7.1 were published in [94]: A. Gisen et al. *Investigation of modified ATLAS pixel implantations after irradiation with neutrons*, submitted to NIMA, 2018.

7.1 Studies with modified pixel implants

Previous investigations showed an increased signal charge after irradiation for thinner detectors [95] and at higher voltages [96], caused by reduced trapping and charge multiplication. These gain effects are probably similar to the one used in avalanche diodes, which lead to the development of **l**ow **g**ain **a**valanche **d**etectors (LGADs) [97].

Another approach is to modify the shape of the n^+ pixel implantations to force maxima in the electric field to increase the collected charge. Based on the IBL pixel design, six modified so-called REINER (**RE**designed, **IN**novative, **E**xciting and **R**ecognizable) pixel designs were developed in Dortmund [47].

Intensive studies on the leakage current of the individual designs before and after irradiation were performed on multiple sensors, revealing noticeable differences between the designs [98, 99]. In addition, a module irradiated with reactor neutrons of the Sandia ACRR to a fluence of $5 \times 10^{15}\,\mathrm{n_{eq}\,cm^{-2}}$ was investigated. Laboratory measurements with this module revealed in comparison to the IBL pixel design a similar or improved charge collection for the new pixel designs [100]. This is shown in Figure 7.1. Testbeam measurements revealed a similar or improved track reconstruction efficiency for the new pixel designs [101], as shown in Figure 7.2.

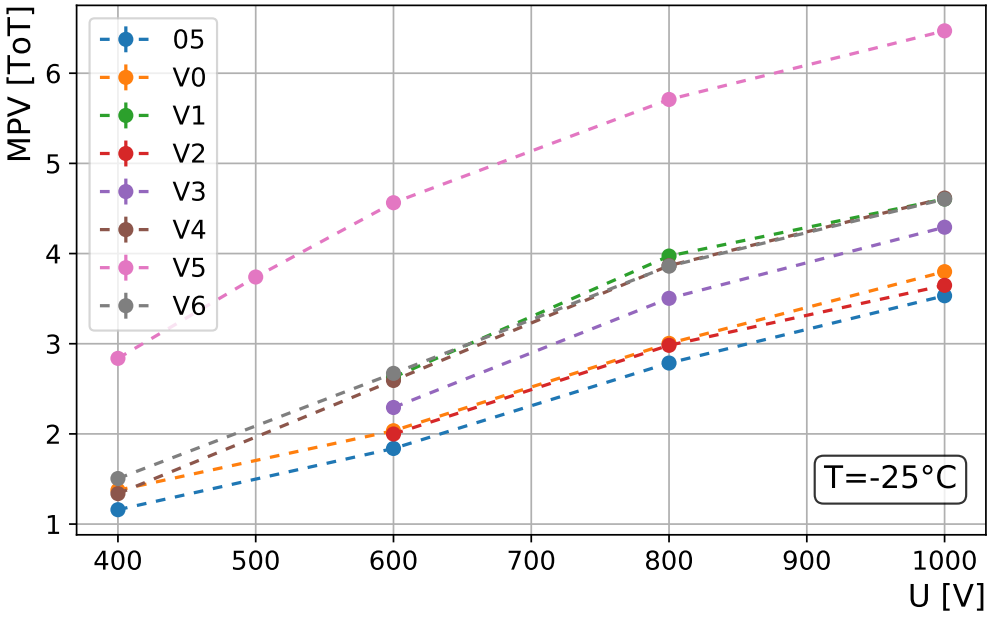

Figure 7.1: MPV as a function of the applied bias voltage for the irradiated REINER module. Data taken from [100].

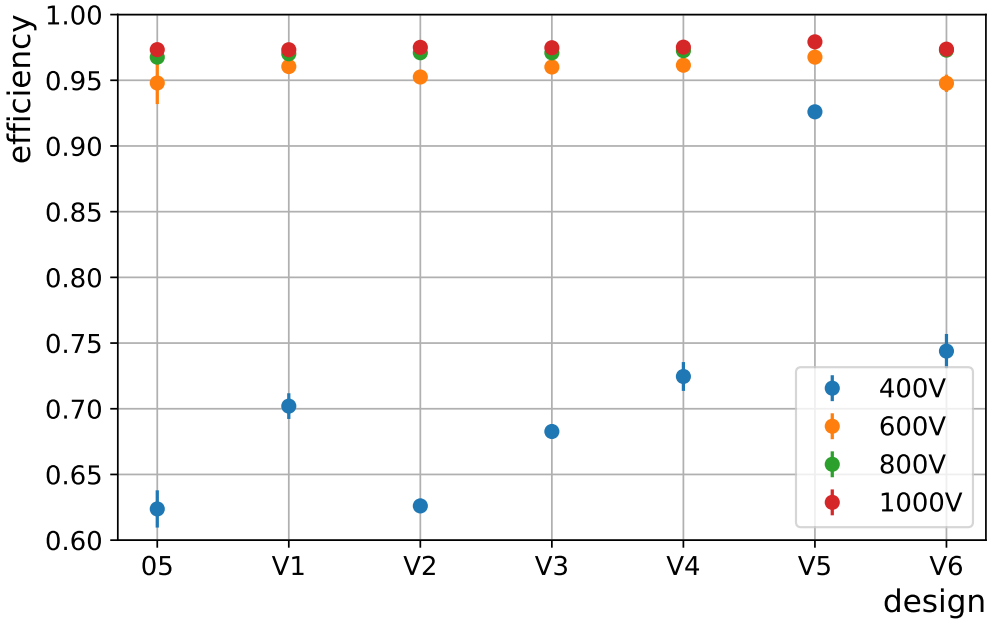

Figure 7.2: Tracking efficiencies for the individual designs as a function of the applied bias voltage for the irradiated REINER module. Data taken from [101].

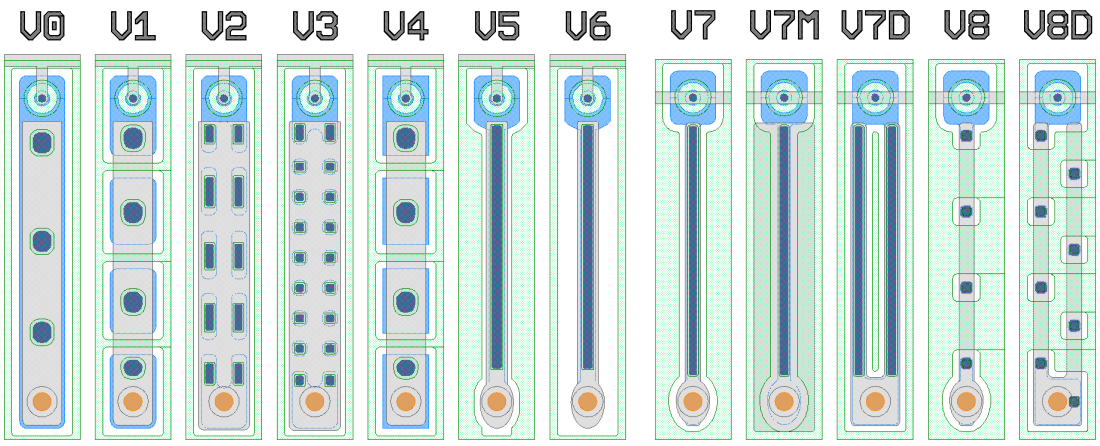

(a) Pixel layouts of REINER Mk I. **(b)** Pixel layouts of REINER Mk II.

Figure 7.3: All REINER pixel designs. Detailed descriptions of the Mk I designs can be found in [47, 94, 100, 101], whereas a detailed description of the Mk II designs can be found in Appendix C.

On the module irradiated with neutrons to $5 \times 10^{15}\,\mathrm{n_{eq}\,cm^{-2}}$, the REINER pixel designs perform similar or better than the IBL standard design in terms of charge collection and tracking efficiency. The best performing design is the pixel design *V5*. Its $\mathrm{n^+}$ implantation features a width of 10 µm, while at the same time the width of the high dose area of the moderated p-spray profile is largely increased. The width of the $\mathrm{n^+}$ implantation in the IBL design is 30 µm, which is three times as wide as in *V5*.

The layouts of *V0*, the IBL design, and *V5* are shown together with the layouts of the other pixel designs of the first version, REINER Mk I, in Figure 7.3a. The weiterdenkung of pixel design *V5* to explore the limits of this approach lead to the development of further modificated designs. These new modified designs form the second version, REINER Mk II. They are shown in Figure 7.3b and described in detail in Appendix C.

7.2 New wafer layouts

7.2.1 DOPIX2016

To prepare future investigations, a new wafer layout to be used on n-substrate was designed. For the development of the layouts of the individual sensors, the results from chapter 6 and section 7.1 were taken into account, but the wafer layout also contains sensors compatible with the forthcoming RD53A read-out chip.

An overview on the wafer layout is shown in Figure 7.4. A table giving some basic information about the sensors and a more detailed description of the individual sensor layouts can be found in Appendix C.

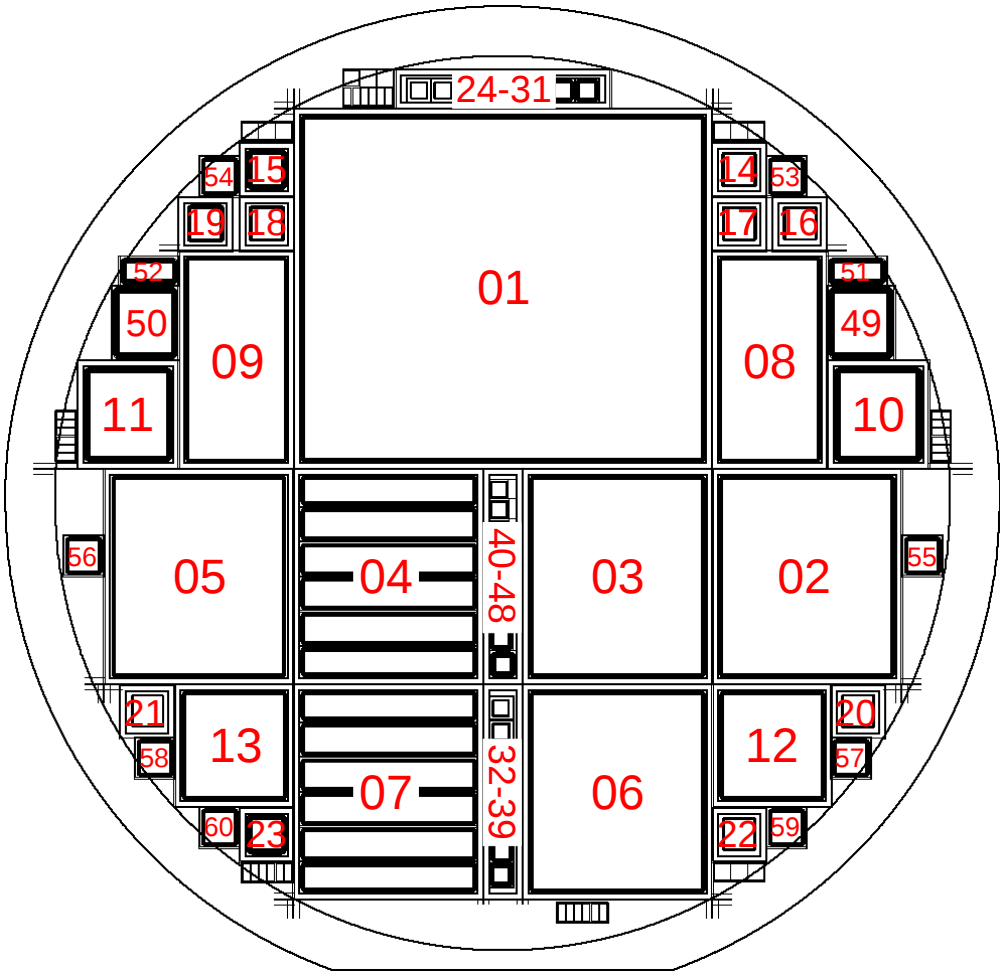

Figure 7.4: Overview on the DOPIX2016 wafer layout. View on p-side.

7.2.2 DOPIX2017

A further wafer layout was designed to be used on p-substrate, transferring the REINER pixel layout and many of the DOPIX2016 layouts from the n^+-in-n to the n-in-p technology. A detailed description of the sensor structures can be found in [102]. First wafers featuring this design are expected to be delivered in summer 2018.

7.3 IV characteristics of DOPIX2016 wafers

The DOPIX2016 design was submitted to CiS at the end of November 2016. The wafers of a first batch produced with this layout were delivered in spring 2018. According to the wafer vendor, the used n-type wafers have a thickness of 200 µm with a wafer resistivity of 2500 Ω cm to 5500 Ω cm. To get an overview of the quality of the sensors

of this production, IV characteristics were measured for several sensors of a few wafers before dicing. This overview did not yet include any REINER sensors, which will be investigated in detail in later studies.

Each investigated wafer was placed on a movable vacuum chuck in a probe station. The bias voltage was applied via a probe needle, ground was connected via the metal vacuum chuck. IV characteristics were measured in steps of 5 V up to a maximum voltage of 200 V. The breakdown voltage is defined as the voltage where the measured leakage current exceeds the limit of 5 µA. The ITk acceptance criteria states that the breakdown voltage should be larger than $V_{\text{depl}} + 70\,\text{V}$.

7.3.1 Breakdown voltage investigations

The IV characteristics of various sensors on the wafers *02* and *11* with DOPIX2016 layout are shown in Figure 7.5. The depletion voltages, determined by the manufacturer, are 60.4 V for wafer *02* and 40.6 V for wafer *11*, resulting in a resistivity of 2.23 kΩ cm and 3.32 kΩ cm, respectively.

The quad sensors with the layout *01*, which is compatible to four FE-I4 read-out chips, have a smooth curve and no breakdown is visible.

The sensors, which are compatible to single FE-I4 chips, show different behaviour. One sensor with the *02* layout, which features an IBL-compatible design, shows a strong rise in leakage current after a bias voltage of 50 V, but no breakdown occurs up to 200 V. The other sensor with the same layout has a smooth curve and no visible breakdown.

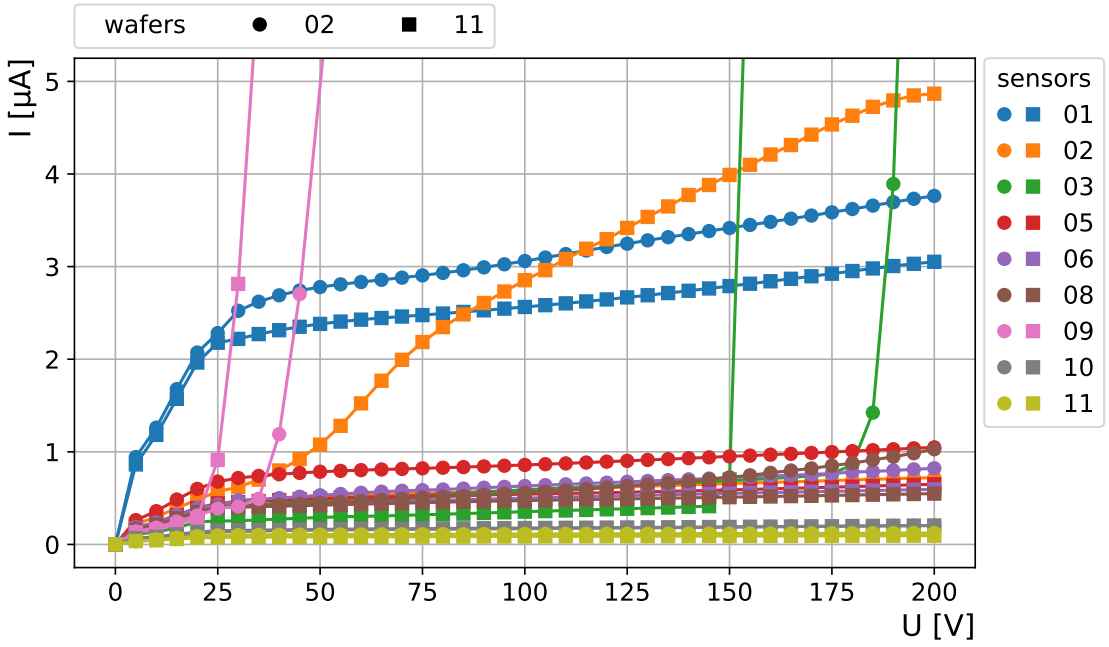

Figure 7.5: IV characteristics of various sensors on different DOPIX2016 wafers.

Since this behaviour occurs only with one sensor, which has the well examined IBL layout, this is a good example of the need for quality control, since a sensor occasionally does not meet the acceptance criteria. The sensor with the layout *05*, also with an IBL-compatible design but with a reduced bias ring width, have a smooth curve and no visible breakdown.

The sensor layouts *03* and *06* are comparable except for the width of the high dose area of the moderated p-spray profile. For the layout *03*, the width is increased to 10 µm instead of the usual 5 µm, leading also to an increased distance between the pixel implants of 20 µm instead of 15 µm and thus to a reduction of the pixel implant width by 5 µm, as the pixel pitch is unchanged. Both sensors feature common punch-through dots, each shared by four pixels. One sensor with the *03* layout has a breakdown at 150 V, the other has a breakdown at 190 V, which is still acceptable according to the ITk criteria but at lower voltage than most other investigated sensors. The sensors with the *06* layout have a smooth curve and no visible breakdown, which proves the functionality of the common punch-through dot concept for n^+-in-n sensors. The early breakdown of the sensors with the *03* layout is probably due to the increased distance between the n-implants in respect to the reduced n-implant width. A comparable effect was found in simulations of the breakdown voltage as a function of implant width of n-in-p sensors [50].

The sensors, which are compatible to RD53A read-out chips, show different behaviour. The sensors with the *08* layout, with a pixel pitch of $50 \times 50\,\mu m^2$, have a smooth curve. The sensors with the *09* layout, with a pixel pitch of $100 \times 25\,\mu m^2$, show an early breakdown below 50 V. A comparison of the layouts can be found in Figure C.3 in the appendix. While the distance between the n-implants in both sensor layouts is 15 µm, a significant difference is the square shape of the pixel implant of layout *08* compared to the long, narrow rectangular shape of layout *09*. Its unfavorable effects on the breakdown were already observed with the sensors with layout *06* and with the REINER designs *V5* and *V6*, but also the different bias dot pattern should be taken into account.

The sensor layouts *10* and *11*, which are compatible to FE-I3 chips, both have a smooth curve and no visible breakdown.

The investigations revealed good behavior in terms of breakdown voltage for most sensors. It is confirmed again that the IBL pixel design works very well in terms of a late breakdown. Modifications, like done on the sensors *03*, did not lead to any improvement in this respect. The reasons for the early breakdown of the sensors with a pixels of pitch $100 \times 25\,\mu m^2$ needs to be examined in more detail, because with such an early breakdown it makes sense not to use this layout on an n^+-in-n sensor.

7.3.2 Leakage current area density investigations

In [103], a reduction of the leakage current area density was found with increasing sensor area. This study comprised guard ring diodes and FE-I3 single, FE-I4 single, FE-I4 double and FE-I4 quad chip sensors. A reduction of 20 % for the leakage current area density from FE-I3 single chip sensors to FE-I4 quad chip sensors was observed.

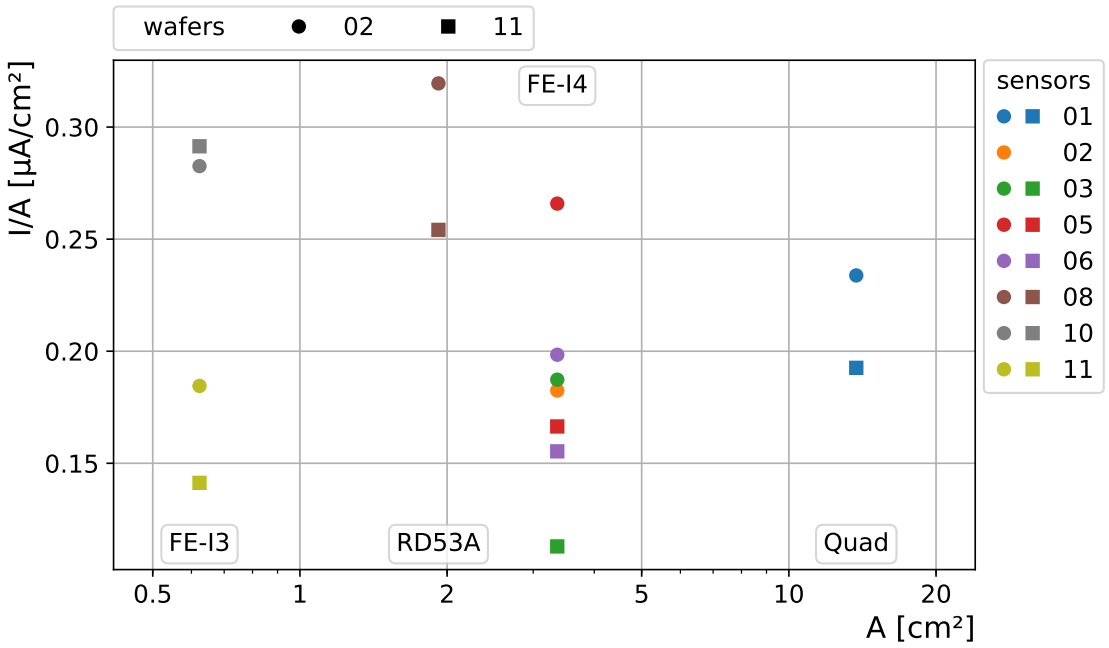

Figure 7.6: Leakage current area density at 120 V as a function of the sensor area of various sensors on different non-diced DOPIX2016 wafers.

The ITk acceptance criteria state that the leakage current should be less than $0.75\,\mu A\,cm^{-2}$ at $V_{depl} + 50\,V$. Therefore the leakage current is measured at a bias voltage of 120 V, which surpasses the voltage requirement. The leakage current area density at this voltage as a function of the sensor area is shown in Figure 7.6. All sensors clearly fulfil the leakage current requirement.

The difference between the leakage currents of the FE-I3 sized sensors indicates a strong dependence on the state of the surface. The sensor layout *10* features a pixel matrix, which means that it features a pixelated n-side, where the n^+-implants are interrupted by the p-spray passivation. The sensor layout *11* is diode-like, since its n-side, as for diodes, consists of a continuous n^+-implant which is not interrupted by the p-spray passivation. The diode-like layout avoids electric field strength maxima, which are a result of high gradients in the doping concentration, usually located at the pn-junction of the pixels and the p-spray passivation. For non-pixelated sensors, the avoiding of many pn-junctions leads to a more homogeneous electric field and thus to a reduced leakage current.

Taking this into account, the measurement data do not contradict the results of [103]. For a clearer statement, the statistics must be increased by measuring the sensors of further wafers.

Chapter 8

Conclusions

In order to meet the requirements of the HL-LHC, the current Inner Detector of the ATLAS experiment will be replaced by the new, all-silicon ITk. Quad chip modules are foreseen in its outer pixel barrel layers and in its pixel end-cap rings.

Two fully working n^+-in-n quad modules were assembled and investigated. Since the final ITk pixel read-out chip is not yet available, FE-I4 read-out chips were used. The examinations revealed very few defective pixels and thus a good bump bond quality, which is a challenge in the production of large-area modules, like quad modules are.

Promising results were obtained for the quad modules in laboratory and testbeam measurements. The tools used for the analysis such as *TBmon2* and *fei4analyzer* were adapted and enhanced to be suitable for quad modules. MIP-like particles deposit a charge signal corresponding to 20 ke at a threshold of 3200 e in the sensor. A tracking efficiency well above 99.9 % was measured for pixels with standard design which account for 95 % of all read-out channels. A successful analysis of the efficiency for pixels with 'ganged', 'inter-ganged' and 'long' designs was also demonstrated, revealing a tracking efficiency of more than 99.9 % for these special read-out channels.

While unirradiated, the investigated quad module prototypes would be suitable candidates for the ITk. This is not confirmed by the investigations after irradiation. The reasons for this lie in the nature of prototyping, like using rigid PCBs instead of flexible PCBs and their activation by an unfavourable irradiation treatment. The measurements should be repeated with pixel modules and under conditions that correspond to the ones of the final ITk.

Large scale prototyping and testing of various aspects of further quad modules already started within the ATLAS collaboration, as the pre-production of the final ITk pixel sensors will start next year. The experience gained in quad module handling simplifies future investigations and the findings of this work improve the testing methodology for quad modules.

In addition, studies to improve the design of the pixel cells were carried out. Superior charge collection and tracking efficiency were noted in some of the so-called REINER structures. A new wafer layout was developed to further study these designs. First wafers featuring the new layout were delivered this year, with promising results of initial measurements. The sensors will be used for module assembly, followed by the main investigation. The different sensors on the wafer also offer the possibility of further research on the fundamental properties of silicon.

References

[1] ATLAS Collaboration. Observation of a new particle in the search for the Standard Model Higgs boson with the ATLAS detector at the LHC. *Phys. Lett. B*, 716(1): 1–29, Sept. 2012.

[2] CMS Collaboration. Observation of a new boson at a mass of 125 GeV with the CMS experiment at the LHC. *Phys. Lett. B*, 716(1):30–61, Sept. 2012.

[3] G. Apollinari et al., editors. *High-Luminosity Large Hadron Collider (HL-LHC): Technical Design Report V. 0.1*, volume 4/2017 of *CERN Yellow Reports: Monographs*. CERN, 2017.

[4] The HL-LHC project website. URL `http://hilumilhc.web.cern.ch/about/hl-lhc-project`. [Online, accessed 23. 01. 2018].

[5] ATLAS Collaboration. Physics at a High-Luminosity LHC with ATLAS. Technical Report ATL-PHYS-PUB-2012-001, CERN, Aug. 2012.

[6] ATLAS Collaboration. Physics at a High-Luminosity LHC with ATLAS (Update). Technical Report ATL-PHYS-PUB-2012-004, CERN, Oct. 2012.

[7] ATLAS Collaboration. Technical Design Report for the ATLAS Inner Tracker Strip Detector. Technical Report CERN-LHCC-2017-005, CERN, Apr. 2017.

[8] ATLAS Collaboration. Technical Design Report for the ATLAS Inner Tracker Pixel Detector. Technical Report CERN-LHCC-2017-021, CERN, Sept. 2017.

[9] S. M. Sze and M.-K. Lee. *Semiconductor Devices: Physics and Technology*. John Wiley & Sons, New York, 3rd edition, 2012. ISBN 978-0470-53794-7.

[10] C. Leroy and P.-G. Rancoita. *Silicon Solid State Devices and Radiation Detection*. World Scientific, Singapore, 2012. ISBN 978-981-4390-04-0.

[11] C. Leroy and P.-G. Rancoita. *Principles of radiation interaction in matter and detection*. World Scientific, Singapore, 2nd edition, 2009. ISBN 978-981-4390-04-0.

[12] H. Kolanoski and N. Wermes. *Teilchendetektoren*. Springer-Verlag, Berlin Heidelberg, 2016. ISBN 978-3-662-45349-0.

[13] C. Patrignani et al. (Particle Data Group). Review of Particle Physics. *Chin. Phys. C*, 40(10):100001, Oct. 2016.

[14] H. Bichsel. Straggling in thin silicon detectors. *Rev. Mod. Phys.*, 60:663–699, July 1988.

[15] G. Lutz. *Semiconductor Radiation Detectors*. Springer-Verlag, Berlin Heidelberg, 2nd printing of the 1st edition, 2007. ISBN 978-3-540-71678-5.

[16] G. Lindström, M. Moll, and E. Fretwurst. Radiation hardness of silicon detectors – a challenge from high-energy physics. *Nucl. Instr. and Meth. in Phys. Res. A*, 426(1):1–15, Apr. 1999.

[17] G. Lindström. Radiation damage in silicon detectors. *Nucl. Instr. and Meth. in Phys. Res. A*, 512(1-2):30–43, Oct. 2003.

[18] E. A. Mobs. The CERN accelerator complex, 2016. URL `http://cds.cern.ch/record/2225847`. General Photo OPEN-PHO-ACCEL-2016-013.

[19] S. Gilardoni and D. Manglunki, editors. *Fifty years of the CERN Proton Synchrotron*. CERN Yellow Reports: Monographs. CERN, Geneva, June 2011.

[20] B. Adeva et al. DIRAC: A high resolution spectrometer for pionium detection. *Nucl. Instr. and Meth. in Phys. Res. A*, 515(3):467–496, Dec. 2003.

[21] M. Glaser et al. New irradiation zones at the CERN-PS. *Nucl. Instr. and Meth. in Phys. Res. A*, 426(1):72–77, Apr. 1999.

[22] F. Ravotti et al. A New High-Intensity Proton Irradiation Facility at the CERN PS East Area. *Proceedings of Science*, TIPP 2014:354, July 2015.

[23] F. Ravotti et al. Upgrade scenarios for irradiation lines: Upgrade of the Proton Irradiation Facility in the CERN PS EAST AREA. *AIDA Delivrable Report D8.4*, Sept. 2014.

[24] Information on the CERN PS-IRRAD website. URL `http://ps-irrad.web.cern.ch/documents/irrad_duration_2017.pdf`. [Online, accessed 26. 05. 2018].

[25] Super Proton Synchrotron marks its 25th birthday. *CERN Courier*, 41(6):24–26, July 2001.

[26] E. Gschwendtner. CNGS and North Area Operation. AB/OP Shutdown Lectures 2008, Mar. 2008. URL `http://jwenning.home.cern.ch/jwenning/documents/TrainingOP/ShutdownLectures_EG_Mar08.pdf`. [Online, accessed 25. 05. 2018].

[27] L. Evans and P. Bryant, editors. LHC Machine. *JINST*, 3(08):S08001, Aug. 2008.

[28] The twists and turns of a successful year for the LHC. *CERN Courier*, 57(10):10, Dec. 2017.

[29] ATLAS Collaboration. The ATLAS Experiment at the CERN Large Hadron Collider. *JINST*, 3(08):S08003, Aug. 2008.

[30] N. Readioff. The Large Hadron Collider, Feb. 2015. URL `https://ideas.lego.com/projects/94885`. [Online, accessed 11. 07. 2016].

[31] ATLAS Collaboration. Track Reconstruction Performance of the ATLAS Inner Detector at $\sqrt{s} = 13$ TeV. Technical Report ATL-PHYS-PUB-2015-018, CERN, July 2015.

[32] W. Buttinger. The ATLAS Level-1 Trigger System. *J. Phys.: Conf. Ser.*, 396(1): 012010, Dec. 2012.

[33] CMS Collaboration. The CMS experiment at the CERN LHC. *JINST*, 3(08): S08004, Aug. 2008.

[34] ALICE Collaboration. The ALICE experiment at the CERN LHC. *JINST*, 3(08): S08002, Aug. 2008.

[35] LHCb Collaboration. The LHCb Detector at the LHC. *JINST*, 3(08):S08005, Aug. 2008.

[36] ATLAS Collaboration. ATLAS Insertable B-Layer Technical Design Report. Technical Report CERN-LHCC-2010-013, CERN, Sept. 2010.

[37] ATLAS Collaboration. ATLAS Insertable B-Layer Technical Design Report Addendum. Technical Report CERN-LHCC-2012-009, addendum to CERN-LHCC-2010-013, CERN, May 2012.

[38] ATLAS IBL Collaboration. Production and Integration of the ATLAS Insertable B-Layer. *JINST*, 13(05):T05008, May 2018.

[39] M. Garcia-Sciveres et al. The FE-I4 pixel readout integrated circuit. *Nucl. Instr. and Meth. in Phys. Res. A*, 636(1):155–159, Apr. 2011.

[40] C. Gößling et al. Planar n^+-in-n silicon pixel sensors for the ATLAS IBL upgrade. *Nucl. Instr. and Meth. in Phys. Res. A*, 650(1):198–201, Sept. 2011.

[41] M.S. Alam et al. The ATLAS silicon pixel sensors. *Nucl. Instr. and Meth. in Phys. Res. A*, 456(3):217–232, Jan. 2001.

[42] S. Altenheiner et al. Planar slim-edge pixel sensors for the ATLAS upgrades. *JINST*, 7(02):C02051, Feb. 2012.

[43] C. Da Via et al. 3D silicon sensors: Design, large area production and quality assurance for the ATLAS IBL pixel detector upgrade. *Nucl. Instr. and Meth. in Phys. Res. A*, 694:321–330, Dec. 2012.

[44] ATLAS Collaboration. Letter of Intent for the Phase-II Upgrade of the ATLAS Experiment. Technical Report CERN-LHCC-2012-022, CERN, Dec. 2012.

[45] ATLAS Collaboration. ATLAS Phase-II Upgrade Scoping Document. Technical Report CERN-LHCC-2015-020, CERN, Sept. 2015.

[46] B. Ristic, on behalf of the ATLAS Collaboration. CMOS Pixel Development for the ATLAS Experiment at HL-LHC. *Springer Proceedings in Physics*, 213(2): 426–430, Aug. 2018.

[47] T. Wittig. Slim Edge Studies, Design and Quality Control of Planar ATLAS IBL Pixel Sensors. Dissertation, TU Dortmund, Apr. 2013.

[48] G. Aad et al. ATLAS pixel detector electronics and sensors. *JINST*, 3(07):P07007, July 2008.

[49] N. Savic et al. Investigation of thin n-in-p planar pixel modules for the ATLAS upgrade. *JINST*, 11(12):C12008, Dec. 2016.

[50] J.-C. Beyer et al. Characterisation of novel thin n-in-p planar pixel modules for the ATLAS Inner Tracker upgrade. *JINST*, 13(01):C01009, Jan. 2018.

[51] J. Lange et al. Radiation hardness of small-pitch 3D pixel sensors up to a fluence of $3 \times 10^{16}\,\mathrm{n_{eq}/cm^2}$. *JINST*, 13(09):P09009, Sept. 2018.

[52] FE-I4 Collaboration. The FE-I4B Integrated Circuit Guide, v2.3, Dec. 2012.

[53] RD53 Collaboration. The RD53A Integrated Circuit, v3.24. Technical Report CERN-RD53-PUB-17-001, May 2018.

[54] K. Dette. Commissioning of the ATLAS Insertable B-Layer and first operation experience. Dissertation, TU Dortmund, Feb. 2017.

[55] L. Gonella. Bump Bonding and Module Update in Germany. *Talk at the ATLAS Upgrade Week*, Apr. 2015.

[56] USBpix website. URL `http://icwiki.physik.uni-bonn.de/twiki/bin/view/Systems/UsbPix`. [Online, accessed 22. 07. 2017].

[57] STcontrol User Guide. URL `http://icwiki.physik.uni-bonn.de/twiki/bin/view/Systems/STcontrolUserGuide`. [Online, accessed 22. 07. 2017].

[58] RCE data acquisition framework development portal. URL `http://www.cern.ch/rceproject`. [Online, accessed 01. 08. 2017].

[59] RCE / HSIO distribution website. URL `http://www.slac.stanford.edu/exp/atlas/upgrade/RCE-distribution-2016May.html`. [Online, accessed 10. 03. 2018].

[60] E. Browne. Nuclear Data Sheets for A = 90. *Nuclear Data Sheets*, 82(3):379–546, Nov. 1997.

[61] M. Berger et al. ESTAR, PSTAR, and ASTAR: Computer Programs for Calculating Stopping-Power and Range Tables for Electrons, Protons, and Helium Ions (version 2.0.1). National Institute of Standards and Technology, Gaithersburg, MD, USA, 2017. URL `http://physics.nist.gov/Star`. [Online, accessed 08. 05. 2018].

[62] C. Nesaraja. Nuclear Data Sheets for A = 241. *Nuclear Data Sheets*, 130:183–252, Dec. 2015.

[63] fei4Analyzer website. URL `https://github.com/terzo/fei4Analyzer`. [Online, accessed 26. 05. 2018].

[64] CERN Program Library. URL `http://www.cern.ch/cernlib`. [Online, accessed 26. 05. 2018].

[65] K. Kölbig and B. Schorr. A program package for the Landau distribution. *Computer Physics Communications*, 31(1):97–111, Jan. 1984.

[66] Python Software Foundation. Python Language Reference, version 2.7. URL `https://pypi.org/project/pyLandau/`. Available at `http://www.python.org`. [Online, accessed 26. 05. 2018].

[67] pyLandau package website. URL `https://pypi.org/project/pyLandau/`. [Online, accessed 26. 05. 2018].

[68] Scipy optimize.curve_fit Reference Guide. URL `https://docs.scipy.org/doc/scipy/reference/generated/scipy.optimize.curve_fit.html`. [Online, accessed 26. 05. 2018].

[69] R. Brun and F. Rademakers. ROOT — An object oriented data analysis framework. *Nucl. Instr. and Meth. in Phys. Res. A*, 389(1-2):81–86, Apr. 1997. See also `http://root.cern.ch/`.

[70] F. James. MINUIT Function Minimization and Error Analysis: Reference Manual Version 94.1. *CERN Program Library*, entry D506, Mar. 1994.

[71] EUDET website. URL `https://www.eudet.org/`. [Online, accessed 26. 05. 2018].

[72] J. Baudot et al. First test results of MIMOSA-26, a fast CMOS sensor with integrated zero suppression and digitized output. *2009 IEEE Nucl. Sci. Symp. Conf. Rec. (NSS/MIC)*, pp. 1169–1173, Oct. 2009.

[73] EUDAQ website. URL `http://eudaq.github.io/`. [Online, accessed 26. 05. 2018].

[74] EUDET-type beam telescopes website. URL `https://telescopes.desy.de`. [Online, accessed 17. 03. 2018].

[75] H. Jansen et al. Performance of the EUDET-type beam telescopes. *EPJ Tech. Instrum.*, 3(1):7, Oct. 2016.

[76] EUTelescope website. URL `http://www.cern.ch/eutelescope`. [Online, accessed 26. 05. 2018].

[77] I. Rubinsky. EUTelescope. Offline track reconstruction and DUT analysis software. *EUDET-Memo-2010-12*, Dec. 2010.

[78] T. Bisanz. Test-beam activities and results for the ATLAS ITk pixel detector. *JINST*, 12(12):C12053, Dec. 2017.

[79] H. Gjersdal. Test beam track reconstruction and analysis of ATLAS 3D pixel detectors. Dissertation, Universitetet i Oslo, June 2014.

[80] Millepede-II website and manual. URL `http://www.desy.de/~kleinwrt/MP2/doc/html/index.html`. [Online, accessed 26. 05. 2018].

[81] TBmon2 website. URL `https://bitbucket.org/TBmon2/tbmon2`. [Online, accessed 26. 05. 2018].

[82] M. George. Testbeam Measurements with Pixel Sensors for the ATLAS Insertable b-Layer Project. Dissertation, Universität Göttingen, Apr. 2014.

[83] C. J. Clopper and E. S. Pearson. The Use of Confidence or Fiducial Limits Illustrated in the Case of the Binomial. *Biometrika*, 26(4):404–413, Dec. 1934.

[84] P. Dervan et al. The Birmingham Irradiation Facility. *Nucl. Instr. and Meth. in Phys. Res. A*, 730:101–104, Dec. 2013.

[85] P. Dervan et al. Upgrade to the Birmingham Irradiation Facility. *Nucl. Instr. and Meth. in Phys. Res. A*, 796:80–84, Oct. 2015.

[86] G. Lindström et al. Radiation hard silicon detectors – developments by the RD48 (ROSE) collaboration. *Nucl. Instr. and Meth. in Phys. Res. A*, 466(2):308–326, July 2001.

[87] I. Mateu. Experimental determination of the NIEL hardness factor for the new CERN proton irradiation facility. *Talk at the 28th RD50 Workshop*, June 2016.

[88] M. Moll et al. Leakage current of hadron irradiated silicon detectors – material dependence. *Nucl. Instr. and Meth. in Phys. Res. A*, 426(1):87–93, Apr. 1999.

[89] A. Gisen et al. Planar n-in-n quad module prototypes for the ATLAS ITk upgrade at HL-LHC. *JINST*, 12(12):C12032, Dec. 2017.

[90] A. Macchiolo. Technical Specification and Acceptance Criteria for the Planar Pixel Sensors for the ITK project. Technical Report ATL-COM-UPGRADE-2017-002, CERN, Feb. 2017.

[91] J. Weingarten et al. Planar pixel sensors for the ATLAS upgrade: beam tests results. *JINST*, 7(10):P10028, Oct. 2012.

[92] ATLAS IBL Collaboration. Prototype ATLAS IBL modules using the FE-I4A front-end readout chip. *JINST*, 7(11):P11010, Nov. 2012.

[93] Information on the CERN PS-IRRAD website. URL `http://ps-irrad.web.cern.ch/documents/run2017/Sets-2017.html`. [Online, accessed 30. 01. 2018].

[94] A. Gisen et al. Investigation of modified ATLAS pixel implantations after irradiation with neutrons. *To be published in Nucl. Instr. and Meth. in Phys. Res. A*, 2018.

[95] G. Casse et al. Enhanced efficiency of segmented silicon detectors of different thicknesses after proton irradiations up to $1 \times 10^{16} n_{\mathrm{eq}} \mathrm{cm}^{-2}$. *Nucl. Instr. and Meth. in Phys. Res. A*, 624(2):401–404, Dec. 2010.

[96] G. Kramberger et al. Investigation of Irradiated Silicon Detectors by Edge-TCT. *IEEE Transactions on Nuclear Science*, 57:2294–2302, Aug. 2010.

[97] G. Pellegrini et al. Technology developments and first measurements of Low Gain Avalanche Detectors (LGAD) for high energy physics applications. *Nucl. Instr. and Meth. in Phys. Res. A*, 765:12–16, Nov. 2014.

[98] J. Helmig. Investigation of Modified Pixel Implantations for Planar n^+-in-n Silicon Sensors. Masterarbeit, TU Dortmund, Sept. 2015.

[99] A.-K. Raytarowski. Comparison of Leakage Current Characteristics of the Pixel Designs of Irradiated and non-Irradiated REINER Pixel Sensors. Masterarbeit, TU Dortmund, May 2018.

[100] M. Grothe. Laboratory Studies of Planar n^+-in-n Silicon Pixel Sensors with Modified Pixel Implantations for the ATLAS Experiment. Masterarbeit, TU Dortmund, Mar. 2017.

[101] M. Weers. Test Beam Studies of Planar n^+-in-n Silicon Pixel Sensors with Modified Pixel Implantations for the ATLAS Experiment. Masterarbeit, TU Dortmund, Mar. 2017.

[102] S. Dungs. Design und Charakterisierung von planaren n^+-in-p Pixelsensoren für das ATLAS Experiment. Masterarbeit, TU Dortmund, Nov. 2017.

[103] R. Klingenberg, A. Gisen, et al. Power dissipation studies on planar n^+-in-n pixel sensors. *Nucl. Instr. and Meth. in Phys. Res. A*, 831:105–110, Sept. 2016.

Danksagung

Sehr viele Menschen haben mich bei der Erstellung dieser Arbeit in vielfältiger Art und Weise unterstützt, und dafür möchte ich mich bei ihnen bedanken.

Ich danke Prof. Dr. Kevin Kröninger für die Möglichkeit, meine Dissertation als Teil einer großen internationalen Kollaboration anzufertigen und dabei mit Kollegen aus verschiedensten Ländern zusammenzuarbeiten. Ebenso danke ich Prof. Dr. Thomas Weis für seine spontane Bereitschaft, das Zweitgutachten zu übernehmen und Dr. Bärbel Siegmann für ihre ebenfalls spontane Bereitschaft, als weiteres Mitglied der Prüfungskommission zu fungieren. Für seine zuvorkommende Bereitschaft, die Vertretung des Zweitgutachters zu übernehmen, bin ich Prof. Dr. Dr. Wolfgang Rhode sehr dankbar.

Der plötzliche Tod von PD Dr. Reiner Klingenberg hat eine große Lücke innerhalb unseres Lehrstuhls hinterlassen. Ich bin dankbar für unsere Zusammenarbeit und alles, was ich von dir über wissenschaftliches Arbeiten und das Bewältigen von Herausforderungen lernen durfte, Danke!

Prof. Dr. Claus Gößling hat mich schon früh in meiner Universitätskarriere für das ATLAS-Experiment begeistert. Ihm habe ich es zu verdanken, dass ich mich seit sechs Jahren mit dem Pixeldetektor beschäftigen darf.

Ich danke Silke für unser gemeinsames Nordseitenbüro und für die im Laufe der Jahre vielen Anmerkungen und Kommentare zu allen erdenklichen Lebenslagen, stets hilfreich, angebracht und überaus nützlich. Uns ist das kosmische Gleichgewicht zu verdanken!

Ich danke Jens, der sich die Mühe gemacht hat, die meisten Zeilen dieser Arbeit zu lesen und dabei hauptsächlich konstruktive Kritik zu hinterlassen.

Ich danke Jonas für seine vielen aufmunternden und antreibenden Worte, weltneue Entdeckungen, unerwartete Gewinnspiele, ausufernde Geschichten, Korrekturen in letzter Minute und Süßigkeiten.

Bei André und Mareike bedanke ich mich für euren Kampf mit der Testbeamreko, die mir den Einstieg in selbige deutlich erleichtert hat.

Bei Andrea, Markus und Mike bedanke ich mich für die vielen nützlichen Dinge die ihr vollbringt, die meistens unbemerkt im Hintergrund geschehen und beim Ausbleiben dramatisch auffallen.

Bei Tobias bedanke ich mich für die Einführung in *KLayout* und das Designen von Sensoren und dafür, dass du immer noch abhebst, obwohl du eine Dortmunder Nummer siehst.

Bei unseren wissenschaftlichen Werkstätten bedanke ich mich für die meist schnelle und immer zuverlässige Fertigung unserer Aufträge unter Berücksichtigung aller Sonderwünsche. Insbesondere danke ich Jens Sparfeld von der Elektronikwerkstatt für das Bestücken der Quad-PCB.

Noch mehr Dank kommt dem Rest des Lehrstuhls zu, insbesondere der Mensa-Runde, der Lasertag-Liste und e4 e.V., die durch Süßigkeiten, diverse Backwaren, Kaffeeklatsch, Ausflüge und anderweitige Aktivitäten für ein sehr angenehmes Arbeitsklima sorgten.

Schlussendlich möchte ich mich bei meinen Eltern, meinen Brüdern, meiner restlichen Familie und bei meinen Freunden für die vielfältige Unterstützung bedanken.

Ich danke erneut Silke und Jonas, für euren schlechten Einfluss auf meinen ansonsten tadellosen Lebenswandel.

Ich danke der Schwafelrunde, dabei zuallererst natürlich Stephan und Siggi, aber auch Arne, Felix, Nora, Philip, Sören und dem ganzen Rest, sowie dem Weihnachtsmarkt-Stammtisch, also Christian, Fabian, demselben Philip und dem anderen Philipp für unsere gemeinsame Zeit an der Uni und auch danach.

Ich danke dem inzwischen weltweit verstreuten Hungrigen Haufen für die Treffen am CERN und die anderweitigen Diskussionen, dabei besonders Karo für ihre Karte und Bane für die stets willkommene Aufnahme und die vielen, teils kurzfristig angekündigten, Übernachtungen.

Last but not least, I would like to thank all my colleagues from the ATLAS collaboration, whom I have always found to be very friendly and helpful. This includes in particular Fabian Hügging and Laura Gonella, for many tips and advices regarding FE-I4s; Wolfgang Dietsche, Lars Graber and Gerhard Brand, for wirebonding of my modules; Julia Rieger, for some very good advices regarding STcontrol; Tobias Bisanz, for his work on EUTelescope; Anna Macchiolo, for always sharing knowledge and devices and reference planes; Federico Ravotti and Giuseppe Pezzullo, for the irradiation at the CERN-PS and the help with the RP transportation; Sebastian Grinstein and Carles Puigdengoles, for providing the quad rigid PCB; Kenneth ‘Kenny’ Wraight, for the organization of the quad irradiation campaign and the support during the measurements in Glasgow; Dima Maneuski, for pointing out the right places in Glasgow; Jon Taylor, for our discussions about quads at testbeams; and Stefano Terzo, for the *fei4Analyzer*.

Special thanks go to all participants of the ATLAS ITk pixel testbeam campaigns, all the shifters, especially Mareike and the others from Dortmund, and, in no particular order, Julien Beyer, Natascha Savic, Marco Bomben, Audrey Ducourthial, Jörn Lange, David Vázquez Furelos, Koji Nakamura and André Rummler for making all the hours we spent there more comfortable and more fun.

Appendix A

Important FE-I4 configuration parameters

In the following, a short explanation about the most important configuration parameters for the operation of modules with FE-I4 read-out chips is given. More details and information about all configuration parameters can be found in [52].

Global parameters

GA (Global Adress) The configuration is sent to the FE with the corresponding GA.

The GA of an FE can be set on the PCB with jumpers via a binary pattern. This setting is necessary if more than one FE are connected like when operating quads. A GA value of 8 will send the configuration to all connected FEs.

HitDiscCnfg This enables the discrimination of *small hits* with a ToT signal of 1 or 2.

During detector operation, these hits are very likely delayed because of timewalk. Therefore they are suppressed to prevent allocation to the wrong **b**unch-**c**rossing **id**entifier (BCID) but not directly discarded. They are only taken into account if a *big hit*, a hit with a ToT signal larger than 2, is recorded in a neighbouring pixel.

Since this feature is not relevant for laboratory and testbeam measurements, this DAC should normally be set to 0, which disables this feature.

SmallHitErease This suppresses the readout of *small hits*, even in the case of a neighbouring *big hit*. To avoid unexpected behaviour, it should be enabled if HitDiscCnfg is disabled.

PrmpVbpf This DAC regulates the global feedback current for the first amplifier stage (Preamp). The fall time of this amplifier shapes the ToT signal, so this is a global setting for the ToT response.

The standard starting value is 20.

Amp2Vbpf This DAC regulates the feedback current for the second amplifier stage (Amp2). This stage is for gain only.

The standard starting value is 50. Since this DAC is very sensitive to radiation, it should be increased to 150 for irradiated modules.

VthinAlt_Coarse This is the coarse setting for the global threshold input voltage. This is a 8-bit DAC but only values of 0 to 2 are reasonable. In contrast to Vthin of the FE-I4A, this DAC is compensated for temperature dependence.

The standard starting value is 0.

VthinAlt_Fine This is the fine setting for the global threshold input voltage. This is a 8-bit DAC. In contrast to Vthin of the FE-I4A, this DAC is compensated for temperature dependence.

The standard starting value is 210.

TdacVbp This DAC sets the step size of the TDAC. In the case of broad TDAC distributions covering the full range of 0 to 31, this DAC should be increased. In the case of narrow TDAC distributions, this DAC should be decreased.

The standard starting value is 255.

FdacVbn Similar to TdacVbp, this DAC sets the step size of the FDAC. In the case of broad FDAC distributions covering the full range of 0 to 15, this DAC should be increased. In the case of narrow FDAC distributions, this DAC should be decreased.

The standard starting value is 30.

Pixel cell parameters

TDAC This is a 5-bit DAC for local pixel threshold tuning. It allows precise adjustment of the threshold.

The standard starting value is 15.

FDAC This is a 4-bit DAC for local pixel feedback current tuning. It allows precision adjustment of the ToT response.

The standard starting value is 7.

Enable (EN) Enables or disables a pixel. By default this map is only active in source scans and does not affect other scans.

Hitbus/HitOr Enables or disables the hitbus output of a pixel. Usually the inverted enable map. By default this map is only active in source scans and does not affect other scans.

Injection capacitance There are two capacitances for test charge injection, called $C_{\mathrm{inj1}}/C_{\mathrm{low}}$ and $C_{\mathrm{inj2}}/C_{\mathrm{med}}$. The nominal value for C_{low} is 1.95 fF, the nominal value for C_{med} is $2C_{\mathrm{low}}$ or 3.90 fF. Usual the sum of both capacitances, called C_{high}, is measured and used. The exact calibration values of either C_{low} and C_{med} or their sum have to be extracted during wafer probing.

Appendix B

General tuning procedure

In the following, a short explanation about the general tuning procedure of an FE-I4 module is given.

Important scans

- The *digital* checks the functionality of the digital pixel circuit
- The *analog test* checks the functionality of the analogue pixel circuit
- The *GDAC tune* adjusts both VthinAlt DACs
- The *If tune* adjusts the *PrmpVbpf* DAC
- The *TDAC tune* adjusts the *TDAC*
- The *FDAC tune* adjusts the *FDAC*

Tuning procedure

If the module is configured correctly, the LV currents should adapt. At first, a *digital* and an *analog* test should always be carried out, preferably with bias voltage applied. The general sequence of a *tuning* consists of an automatic GDAC and an *If* tune, followed by a *TDAC*, *FDAC* and a second *TDAC* tune.

1. *Digital* test
2. *Analog* test
3. *GDAC* fast tune
4. *IF* tune
5. *TDAC* fast tune
6. *FDAC* tune
7. *TDAC* fast tune

Starting from the standard values, thresholds of 2000 e can easily be reached. Such a stable tuning should be used for reaching lower thresholds. The automatic scans often fail when attempting, so the parameters have to be adjusted manually.

Appendix C

Description of the sensors of DOPIX2016

In the following, a short explanation about the sensors of the DOPIX2016 n^+-in-n wafer layout is given. This layout forms the basis for the masks required for the photolithographic wafer process. Most of the sensor layouts are suitable for thinning with KOH etching.

The detailed process steps are described in subsection 4.1.1. The layout colors corresponding to these steps are listed in Table C.1. An overview of the DOPIX2016 wafer layout is shown in Figure 7.4. An overview and some basic information about the individual sensors on the wafer can be found in Table C.2.

Table C.1: Colors used in the layouts.

	n-side	p-side
implant	blue	red
oxide passivation (opening)	brown	brown
inner nitride passivation (opening)	green	green
metal	grey	grey
outer nitride passivation (opening)	orange	orange

DOPIX2016 sensor layouts

01: Quad The design is adopted from the MNPix01 layout and corresponds to the one presented in section 4.4.1. The first and the last pixel column are located below the guard rings.

02, 05: FE-I4, IBL-like The design *02* is adopted from the MNPix01 layout and corresponds to the IBL layout. Again, the first and the last pixel column are located below the guard rings.

The design *05* is a slim version of design *02*. The width of the bias ring is reduced from 85 µm to 50 µm The height of the HV electrode is reduced by 50 µm at the top and bottom, and therefore it ends with the end of the pixelated area.

Table C.2: Overview on sensor structures on the DOPIX2016 wafer layout.

No.	sensor type	No. of GR	details
1	FE-I4 2x2 MCS	13	lateral edge pixels beneath **g**uard **r**ings (GR)
2	FE-I4 SCS	13	standard design, lateral edge pixels beneath GR
3	FE-I4 SCS	13	RD53 like pixels (pixel sizes $250 \times 50\,\mu m^2$ and $5 \cdot 50 \times 50\,\mu m^2$), common bias dot, p-spray width 10 µm
4	FE-I4 SCS	13	REINER Mk II, pixel variants, segmented p-side
5	FE-I4 SCS	13	slim design: bias ring 50 µm, slim p-side, lateral edge pixels beneath GR
6	FE-I4 SCS	13	RD53 like pixels (pixel sizes $250 \times 50\,\mu m^2$ and $5 \cdot 50 \times 50\,\mu m^2$), common bias dot, p-spray width 5 µm
7	FE-I4 SCS	13	biasing concepts: common bias dot or poly-Si, segmented p-side
8	RD53A SCS	11	pixel size $50 \times 50\,\mu m^2$, common bias dot
9	RD53A SCS	11	pixel size $100 \times 25\,\mu m^2$, common bias dot
10	FE-I3 SCS	16	conventional design
11	FE-I3 diode	16	without pixel implants
12, 13	micro-strip	13	128 strips, 75 µm pitch
14–22	GR diodes	16 to 5	active area $9\,mm^2$
15	GR diode	16	active area $9\,mm^2$, no etching mask
23	GR diode	16	active area $9\,mm^2$, passivation openings on GR, no etching mask
24–31	GR diodes	13 to 5	active area $2.25\,mm^2$, increasing distance to edge, no etching mask
32–39	GR diodes	13 to 5	active area $2.25\,mm^2$, increasing distance to edge
40–48	GR diodes	13 to 5	active area $2.25\,mm^2$, 50 µm distance to edge
49	test structure	16	punch through and bias dot variations, no etching mask
50	test structure	16	punch through and bias dot variations, low p-spray dose, no etching mask
51, 52	MOSFET	16	ATLAS production design, no etching mask
53–60	GR diodes	13	active area $9\,mm^2$, no etching mask

03, 06: FE-I4, RD53 like pixels These designs are suitable to an FE-I4 chip, but are intended to be RD53A chip-like. Therefore, in the first half of pixel columns, the pixel implant is an adaption of a $50 \times 50\,\mu m^2$ pixel. One side of the $50 \times 50\,\mu m^2$ pixel cell

was stretched to 250 µm. In the second half of the pixel columns, each $250 \times 50\,\mu m^2$ pixel cell features 5 implants of size $50 \times 50\,\mu m^2$, connected via a metal trace. Parts of the pixel matrices are shown in Figure C.1a. Both halves of the pixel columns feature common bias dots. They are located close to the bump bond pad to mimic RD53A sensors in this region.

The difference between layouts *03* and *06* is the width of the high dose area of the moderated p-spray profile. For layout *03*, the width is 10 µm, as in the standard IBL layout *02*. For layout *06*, the width is 5 µm, as in the RD53A layout *08*.

The first and last pixel column have the standard IBL pixel layout and bias dot.

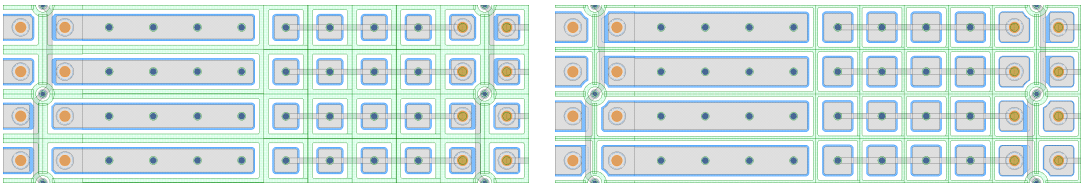

(a) Part of the pixel matrix of sensor *03*. **(b)** Part of the pixel matrix of sensor *06*.

Figure C.1: Different pixel layouts used in the sensors compatible to RD53A chips.

04: REINER Mk II Starting with Mk I [47], further modified pixel designs have been developed. These new REINER pixels are the weiterdenkung of *V5*. The sensor *04* has its p-side segmented by guard rings into 6 parts, each featuring one of the pixel designs. The designs of the individual pixels are shown in Figure C.2, along with the segmented p-side.

V0 is the standard IBL pixel for on-sensor comparison.

V7 is similar to *V5* of Mk I, but with a further reduced width of n-implant to the lowest value of 8 µm, which can reasonably be manufactured.

V7M is similar to *V7*, but the metal layer is broadend to investigate a possible influence.

V7D is similar to *V7*, but it features two narrow n-implants with a width of 8 µm.

V8 features small n-implants with an implant size of $8 \times 8\,\mu m^2$ with a pitch of 50 µm, a possible solution for RD53A-chips.

V8D is similar to *V8*, but features two rows of the small n-implants.

07: Biasing concepts This sensor features different biasing concepts. Again, its p-side is segmented into 6 parts by guard rings. One part corresponds to the IBL standard design. Two parts feature common bias dots. Three parts feature different poly-Si biasing concepts.

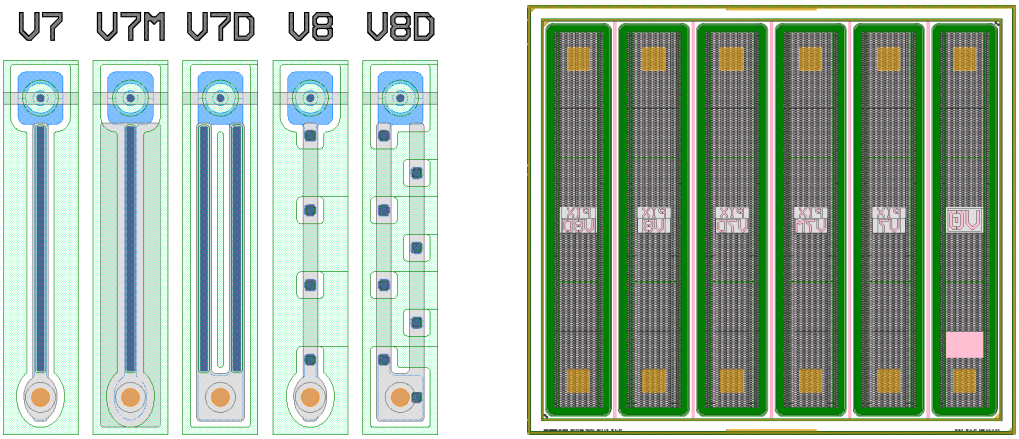

(a) Design of the different pixels. **(b)** Segmented p-side.

Figure C.2: Design of the different pixels and the segmented p-side of the REINER Mk II sensor.

08, 09: RD53A single chips sensors The design *08* features pixel cells with a pitch of $50 \times 50\,\mu m^2$ and a common punch through dot between every second pixel column and every second row. The design *09* features pixel cells with a pitch of $100 \times 25\,\mu m^2$ and a common punch through dot between every forth pixel column and every row. An excerpt of the pixel matrix for both different layouts is shown in Figure C.3. Other than the FE-I4 sensors, both RD53A sensor layouts feature only 11 GRs.

10, 11: FE-I3 The sensor layout *10* is a conventional FE-I3 layout. The sensor layout *11* has the size of an FE-I3 sensor, but features no pixel matrix. Thus it is diode-like.

12, 13: Micro-strip sensors Both micro-strip sensors features the same layout. It has 128 strips with a pitch of 75 µm. The biasing of the strips is done via a poly-Si resistor, which is connected to the bias ring.

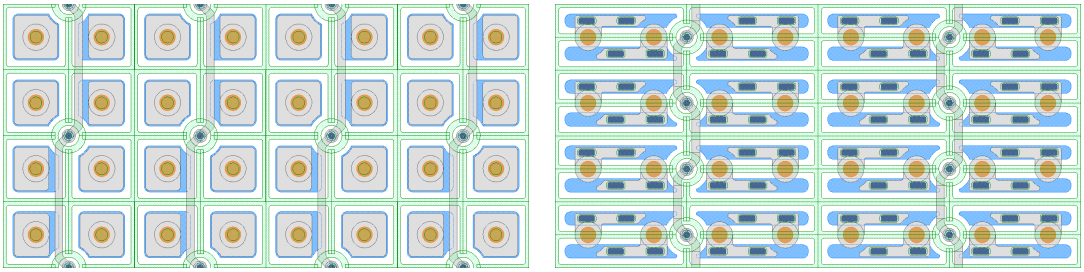

(a) Part of the pixel matrix of sensor *08*. **(b)** Part of the pixel matrix of sensor *09*.

Figure C.3: Different pixel layouts used in the sensors compatible to RD53A chips.

Appendix D

Conference contributions, publications and talks

A. Gisen: *Investigation of highly irradiated ATLAS n^+-in-n planar pixel sensors.* Talk at the "25th RD50 Workshop", November 2014, CERN, Geneva, Switzerland.

A. Gisen: *Annealing bestrahlter planarer n^+-in-n ATLAS Pixel Siliziumsensoren.* Talk at the "Frühjahrstagung der DPG", March 2015, Wuppertal, Germany.

A. Gisen: *Sensorentwicklung für das ITk-Upgrade des ATLAS-Pixeldetektors.* Talk at the "47. Herbstschule für Hochenergiephysik", September 2015, Maria Laach, Germany.

A. Gisen, on behalf of the PPS community: *Recent results of the ATLAS Upgrade Planar Pixel Sensors R&D Project.* Talk at the "ATLAS Upgrade Week", November 2015, CERN, Geneva, Switzerland.

A. Gisen: *Power Dissipation Studies on n^+-in-n Pixel Sensors.* Talk at the "27th RD50 Workshop", December 2015, CERN, Geneva, Switzerland.

A. Gisen: *Planare n^+-in-n Quadmodule für das ITk-Upgrade des ATLAS-Experiments.* Talk at the "Frühjahrstagung der DPG", March 2016, Hamburg, Germany.

R. Klingenberg, S. Altenheiner, D. Bryan, S. Dungs, A. Gisen, C. Gößling, B. Hillringhaus, K. Kröninger, C. Ratering, T. Wittig: *Power dissipation studies on planar n^+-in-n pixel sensors.* Nucl. Instr. Meth. Phys. Res. A **831**, September 2016, pp. 105–110.

A. Gisen: *Planare n^+-in-n Quadmodule für das ITk-Upgrade des ATLAS-Experiments.* Talk at the "Frühjahrstagung der DPG", March 2017, Münster, Germany.

A. Gisen: *Investigation of modified ATLAS pixel implantations.* Talk at the "30th RD50 Workshop", June 2017, Kraków, Poland.

A. Gisen: *Prototypes of planar n-in-n quad modules for the ATLAS ITk upgrade at HL-LHC.* Poster at the "11th International Conference on Position Sensitive Detectors (PSD11)", September 2017, Milton Keynes, UK.

A. Gisen: *Investigation of modified ATLAS pixel implantations after irradiation with neutrons and protons.* Talk at the "31st RD50 Workshop", November 2017, CERN, Geneva, Switzerland.

A. Gisen: *Investigation of modified ATLAS pixel implantations after irradiation with*

neutrons. Poster at the "11th International 'Hiroshima' Symposium on the Development and Application of Semiconductor Tracking Detectors (HSTD11)", December 2017, OIST, Okinawa, Japan.

A. Gisen, S. Altenheiner, I. Burmeister, C. Gößling, R. Klingenberg, K. Kröninger, J. Lönker, M. Weers, F. Wizemann: *Planar n-in-n quad module prototypes for the ATLAS ITk upgrade at HL-LHC*. JINST **12**, December 2017, C12032.

A. Gisen: *Planare n^+-in-n Quadmodule für das ITk-Upgrade des ATLAS-Experiments*. Talk at the "Frühjahrstagung der DPG", March 2018, Würzburg, Germany.

A. Gisen, S. Altenheiner, C. Gößling, M.Grothe, R. Klingenberg, K. Kröninger, J. Lönker, M. Weers, T. Wittig, F. Wizemann: *Investigation of modified ATLAS pixel implantations after irradiation with neutrons*. Accepted in Nucl. Instr. Meth. Phys. Res. A in August 2018.

In addition, four status updates on the activities in Dortmund at one AUW, two pixel sensor meetings and one ITk week.

Appendix E

Supervised and co-supervised theses

Jonas Lönker: *Einfluss der Temperatur auf den Betrieb von FE-I3-Single-Chip-Assemblies.* Bachelorarbeit, TU Dortmund, Dezember 2014.

Sascha Dungs: *Aufbau und Charakterisierung eines Messplatzes für temperaturabhängige Messungen von ATLAS Pixelsensoren.* Bachelorarbeit, TU Dortmund, Juli 2015.

Mattias Gianfelice: *Charakterisierung von FE-I4 Singlechip-Assemblys des Atlas Pixeldetektors.* Bachelorarbeit, TU Dortmund, Juli 2015.

Daniel Bryan: *Investigation of the voltage-current-relationship of silicon detectors.* Vacation Laboratory Studentship Report, TU Dortmund, August 2015.

Carolin Ratering: *Verlustleistung in bestrahlten planaren n^+-in-n Siliziumstrukturen.* Bachelorarbeit, TU Dortmund, August 2015.

Jara Helmig: *Investigation of Modified Pixel Implantations for Planar n^+-in-n Silicon Sensors.* Masterarbeit, TU Dortmund, September 2015.

Felix Wizemann: *Building and Testing of a Setup for Capacitance Measurements of ATLAS-Pixel-Sensors Under the Influence of High-Voltage.* Masterarbeit, TU Dortmund, September 2015.

Nora Held: *Entwicklung einer Versuchsanleitung zur Vermessung von Silizium-Streifensensoren mit dem Educational Alibava System.* Masterarbeit, TU Dortmund, Februar 2016.

Felix Janning: *Untersuchung von gealterten bestrahlten ATLAS FE-I4A Single Chip Assemblies.* Bachelorarbeit, TU Dortmund, Juli 2016.

Michael Podlech: *Raumtemperaturannealing von bestrahlten ATLAS FE-I3 Single Chip Assemblies.* Bachelorarbeit, TU Dortmund, Juli 2016.

Marius Grothe: *Laboratory Studies of Planar n^+-in-n Silicon Pixel Sensors with Modified Pixel Implantations for the ATLAS Experiment.* Masterarbeit, TU Dortmund, März 2017.

Mareike Weers: *Test Beam Studies of Planar n^+-in-n Silicon Pixel Sensors with Modified Pixel Implantations for the ATLAS Experiment.* Masterarbeit, TU Dortmund, März 2017.

Alexander Kroner: *Entwicklung des "DUT Config Checkers" zur Verbesserung der Geometrieimplementierung von ATLAS-Sensoren in TBMon2.* Bachelorarbeit, TU Dortmund, Juli 2017.

Sascha Dungs: *Design und Charakterisierung von planaren n^+-in-p Pixelsensoren für das ATLAS Experiment.* Masterarbeit, TU Dortmund, November 2017.

Anna-Katharina Raytarowski: *Comparison of Leakage Current Characteristics of the Pixel Designs of Irradiated and non-Irradiated REINER Pixel Sensors.* Masterarbeit, TU Dortmund, Mai 2018.